SOME FRACTIONAL ORDER DIFFUSION MODELS FOR SINGLE IMAGE FOG REMOVAL AND DENOISING

Ph. D. THESIS

by

SAVITA

DEPARTMENT OF MATHEMATICS
INDIAN INSTITUTE OF TECHNOLOGY ROORKEE
ROORKEE - 247 667 (INDIA)
February, 2020

SOME FRACTIONAL ORDER DIFFUSION MODELS FOR SINGLE IMAGE FOG REMOVAL AND DENOISING

A THESIS

Submitted in partial fulfilment of the requirements for the award of the degree

of

DOCTOR OF PHILOSOPHY

in

MATHEMATICS

by

SAVITA

DEPARTMENT OF MATHEMATICS
INDIAN INSTITUTE OF TECHNOLOGY ROORKEE
ROORKEE - 247 667 (INDIA)
February, 2020

INDIAN INSTITUTE OF TECHNOLOGY ROORKEE

STUDENT'S DECLARATION

I hereby certify that the work presented in the thesis entitled **"SOME FRACTIONAL ORDER DIFFUSION MODELS FOR SINGLE IMAGE FOG REMOVAL AND DENOISING"** is my own work carried out during a period from July, 2014 to February, 2020 under the supervision of Dr. Sanjeev Kumar, Associate Professor, Department of Mathematics, Indian Institute of Technology Roorkee, Roorkee.

The matter presented in the thesis has not been submitted for the award of any other degree of this or any other Institute.

Dated: February 12, 2020 **(SAVITA)**

SUPERVISOR'S DECLARATION

This is to certify that the above mentioned work is carried out under my supervision.

Dated: February 12, 2020 **(Dr. Sanjeev Kumar)**

Supervisor

Dedicated to my parents

Mr. Karambir Nandal and Mrs. Rajwanti,

my loving husband

Mr. Chaturbhuj Kuntal

and my siblings who supported me all the way since the beginning of my studies.

Abstract

This thesis presents new algorithms that endow with improved elucidation to the problem of image restoration. In particular, five different algorithms are presented to deal with the two subproblems of image restoration namely 'defogging' and 'denoising'. All these five algorithms utilize a fractional-order generalization of integer order derivatives in the image space during an implementation of diffusion filtering. Several experimental results are presented in the form of qualitative and quantitative evaluations to support the algorithms proposed in the thesis. A detailed comparison study of some existing approaches has been carried out to highlight the applicability and the virtue of the proposed algorithms. The proposed algorithms have many applications in different areas such as video surveillance, traffic monitoring, healthcare imaging, remote sensing, etc.

The thesis starts with a general introduction of the image defogging and image denoising problems. The motivation of the proposed work is also expressed. A brief inspection of the existing techniques related to image denoising and defogging is summed up in first chapter. Then two different algorithms are presented to deal with the problem of image defogging/dehazing. Each of these algorithms uses a fractional-order anisotropic diffusion model to have a refined airlight map for restoring fog affected degraded images. First algorithm diffuses each channel of the airlight map separately and finally these channels are fused to get a refined airlight map. In the second algorithm, a cross-channel term is added to balance the inter-channel diffusion for

avoiding the diffused/blended bands. This helps restore images having more than one channel in a better and improved way. Apart from the inter-channel regularization term, the intensity and direction of the anisotropic diffusion are controlled by a factor p, which gives better results.

To extend the study of the thesis to image denoising problem, two different algorithms are proposed for removing additive noise from the degraded images. The third algorithm makes use of fractional quaternion wavelet transform (FrQWT). For filtering the noisy components in FrQWT domain, hard and semi-soft thresholdings are used. Finally, a phase regularization step is implemented before applying the inverse FrQWT. It is worth to mention here that the proposed wavelet image denoising in the FrQWT domain gives impressive results in case of additive white Gaussian noise. The fourth algorithm uses anisotropic diffusion and wavelet transform-based subspace decomposition. This method is directionally sensitive for better edge preservation. Moreover, fractional derivatives based convolution filters are implemented in different wavelet subbands of the noisy image which makes algorithm suitable for parallel computing.

Finally, a new diffusion coefficient known as 'tansig' function of fractional order gradients is proposed to improve the accuracy and convergence of the earlier algorithms. This method is applicable for image defogging as well as image denoising problems. The thesis is concluded based on the work presented in the earlier chapters. Likewise, a brief description of the scope for further study is given.

List of Publications

1. Nandal, S. and Kumar, S., 2019. Single image fog removal algorithm in spatial domain using fractional order anisotropic diffusion. Multimedia Tools and Applications, 78(8), pp.10717–10732.

2. Nandal, S. and Kumar, S., 2020. Fractional-Order Anisotropic Diffusion for Defogging of RGB Images. International Journal of Image and Graphics, 20(01), p.2050001.

3. Nandal, S. and Kumar, S. (2018) Image Denoising Using Fractional Quaternion Wavelet Transform. In: Proceedings of 2nd International Conference on Computer Vision & Image Processing. Advances in Intelligent Systems and Computing, 704. Springer, Singapore DOI:10.1007/978-981-10-7898-925

4. Nandal, S. and Kumar, S., Generalized order anisotropic diffusion model for image denoising using wavelet based subspace decomposition, Multimedia Tools and Applications 2019. (Current Status: Under review)

5. Nandal, S. and Kumar, S., Image denoising and defogging using New Adaptive Diffusion Functions, IET Image Processing 2019 (Submitted in May 2019)

Acknowledgements

At this moment of accomplishment, I feel immense pleasure to express my gratitude to Almighty God for giving me strength and wisdom, and all those who contributed in many ways in my journey of doctoral research and made it an unforgettable experience of my life. First of all, I would like to express my sincere thanks to my supervisor Dr. Sanjeev Kumar, Associate Professor, Department of Mathematics for his guidance, patience, valuable suggestions, motivation and continuous support throughout my research. I am fortunate to do my research under his guidance as I have learned to overcome many difficulties from his expertise. I am also grateful to him for providing an excellent atmosphere for doing research and freedom to explore new things. His guidance helped me a lot during my research in various ways. I could not have imagined having a better advisor and mentor for my Ph.D study.

I am also indebted to Prof. N. Sukavanam, Head, Department of Mathematics, IIT Roorkee and DRC chairperson, Prof. Kusum Deep, Department of Mathematics, IIT Roorkee, for providing valuable advice and infrastructural facilities during my research. I owe my gratitude to all the faculty members, especially to my SRC members Prof. Kusum Deep, Prof. Roshan Lal and Assistant Professor Dr. Vinod Pankajakshan, for their valuable time, remarks, suggestions and guidance, which helped me in improving my skills and quality of research work.

I would like to acknowledge the financial support of the Ministry of Human Resource and Development (MHRD), New Delhi, India to carry out this research work.

I express my profound gratitude to Sunil Dua Sir for his constant efforts, support and motivation.

He is the main reason for what I am today. Also, I am deeply thankful to Dr. Amit Sehgal for playing instrumental role in shaping my career.

Special thanks are due to my senior and friend Dr. Snehlata Shakya for her propelling support and for offering positive influence in my research work and giving me the mental support at the time when I needed it the most.

I would like to thank all my lab members, Dr. Pushpendra, Dr. Anu Bala, Farhan, Mahima, Ashishi, Neeraj, Deepak and Deepa. I am thankful to my friends, Tripti, Tarul, Arti, Prasanta, Abhishek, Vivek, Jagannath and Scindhiya. Due to their affection, care and support it has been unforgettable memories and pleasant stay at IIT Roorkee.

I dedicate this thesis to my parents, for showing faith in me and giving me liberty to choose what I desired. I am honored for the selfless love, care, pain and sacrifice you did to shape my life. You were willing to support every decision I made. I would never be able to pay back the love and affection showered upon by my parents. I am extremely thankful to my sister Sarita. We did all our education together. She has been my constant support throughout my career. I share heartfelt gratitude towards my younger sister Monika and brother Ajay for their love, affection, blessings, continuous support which kept me going without which nothing was possible.

I also dedicate this thesis to my loving husband Mr. Chaturbhuj Singh. I feel a deep sense of gratitude for him for inspiring me and showing faith in me. Your love, hope, moral support, and guidance have given me the strength to overcome many difficulties and gave confidence to perform my best. No words are enough to express my appreciation for him, without whose support I would not have achieve this goal.

Finally, I am thankful to all those whose name I could not mention but they have contributed in many ways in my research journey to complete this thesis.

Roorkee (Savita)
November , 2019

Table of Contents

List of Figures

List of Tables

Chapter 1

Introduction

This chapter contains a brief description about the introduction and motivation leading to the work presented in this thesis. The introduction about the image defogging and denoising problems is given in Section 1.1. The motivation of this work is expressed in Section 1.2. Section 1.3 gives a brief literature review about the existing techniques for restoring digital images degraded with fog and additive noise. Section 1.4 contains the definitions of some of the metrics used in the subsequent chapters for having quantitative evaluation of the restored images. Finally, Section 1.5 describes the details about subsequent chapters in brief.

1.1 General introduction

Image restoration is a well-studied problem in vision research. The goal of image restoration is to remove or reduce unwanted details like noise, fog/haze, blurring artifacts, etc. from the degraded images. Though in the past few decades, many methods are developed to restore the foggy/noisy images in different conditions, however, restoration of a single foggy/noisy image is still a challenging and amusing task. It attracts not only engineering communities, but also mathematician due to its ill-posed nature and rich theory in terms of various mathematical tools. In general, we require a clean image for many image processing applications such as object detection [63, 80, 115], image/video

retrieval [76, 79, 139], image encryption [16, 77, 143] and remote sensing applications [31, 55, 132]. Image enhancement techniques [4, 49, 90, 114, 124, 138] can be used for increasing the visual quality of an image, however there is a clear distinction between image enhancement and image restoration. Image restoration is an attempt to restore an image to its ideal fidelity, such by removing scratches, blur, haze or noise. On the other hand, image enhancement is an attempt to improve an image beyond what the camera took, by adding color, contrast or detail that was not really there. Therefore, restoration is a kind of inverse problem in which we need to restore images to its original form by removing the effect of degradation operator. In this thesis, we are dealing with anisotropic diffusion-based partial differential equations (PDEs) for restoring the images degraded with fog/haze and presence of additive noise.

In foggy conditions, the images of an outdoor scene are generally of bad quality due to the existence of the water droplets and dust particles resulting in reduced visibility and contrast of the scene. This is an annoying problem, as it has a negative effect on image grabbing results, in the degradation of the captured image. The foggy images have poor visibility, color artifacts and low contrast due to the absorption and scattering of the atmospheric particles. The particles/water droplets in the atmosphere are one of the main reasons for indigent clarity. These droplets reflect light which results in the degradation of an image of the scene. This scattered light enhances whiteness in the scene which is known as airlight. The light which is reflected from the object gets absorbed by the atmospheric particles which further gets attenuated and decreases the visual quality of the scene. This process is known as attenuation. It becomes important to remove the fog for the better visual quality of the images. Here, a couple of approaches are proposed in this thesis to deal with the problem of removing fog/haze from the digital images.

The another image restoration subproblem, we are dealing in this thesis is related to reduce/remove additive noise from digital images. The images of real-world objects gets noisy during the time when the images are captured or transmitted. Some camera sensors corrupts the image by introducing random variations in the image intensity and color information. This noise may also be inherited due

to the reasons like atmospheric turbulence, imperfections in the equipment or the medium used for transmission process. The noise can be more intensive during the acquisition phase, if the appliances used are having low-resolution sensors. The main objective of an image denoising process is to discard the noise, while retaining the sharp features of the image (edges, corners, texture details, etc). Noise is a high-frequency component, so it seems like details of the image, therefore, noise remains preserved in the filtering process or edges become blur. Also, random and uncorrelated noises can not be compressed easily. The removal of noise from the image is a challenging problem as there is a range of images from smooth textures to images with innumerable edges. In the spatial domain, the problem of image restoration is an ill-posed problem. Mathematically, it implies that the matrix which models the noise and blur in the imaging system has eigenvalues close to zero which makes the inversion process unstable. From the applications point of view, the removal of noise is a necessary step in many image processing applications like pattern recognition [113], object segmentation [61, 80], image interpolation [7, 89], image segmentation [160] and in real imaging systems [88, 105, 106, 108] which needs a clean image for processing.

In this thesis, we have used anisotropic diffusion PDEs for restoring the images while preserving the edges and sharp details of the images. Generally, the perception of a diffusion process is to equilibrate concentration while generating or destructing mass [150]. It can be explicitly configured in a mathematical form using the *Fick's* law as follows:

$$j = -D \cdot \nabla I \tag{1.1}$$

The relation between flux j and concentration gradient ∇I is characterized by a diffusion tensor D. If j and gradient ∇I are parallel, then the diffusion is said to be isotropic one. In the case of isotropic diffusion, the diffusion coefficient is a constant function. If the diffusion tensor D is a function of gradients, it will be called as nonlinear isotropic diffusion. In the case of nonlinear diffusion, diffusion takes place like linear diffusion except the region where diffusion is constrained to preserve sharp details. In the case of anisotropic diffusion, flux j and gradient ∇I are usually not parallel. The anisotropic diffusion-based models take into account not only the image gradients but the edge directions also.

The diffusion tensor constructs two eigenvectors in such a way that one eigenvector is parallel to the image gradients and another one is perpendicular to the image gradients. Mathematically, the behavior of diffusion which only transfers mass without creation and destruction of mass is represented by the continuity equation.

$$\partial_t I = div(D \cdot \nabla I) \tag{1.2}$$

In the case of image processing, the intensity values at some particular pixel is the concentration in the above diffusion PDE.

1.2 Motivation for the study

Although over the past few decades, many techniques have been developed for the restoration of digital images degraded by additive/multiplicative noise or by the atmospheric artifacts such as fog/haze. However, several challenges still persist which remains an interesting problem for several researchers. The study proposed in this thesis is motivated by some of these challenges.

It is still a debatable issue that out of the first-order gradient and Laplacian based filters, which one gives more accurate and sharp details of an image. Therefore, generalization of these integer-order derivatives may have the advantages of both of them. Hence, the work of this thesis harness the theory of the fractional-order derivative, where the order of differentiation is considered in the interval $[1, 2)$. Apart from it, the design of the diffusion coefficient in the anisotropic diffusion is still a challenging issue. To address this issue, we have designed a couple of new coefficients that are not only adaptive but also play a significant role in the convergence of iterative schemes for solving the fractional order diffusion PDEs.

In a nutshell, we propose five different algorithms that provide better solutions to a couple of image restoration problems. Comprehensive experimental results are presented in the form of qualitative and quantitative evaluations to support the efficiency and applicability of the algorithms proposed in the thesis. Apart from that, a detailed analysis has been carried out along with the comparisons with

some of the existing approaches to highlight the applicability and merits of the proposed algorithms.

1.3 Literature review

Image restoration is an active research area having applications in many vision frameworks such as object detection [63, 80, 115], image/video retrieval [47, 67–69, 76, 79, 109, 110, 116, 139], image inpainting [42] and remote sensing [31, 55, 132], etc. The work presented in this thesis for image restoration has two different subproblems: (i) to remove the fog/haze from synthetic as well as natural foggy/hazy images, and (ii) to remove the additive white Gaussian noise from 2D digital images. In this section, we will present a concise survey of each of these subproblems. Here, we first follow up on the different methods in the literature which describe the different techniques to restore foggy/hazy and noisy images from the degraded ones.

1.3.1 Classification of image defogging/dehazing techniques

The poor vigilance and low contrast of the scene in the foggy images is caused by absorption and scattering by the atmospheric particles. The main reason for the less visibility in the foggy images is the particles/water droplets in the atmosphere. The water droplets absorb the transmitted light from the scene and get attenuated. This is known as attenuation. Also, the particles scatter the light absorbed from the scene in the atmosphere which causes additional whiteness in the scene. This process is known as airlight map. The attenuation and airlight map depends on the depth of the scene from the camera. The main goal of image defogging/dehazing is to restore the fog/haze from the degraded images. In literature, many methods have been proposed to restore the foggy images. The defogging/dehazing methods require either an airlight map or a depth map. Image defogging techniques can be divided into the following categories.

- Histogram based methods [51, 66, 81]
- Polarization filter based methods [112, 126]

- Markov Random field(MRF) based methods [45, 137]
- Dark channel prior(DCP) based methods [50, 57, 58, 144, 158]
- Anisotropic diffusion based methods [17, 48, 117, 123, 135, 150, 152]
- Deep learning based methods [6, 10, 86, 131, 147, 157, 169, 173]

1.3.1.1 Histogram based image defogging techniques

In literature, the traditional image restoration techniques were based on contrast enhancement. The contrast enhancement approaches can be divided into three types (i) the histogram equalization, (ii) the histogram modification, and (iii) the non-overlapped block adaptive histogram modification [51, 66, 81]. Histogram equalization technique was used to attain the homogeneous histogram for image restoration. The main drawback of this global histogram equalization scheme was the destruction of occasionally distributed pixel intensities. In the histogram modification approach, an output image is enhanced by adjusting the vigorous range of pixel values so that the output image is visually better. The non-overlapped block adaptive approach was based on the intensities of pixels in a particular neighborhood. This approach has high computational complexity, thus, it was hard to implement this technique in real-time due to storage reasons. Also, the non-overlapped block adaptive histogram modification technique leaves blocking artifacts. To overcome these issues, Kim et al. [81] introduced a block-overlapped histogram equalization algorithm for spatially adaptive contrast enhancement. They also introduced a filtering technique for abolishing over amplified noise.

1.3.1.2 Polarization filter based methods

In 2000, Narasimhan and Nayar [112] developed a geometric framework for analyzing the chromatic effects of atmospheric scattering. In the night, there can be no illumination of daylight so there will be no airlight, so in this condition attenuation dominates. Although in dense fog/haze conditions, the transmitted light from the scene gets attenuated which causes dominance of airlight map. However,

in most of the situations, airlight map as well as attenuation both coexist. In [112], the chromatic effects of scattering in the atmosphere were discussed when both airlight map and attenuation are present together. Firstly, a simple color model for atmospheric scattering was studied which is known as the dichromatic atmospheric scattering model. It was described that the color of a scene in bad weather conditions is a linear combination of the direction of transmitted light and the direction of airlight map. Then, based on the physics of scattering, several geometric constraints were derived on scene color changes, caused by varying atmospheric conditions. Finally, using these constraints, an algorithm was developed for computing fog or haze color, depth segmentation, extracting three-dimensional structure, and recovering true scene colors, from two or more images taken under different but unknown weather conditions.

In 2003, Schechner et al. [126] presented a method which was based on evidence that the light scattered by the atmosphere particles is partially polarized. The optical filtering method was efficient in removing fog/haze in restricted positions only. However, the method described by Schechner et al. works well for a broad range of atmospheric conditions including low polarization. They stated that the light ray from the source to a scatterer and the line of sight from the camera to the scatterer define a plane of incidence. At least two images that were captured at two distinct degrees of polarization were required for implementing the method. Their method was completely based on the polarization of the airlight map. The airlight map was divided into two polarization parts which are parallel and perpendicular to the plane of incidence. The parallel component was associated with minimum observed scene radiance and the perpendicular component was associated with maximum observed scene radiance. However, their method is less effective, when the sky illumination is dull or weather is overcast. Moreover, stability of their method decreases when the degree of polarization of airlight map decreases. This method may fail in case of heavy polarizations.

1.3.1.3 Markov random field(MRF) based methods

The polarization-based methods exploited two or more images of the same scene with different degrees of polarization. The different degrees of polarization might be obtained just by rotating the polarization filter attached with the camera [125]. However, these methods may not be applicable when there is a variation in the scene where the changes are faster than the rotation of filter for finding the minimum and maximum degrees of polarization. The idea of these techniques was to accomplish the differences in distinct images obtained using the polarization filter, which have diverse properties of the engaging medium. The visibility enhancement induced by these methods was significant but the drawback was that it can not handle the scene variations.

In 2008, Tan [137] introduced a method that needed only single images as input. It does not require the multiple images or the geometrical model of the scene. This method was based on a couple of specific perceptions. First, the images with more visibility have high contrast than the foggy images, and second, the airlight map tends to be smooth. A cost function was defined based on the past previous observations in the structure of Markov-random-fields (MRFs). This function can be optimized efficiently using various techniques and the method is applicable to gray as well as color images. Firstly, they obtained atmospheric light from input image. The light chromaticity is calculated using the airlight map. The light color of the input image is removed using the light chromaticity. Afterwards, the data cost and smoothness cost are determined for every pixel of the image. The data cost is estimated from the contrast of a small patch of the image and the smoothness cost is figured out from the distance between labels of two neighboring pixels where the labels are equivalent to the airlight map values. The complete MRFs are developed using these data costs and smoothness costs which are further optimized. These optimized values of the airlight map are used to determine direct attenuation. Finally, this procedure produces an image of the scene with more intensified visibility.

In 2008, Fattal [45] also introduced a method to calculate the optical transmission for a single input image. For this, the image is interpreted through a model that accounts for surface shading in addition to the scene transmission. Based on this refined image formation model, the image is

broken into regions of a constant albedo and the airlight-albedo ambiguity is resolved by deriving an additional constraint that requires the surface shading and medium transmission functions to be locally statistically uncorrelated. This requires the shading component to vary significantly as compared to the noise present in the image. A graphical model was used to propagate the solution to pixels in which the signal-to-noise ratio falls below an admissible level. The airlight color is also estimated using this un-correlation principle. This method was passive and does not require constraints like multiple images of the scene, any light-blocking-based polarization, any form of scene depth information, or any specialized sensors or hardware. Fattal's method has the minimal requirement of a single image acquired by an ordinary consumer camera. Also, Fattal's method does not assume the haze layer to be smooth in space, i.e., discontinuities in the scene depth or medium thickness are permitted.

1.3.1.4 Dark channel prior(DCP) based methods

The progress made by single image haze removal methods was significant but the disadvantage of these methods is that they rely on steady prior assumptions. Tan[137] assumed that the contrast of the haze-free image must be higher in comparison to the initial hazy image. Consequently, the haze was removed by maximizing the local contrast of the restored haze-free image. Also, Fattal [45] computed the albedo of the scene and the medium transmission with the assumption that the transmission and the surface shading are locally uncorrelated. However, this method fails when the assumptions are not satisfied and when there is a considerable amount of haze in the images. Therefore in 2011, He et al. [57] introduced a novel approach called a dark channel prior (DCP). This approach was based on the local stats of an outdoor haze-free image. They discovered that in most parts of an image, there are pixels whose intensity is very low throughout in at least one channel of an RGB image. These pixels were termed as dark pixels. The airlight map is the main reason for the intensity of the dark pixels in a channel of a hazy image. These dark pixels directly provide an accurate estimation of the haze transmission. They combined a haze imaging model and a soft matting interpolation method and the image recovered using this method was of high quality and generated a good depth map.

This approach was physically valid and handled distant objects in heavy haze images as well. The only limitation of this method was when the scene radiance became equivalent to the airlight map. However, this method applies to most of the outdoor hazy images. In 2013, He et al. [58] introduced an efficient method called as guided image filtering. It is an edge-preserving smoothing operator similar to the bilateral filtering method [144]. The guided image filtering method preserved edges better than bilateral filtering. Also, this method was fast and its computational complexity is independent of the filtering kernel size. Several models were proposed by making use of DCP-based restoration of the airlight map which includes [50, 158], etc.

1.3.1.5 Deep learning based methods

In recent times, the deep learning-based techniques are very popular in image processing and computer vision community. Deep learning has gained much popularity in terms of accuracy when using a very large amount of data. Deep learning techniques are a subset of machine learning techniques that works incrementally by identifying low-level classes first and then move towards higher-level categories. Its main application lies in image restoration, image classification, natural language processing, and speech recognition. Deep learning-based methods overcome the shortcomings of traditional methods by automatically learning and getting more suitable image features rather than manually setting the parameters [86]. Big data and GPU are a must for improving the learning capacity of deep learning methods [62]. In image processing, convolutional neural networks are the most successful and classic network for deep learning [91]. However, in successive years, deeper neural networks are getting more popularity and attaining intense performance for image processing problems. Karen Simonyan et al. [29] increased the depth of neural networks to 16-19 weighted layers and the convolution filter of size 3×3 for each layer in image recognition [131]. Following that Christian Szegedy et al. implemented a mechanism by using a sparsely connected layer [6] instead of fully connected layers to increase the width and depth of the neural networks [136]. Although, deep networks have attained successful applications in image processing problems [128] it can cause exploding gradients with increased network depth [14].

This can cause networks to block the convergence. This problem can be avoided by using normalized initialization [157]. Although, when deeper neural networks tend to converge, networks are saturated and degrade quickly with increasing depth of networks. The appearance of the residual network effectively dealt with the aforementioned problems of image recognition [59]. ResNeXt method is a tried and tested method for image classification [159]. The spatial-temporal Attention (SPA) method is very competitive for visual tracking [174]. Residual Dense Network (RDN) is also an effective tool for image super-resolution [173]. Furthermore, DiracNets [169], IndRNN [95] and variational U-Net [43] also provide us with many competitive technologies for image processing. These deep networks are also widely applied in image de-noising, which is the branch of image processing technologies. For example, the combination of kernel-prediction net and CNN is used to obtain a denoised image [10]. BMCNN utilizes NSS and CNN to deal with image denoising [2]. GAN is used to remove noise from noisy image [147].

1.3.2 Classification of image denoising techniques

Image denoising is a fundamental problem in image processing. In most of the cases, noise in digital images is found to be additive in nature with uniform power in the whole bandwidth and with Gaussian probability distribution. Such type of noise is called additive white Gaussian noise (AWGN). It is a vigorous task to just suppress AWGN since it corrupts a significant number of pixels in an image. The noisy image produces undesirable visual quality, it also lowers the visibility of low contrast objects. To remove noise without excessive smoothing of important details, a denoising technique needs to be spatially adaptive. In this thesis, techniques based on wavelet filtering and anisotropic diffusion are considered. A brief survey of these two type of denoising techniques are given in this section.

- Wavelet transform based methods

- Anisotropic diffusion-based methods

1.3.2.1 Wavelet transform-based methods

In recent times, wavelet transforms in frequency domain has acquired generous attention of many researchers to deal with image analysis. Wavelet analysis is coming out as one of the biggest important tools in signal analysis, pattern recognition, image processing, and other fields [1, 78, 108]. Wavelet analysis provides a multi-scale signal decomposition and multi-resolution analysis which gives the entire idea of details occurring at different locations [108]. In image/signal analysis, Gabor functions were used extensively as filters. Gabor filters are bounded and well described using a general window function. This important aspect paved a way for the introduction of windowed Fourier transform [52]. It opened the scope for the development of the wavelet analysis [35, 53]. Simultaneous analysis of time-frequency details and certain desirable properties of multiresolution analysis have proved wavelet transform as a breakthrough tool in image analysis [21, 104]. The basic idea of wavelet transforms is to decompose an image into different frequency subspaces. Wavelets are better than other transforms in time-frequency localization and denoising at multi-resolutions. Taking into account all the legacy, the generalization to the complex discrete wavelet transform(CDWT) from the real-valued wavelet transform came quite naturally [83, 97]. The real discrete wavelet transform and complex wavelet transforms have drawbacks like a small shift in the real discrete wavelet transform signal can generate considerable changes in the magnitude of wavelet coefficient distribution. Progressively, the dual-tree complex wavelet transform or in short CDWT was proposed by Kingsbury [82, 84]. It was basically a computational structure of the complex wavelet transform (CDWT) which has been used frequently in the various image processing applications [12]. This variant conquers a couple of limitations over the classical DWT. Firstly, the magnitudes of the transform coefficients were found to be shift-invariant as real and imaginary parts of CDWT make an Hilbert-pair. Secondly, the advantage of having the phase information which was not found in DWT with real mother wavelet functions. The CDWT utilizes the property of analytic filter banks and therefore, having a representation in terms of magnitude as well as phase information. However, the CDWT model is not found to be an ideal generalization of analytic wavelets in the case of 2-D signals. The CDWT has very low directional selectivity and its only phase

can cause uncertainty when converting into two directions. After that, the real and complex wavelet transforms are extended into quaternion wavelet transform (QWT) by employing a quaternionic Haar kernel [20].

The quaternion wavelet transform (QWT) can be considered as a novel multi-scale analysis tool. QWT is derived from the Hilbert 2-D transform theory, which comes close to shift-invariance and subsequently removes the mentioned limitations of CDWT [164]. In addition to shift-invariance, an added advantage of QWT in image analysis is that it encodes image transition in an absolute 2D-coordinates system. Soulard and Carr have proposed an effective method for texture distribution which uses coherent multi-scale analysis derived from the phase data and magnitude information of the QWT [134]. In their method, an overall measure of intensity from the magnitude is incorporated in terms of the statistical deviation of the third angle of QWT phases. It is also noticed that the third phase of quaternionic angles contains structural information that helps in improving the classification. The fractional wavelet transform (FrWT) is defined as a generalization of the wavelet transform in the fractional Fourier domain. In [25], a multi-scale flow estimation algorithm was given for finding the disparity maps in between frames from a video sequence [26]. Kumar et al. [87] proposed a new algorithm for the implementation of the FrQWT using a dual-tree computation structure. The definition of their FrQWT was based on the 2D Fourier spectrum up to a single quadrant and fractional Hilbert operator. The rotation by an arbitrary angle in the time-frequency plane, fractional Fourier transform (FrFT) uniquely illustrates the information of time as well as of frequency domain. However, the wavelet transform has a multiresolution property. The amalgamation of these two results in FrWT which serves as a powerful tool in performing multi-resolution analysis in time as well as transformed domains. Nowadays, subspace decomposition methods [26] play a significant role in the large scale computations. In subspace decomposition, the different frequency parts of the initial noisy image are denoised independently followed by their fusion.

1.3.2.2 Image denoising using wavelet transform

Wavelets give better denoising results because of properties like sparsity and multi-resolution analysis. The thresholding approach was also used for the filtration of noise from the image. Also, the data-adaptive approaches were used to estimate the optimum value of the threshold parameter [46]. Later on, it was found that the quality of a recovered image can be improved using thresholding of an Undecimated Wavelet Transform based methods [33]. Image denoising is based on two primary approaches i.e. methods based on Spatial domain filtering and methods based on Transform domain filtering.

Spatial domain filtering: In spatial domain filtering, the denoising techniques are traditional filtering techniques that can be further categorized into linear and non-linear filtering methods. Linear filters make edge blur and smash the sharp details of images like corners and fine lines. The linear filtering does not perform well if the noise depends on image intensities. The Wiener filter method requires a smooth image and needs data information of the noise spectrum [66]. This method of computational complexity depends on the chosen window size. Thus, Donoho and Johnstone proposed a method to overcome the instability of Wiener filtering. [40, 41]. The non-linear filters remove the noise without determining the type of noise. The weighted median filter [162], rank conditioned rank selection [56], and relaxed median filter [54] are the established filters that reduces the effects of the linear filters which makes edges invisible in the recovered image.

Transform domain filtering: The non-linear thresholding based methods are the most explored methods for image denoising. The thresholding which filters some coefficients below a fixed value and remaining coefficients are undamaged known as hard thresholding [39]. The VISUShrink thresholding technique is non-adaptive [41]. It depends on the number of pixels in an image thus gives a large threshold value. This results in extremely smoothed images. SUREShrink threshold is a combination of the VISUShrink threshold and SURE (Stein's Unbiased Risk Estimator) threshold [41]. BayesShrink threshold is a data-adaptive threshold and gives better performance always when compared to other

thresholds [32, 130]. BayesShrink gives a data-adaptive threshold. Also, wavelet transforms has been used for decomposition of images for better visual effect. The Undecimated Wavelet Transforms are shift-invariant so it prohibits any visual artifacts in the image but it requires large computations, hence, less beneficial for the image restoration process. The wavelet coefficients are modeled using the technique of multi-resolution analysis at various resolutions. The performance of this method is best but it is much more computationally expensive and complicated. There are two types of techniques for modeling of wavelet coefficients viz. Deterministic and Statistical. The deterministic approach uses the tree structure of wavelet coefficients at each resolution [13, 38, 101]. The statistical models use the correlation of wavelet coefficients at different scales and local correlation of the neighborhood wavelet coefficients. The statistical modeling based methods Marginal Probabilistic Model and Joint Probabilistic Model are explained in [28, 103, 122, 130]. The Independent Component Analysis (ICA) scheme gained a lot of consideration in image denoising. It denoises images [74] with Gaussian as well as Non-Gaussian distribution. This method needed some noise-free input and at least two image frames of the same scene. Thus, this method has this drawback of computational complexity when compared to the wavelet transforms based approaches [64, 74].

1.3.2.3 Numerical schemes using Bernoulli and Legendre wavelets

Wavelets has many applications in numerical analysis, time-frequency analysis, optimal control and signal analysis. Wavelets has been used for numerical solutions of ordinary differential equations, partial differential equations, fractional partial differential equations and fractional delay differential equations. In different differential equations, various wavelets have been used such as Legendre, Haar, Bernoulli, Chebyshev wavelets. The fractional order can be used in the sense of Riemann Liouville, Caputo and Grunwald Letnikov, etc. Rahimkhani and Ordokhani presented a numerical collocation scheme using Bernoulli wavelets with fractional order defined in Riemann-Liouville sense [120]. In [60], a numerical scheme for solving partial differential equations with Dirichlet boundary conditions is given using Legendre wavelets. For fractional delay differential equations, an algorithm has been developed

using Bernoulli wavelets collocation method. In [8], different numerical methods has been developed using Haar and Legendre wavelets for elliptic partial differential equations. Jafari et al. [65] proposed a scheme to attain the approximate numerical solutions of fractional order differential equations with fractional order defined in Caputo sense. This method converts fractional order differential equations into algebraic equations and expanded the solution by Legendre wavelets with unknown coefficients.

1.3.2.4 Anisotropic diffusion based methods

The existing algorithms for image denoising lacks an absolute perseverance of the sharp details of the image. On the other hand, the partial differential equations (PDEs) based methods were capable to preserve fine details in the smoothing process up to some extent. The scatter matrix or moment tensor is equivalently developed by Forstner and Gulch [48] as well as by Bigun and Granlund [17] known as structure tensor is highly beneficial in today's image processing and computer vision tasks such as inspecting textures, corners and T-junctions, optical flow estimation and non-linear diffusion filtering using structure tensors. Initially, the partial differential equations (PDEs) based method used for image denoising was the linear heat equation with the homogenous boundary conditions. The linear diffusion filtering is a classical structure tensor that averages in a neighborhood by applying Gaussian convolution on that specific neighborhood. The main objective of the PDEs based method is to overcome noise while keeping the sharp features, corners, etc intact. This method is simple as well as robust. But the main drawback of linear diffusion filtering is that it applies globally on the image which leads to blurring and dislocation of edges and losing sharp features in the image as well.
In the last two decades, anisotropic diffusion is widely used in restoring the images [117, 152]. To tackle this problem, Witkin introduced the scale-space representation [156], based on which Perona-Malik [117] introduced nonlinear PDEs in the image restoration process. Perona-Malik introduced this breakthrough with a new definition of scale-space in which diffusion was induced in such a way that edges are preserved known as anisotropic diffusion (AD). The nonlinear PDEs have demonstrated outstanding results in denoising and in enhancing digital images, however, they endure some severe

flaws. Firstly, they are not as fast as the traditional methods. Secondly, the nonlinear PDEs generally damage some features in images like the tips of cones get flattened. Also, there is no stopping time in the case of nonlinear PDEs based methods. Anisotropic diffusion process can efficiently smooth noise while preserving the boundaries and texture information if its crucial parameters are estimated and applied correctly. This set defines the behavior and extent of the diffusion process.

Anisotropic diffusion is associated with the energy-consuming procedure in which the energy functional is minimized. The resulting images of Perona and Malik anisotropic diffusion are over smoothed and disturbs the position of edges. Rudin-Osher-Fatemi (ROF) [123] introduced an image restoration method based on total variation. The classical ROF model maintains the sharpness of the edges, however, it gives the staircasing effect. In literature, there are many methods for the restoration of images. An energy functional for the multispectral images was introduced in [135]. Zhang et al [171] introduced an inpainting model in which the p-Laplace operator was used. They compared the physical attributes of the total variational model with the p-Laplace operator and concluded that the anisotropic diffusion with the p-Laplace operator gives better results than the TV model [123]. The staircasing effect is also reduced, however, edges are preserved equivalently in both of the models. In [29], the p-Laplace diffusion was introduced with nonlinear regularization depending on the gradient and curvature of the image. In the existing literature, a lot of diffusion equations with the p-Laplace operator emerged which were based on the local operator of the image [36, 85, 98]. These local operators were not so good in order to deal with the texture and the sharp details because the nature of the sharp details is not local generally.

The structure tensor is the robust replacement of the non-linear PDEs based methods such as the Perona-Malik model [19]. Structure tensor has many advantages than non-linear diffusion filtering and regularized models. The non-linear techniques in literature holds for scalar and vector-valued functions, however, structure tensor is a matrix field. The filter proposed by Perona-Malik is isotropic. For the filter to be truly anisotropic, it should consider the direction of edges along with the edge modulus. Thus, Weickert constructed the diffusion tensor such that the eigenvectors displays the projected edge

structures [150]. In this case, the eigenvectors are not parallel to the edge structures which makes this model certainly anisotropic. Structure tensors give influential information about the local image details in comparison to the gradients. In literature, non-linear diffusion schemes based on structure tensor have proved their convenience for strengthening the corners, valleys and in medical imaging [7]. Black et al. [18] suggested another diffusivity function using the Tukeys Biweight concept. This diffusion process could preserve sharp boundaries and better continuity of edges. However, there are many limitations to the above-mentioned models. In 2001, Weickert and Scharr [153] introduced the coherence-enhancing scheme to enhance the structures of flow or wind type. They blended the non-linear diffusion filtering with an orientation study using the standard structure tensor matrix. The eigenvector corresponding to the smallest eigenvalue of the structure tensor determines the coherence orientation. Although in recent time, a handful of extensions have pursued structure tensor with tensor regularization.

1.4 Metrics for image restoration

Efficiency of an image restoration method can be testified using a series of measures. In this thesis, the following measures are used for checking the effectiveness of the proposed algorithms.

1.4.1 Contrast gain

The contrast gain (CG) is defined as,

$$CG = \bar{\mathrm{C}}_{I_r} - \bar{\mathrm{C}}_{I_f} \tag{1.3}$$

where, $\bar{\mathrm{C}}_{I_f}$ and $\bar{\mathrm{C}}_{I_r}$ are the mean contrasts of the degraded and recovered images. The contrast of a pixel is the ratio $C(x,y) = \frac{s(x,y)}{m(x,y)}$,

with

$$m(x,y) = \frac{1}{(2p+1)^2} \sum_{k=-p}^{p} \sum_{l=-p}^{p} I(x+k, y+l)$$

$$s(x,y) = \frac{1}{(2p+1)^2} \sum_{k=-p}^{p} \sum_{l=-p}^{p} |I(x+k, y+l) - m(x,y)|$$

1.4.2 Colorfulness index

The colorfulness index (CI) of a RGB image $I(x,y)$ (having I_R, I_G and I_B bands) is computed as

$$CI = \sqrt{\sigma_{I_1}^2 + \sigma_{I_2}^2} + 0.3\sqrt{\mu_{I_1}^2 + \mu_{I_2}^2} \tag{1.4}$$

where, σ and μ denotes the standard deviation and mean of an image, respectively. The images $I_1 = I_R - I_G$ and $I_2 = \frac{1}{2}[I_R + I_G - I_B]$ are computed using the three color bands of $I(x,y)$.

1.4.3 Contrast-to-noise ratio

Contrast-to-Noise ratio (CNR) is estimated as,

$$CNR = \frac{|I_r - I_d|}{\sigma_N} \tag{1.5}$$

where, I_r and I_d are image intensities for the images I_r and I_d, respectively; and σ_N is the standard deviation of the image noise.

1.4.4 Visible edges ratio

Visible edges ratio (VER) is defined as,

$$e = \frac{n_l - n_k}{n_l} \tag{1.6}$$

where, n_k and n_l are the cardinalities of visible edges in the degraded image and the recovered image respectively.

1.4.5 Structural similarity

Structural similarity (SSIM) between two images I_1 and I_2 is estimated as,

$$SSIM = \frac{(2\mu_x\mu_y + c_1)(2\sigma_{xy} + c_2)}{(\mu_x^2 + \mu_y^2 + c_1)(\sigma_x^2 + \sigma_y^2 + c_2)} \tag{1.7}$$

where,

- μ_x, μ_y are the averages of images I_1 and I_2 respectively.
- σ_x^2 & σ_y^2 are variances of images I_1 and I_2 respectively.
- σ_{xy} is co-variance of I_1 and I_2.

1.4.6 Mean square error

Mean square error (MSE) is defined as,

$$MSE = \frac{1}{MN}\sum_{j=1}^{N}\sum_{i=1}^{M}[I_{orig}(i,j) - I_{res}(i,j)]^2 \tag{1.8}$$

where, I_{orig} and I_{res} are the original and restored images respectively.

1.4.7 Peak signal to noise ratio

Peak signal to noise ratio (PSNR) is calculated as,

$$PSNR = 10\ \log_{10}(\frac{R^2}{MSE}) \tag{1.9}$$

where, R is maximum intensity value in the image.

Here, for the images restored from the foggy/hazy images, the metrics Contrast Gain (CG), Colorfulness Index (CI), Contrast to Noise Ratio (CNR), Visible Edges Ratio (VER) and Structural Similarity (SSIM) are used. However, for images restored using image denoising process, the metrics Structural Similarity (SSIM), Peak Signal to Noise Ratio (PSNR) and Mean Square Error (MSE) are used.

1.5 Structure of the thesis

The work presented in this thesis is divided over the seven different chapters. A chapter-wise description of the work is given in this section.

Chapter 1 presents a general introduction to the topic of image restoration mainly when the degradation occurs due to additive noise and fog/haze. Apart from it, some of the preliminaries and terminologies required in the subsequent chapters are also given. A detailed review of the existing techniques related to these two types of image restoration problems is also summarized with a closer insight into the existing algorithms that are intricately related to the proposed work.

Chapter 2 presents a fog removal algorithm for gray-scale images. In particular, the fractional-order version of the Perona-Malik model is obtained by applying the calculus of the variation technique on the equivalent functional minimization problem. The proposed algorithm uses the airlight map extracted from the foggy model as the initial image in the anisotropic diffusion process. The iterative diffusion process improves this airlight map. The anisotropic diffusion process is generalized to the order of any real number between $[1, 2)$ using the Riemann-Liouville definition of the fractional-order derivatives. The formulation of the iterative process is carried out in the spatial domain to have a simple and computationally efficient implementation. Simulation results validate that the proposed algorithm is outperforming a few of the existing algorithms. The comparison analysis is carried out based on different metrics like contrast gain, colorfulness index, contrast-to-noise ratio, and visible edges ratio.

Chapter 3 presents an algorithm for removing haze/fog from multi-channel images. Again, this algorithm uses a fractional-order anisotropic diffusion equation. However, the p-Laplace norm of the fractional-order gradients is used for adaptive diffusion of the local image details. Apart from it, to deal with different channels, the diffusion equation contains a regularization term to balance the inter-channel correlations and to evade the diffused bands in the recovered image. An iterative numerical scheme is designed to solve the diffusion PDE of this algorithm. The results show the better performance of this algorithm than the fractional-order anisotropic diffusion without any norm and cross channel term. Apart from the natural images, the proposed algorithm is also tested on the synthetic

foggy images from the benchmark data-set namely 'SOT' [93]. This data set containing synthetic haze in indoor images, naturally hazed outdoor images and synthetic hazy outdoor images. The comparison study is carried out using different metrics like contrast gain, colorfulness index, contrast-to-noise ratio, and visible edges ratio. The proposed algorithm would be worthwhile mentioning in need of more accurate image restoration.

In Chapter 4, an image denoising algorithm is proposed using fractional quaternion wavelet transform(FrQWT). In particular, images corrupted with additive Gaussian noise are considered and FrQWT is performed via hard and semi-soft thresholds. The thresholding on the wavelet coefficients reveals the capabilities of wavelet transform in the restoration of an image degraded by noise. FrQWT is simple and adaptive since the estimation of threshold parameters depends on the data of wavelet coefficients. This technique is compared with existing methods of similar category.

In Chapter 5, an improved context-adaptive fractional-order anisotropic diffusion (FOAD) model is proposed specifically for image denoising. The proposed FOAD model also includes a modified version of the diffusion coefficient suggested in the Perona-Malik model. Fractional-order derivative is applied to reduce the stair-casing effect and to preserve the fine characteristics, whereas, the improved diffusion coefficient protects edges and corners from getting over-smoothed. A discrete wavelet transform is used to decompose the image into low-frequency parts and the high-frequency components. Fractional order anisotropic diffusion is applied on the approximation part and detailed parts in some particular directions according to a predefined strategy. The effectiveness of this algorithm is tested on several images with different metrics. The proposed algorithm is found to be quite effective in removing the noise and maintaining the edges and corners.

Chapter 6 presents a new data-driven diffusion coefficient mainly for anisotropic diffusion-based image restoration models. This diffusion coefficient is tested for the sub-problems of image denoising

and image dehazing, showing good performance in both the cases. In the case of image denoising, images are corrupted with additive Gaussian noise (AWGN). The fractional-order derivatives are used in Riemann-Liouville sense which is in principle a convolution of two functions. Apart from it, a more adaptive version of this diffusion coefficient is developed based on the local noise estimation. The efficiency of this algorithm is tested on various noisy/hazy images. Considered images contain a lot of edges and detailed part, however, the proposed algorithm still performs better maintaining sharp details while removing noise and haze.

Chapter 7 has the concluding remarks of the overall work proposed in the thesis. In particular, the advantages of the proposed algorithms together with the limitations and challenges are given. Apart from it, several directions for the future scope of this work are also given in this chapter.

Chapter 2

Single image fog removal algorithm in spatial domain using fractional order anisotropic diffusion

2.1 Introduction

In this chapter, an image defogging algorithm using a fractional-order anisotropic diffusion process is proposed. The proposed algorithm uses the airlight map extracted from the foggy model as the initial image in the anisotropic diffusion process. An iterative diffusion process refines this airlight map. The anisotropic diffusion process is generalized to the order of any real number between $[1, 2)$ using the Riemann-Liouville definition of the fractional-order derivatives. The formulation of the iterative process is carried out in the spatial domain to have a simple and computationally efficient implementation.

In literature, the first category of models was based on the simple image enhancement techniques to restore the foggy images [17]. The second category of the algorithms were based on the use of polarization filters to remove the fog effect from the images [25, 26]. In [28], the algorithm maximizes the local contrast of the image using the Markov-Random-Field (MRF) model. The results were found

impressive except few blocking artifacts around the depth discontinuities (edges). The algorithm proposed in [6] used Independent Component Analysis (ICA). In the third category of the algorithms, Dark-Channel-Prior(DCP) was used to address the defogging of images. Mainly, DCP depends on the statistics of the images of an outdoor scene [10]. Recently, few algorithms use learnable filters to design governing PDEs and associated boundary conditions [3, 19, 20]. Also, several models were proposed using diffusion partial differential equation (PDE) for denoising of digital images [23, 34, 38].

In this chapter, the proposed algorithm refines the airlight map by using a fractional-order anisotropic diffusion (Fr-AD) process. The Fr-AD algorithm is a generalization of classical anisotropic diffusion (AD) [33]. Also, it is a pseudo-PDE-based algorithm between the Perona-Malik model and fourth-order anisotropic diffusion equations [38]. The computations of the fractional derivatives are carried out in the spatial domain instead of the existing Fourier domain-based methods [12]. Additionally, very few parameters are selected manually in the proposed algorithm. These manually tuned parameters do not depend on the image under restoration and remain fixed. The iterative algorithm takes the initial airlight map as the input, and then subsequent iterations derive towards the refined airlight map. The convergence analysis is carried out of the numerical scheme. The presented numerical results validate a better performance of the Fr-AD over some of the existing algorithms.

2.2 Fractional order derivative

Let $f(z)$ be an analytic function in a simple connected region of the complex z- plane $\mathbb{C}$ containing origin. The fractional integral $I_z^{\alpha} f(z)$ of an order α of the function $f(z)$ is defined in [3]. The generalization of the fractional integral can be determined by taking into account the natural $n \in \mathbb{N}$ and real μ in the n-fold integral, and then operating the Cauchy's formula for iterated kernel's $n-1$ times. With this process, the fractional integral operator is given by

$$I_z^{\alpha,\mu} f(z) = \frac{(\mu+1)^{1-\alpha}}{\Gamma(\alpha)} \int_0^z (z^{\mu+1} - \xi^{\mu+1})^{\alpha-1} \xi^{\mu} f(\xi) d\xi. \tag{2.1}$$

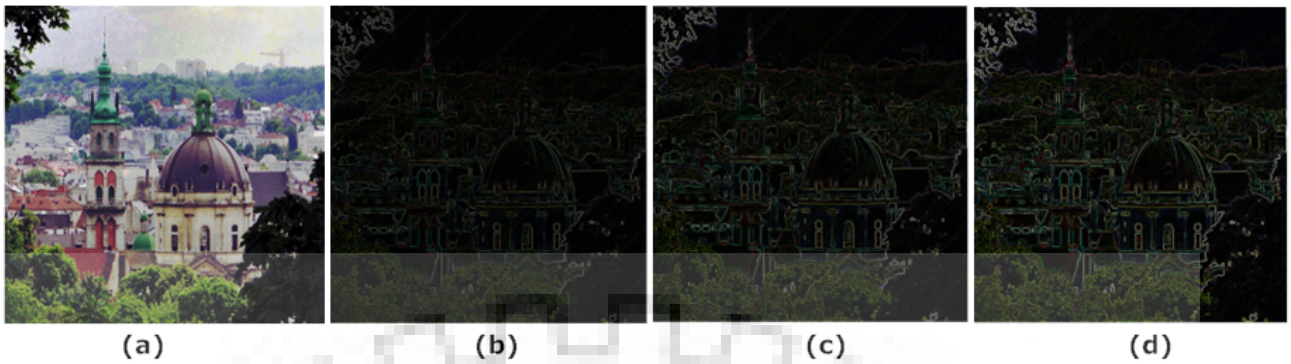

Figure 2.1: Norm of derivatives in x and y direction on initial airlight map of Tomb image for: (a) $\alpha = 1$; (b) $\alpha = 1.4$; (c) $\alpha = 1.8$

where $\alpha, \mu(\neq -1) \in \mathbb{R}$.

When $\mu = 0$, we get the classic Riemann-Liouville fractional integral. Further, Riemann-Liouville fractional derivatives are defined using this fractional integral.

A generalized differential operator of order α resembling to the generalized fractional integral is defined in the following manner

$$D_z^{\alpha,\mu} f(z) = \frac{(\mu+1)^\alpha}{\Gamma(1-\alpha)} \frac{d}{dz} \int_0^z \frac{\xi^\mu}{(z^{\mu+1} - \xi^{\mu+1})^\alpha} f(\xi) d\xi, \quad 0 \leq \alpha < 1 \tag{2.2}$$

$$D_z^\alpha f(z) = \frac{d}{dz}\Big(\frac{z^{-\alpha}}{\Gamma(1-\alpha)} * f(z)\Big) = \frac{d}{dz}\Big(\frac{z^{-\alpha}}{\Gamma(1-\alpha)}\Big) * f(z) \tag{2.3}$$

The partial fractional derivatives with respect to x and y variables are calculated by convoluting the initial airlight map with fixed small size matrices $\begin{bmatrix} -1 & 1 \\ -1 & 1 \end{bmatrix}$ and $\begin{bmatrix} -1 & -1 \\ 1 & 1 \end{bmatrix}$ respectively weighted by using α and a constant viz. 0.25. The derivatives keep refining as per the refinement in airlight map with increasing iterations. The convolution method followed here returns a central part of the convolution that is the same size as the airlight map. Figure 2.1 illustrates the norm of the gradient vector for different fractional orders.

2.3 Image defogging model

In this section, the image defogging model and restoration process is discussed followed by the convergence analysis of the proposed scheme. The most general model to describe an image degraded with fog effect can be expressed as [112, 125, 140]

$$I_0(x,y) = I(x,y)e^{-kd(x,y)} + I_\infty(1 - e^{-kd(x,y)}) \tag{2.4}$$

where, $I(x,y)$ is the original image (intensity at pixel location (x,y) in the absence of fog), k is the coefficient of the scattering related to the atmosphere and $d(x,y)$ is the distance of the scene from camera. The array I_∞ is atmospheric light or sky intensity and $I_0(x,y)$ is the observed foggy image of the scene. Here, $e^{-kd(x,y)}$ is often represented as transmission map and is given by $t(x,y) = e^{-kd(x,y)}$. In clear weather conditions, we have $k \approx 0$. However, k becomes non-negligible in foggy images. In (2.4), the first term $I(x,y)e^{-kd(x,y)}$ is referred as direct attenuation and second term $I_\infty(1 - e^{-kd(x,y)})$ is the airlight map. The decay of the scene radiance in the medium is occurred due to the presence of this direct attenuation term. Generally, scene color is changed due to the diversion in the airlight map. Attenuation is a decreasing function at an exponential rate. This reduces the contrast of the scene. The airlight map $A_0(x,y)$ produces whiteness in the scene. The equation (2.4) can be modified as

$$I_0(x,y) = I(x,y)\Big(1 - \frac{A_0(x,y)}{I_\infty}\Big) + A_0(x,y) \tag{2.5}$$

Normalization is performed on a foggy image for simulation. As effect of the fog is pure white so the sky intensity may be taken as 1 throughout the array, and hence, (2.5) becomes

$$I_0(x,y) = I(x,y)(1 - A_0(x,y)) + A_0(x,y) \tag{2.6}$$

To restore, $I(x,y)$ from its degraded version $I_0(x,y)$, we need to estimate $A_0(x,y)$ accurately. The airlight map $A_0(x,y)$ is a positive scalar map. Generally, outdoor images are colorful (contains trees, purple red plants and blue water), hence, the assumption of using DCP is true in case of natural images. An illustration of the proposed algorithm is given in Figure 2.2.

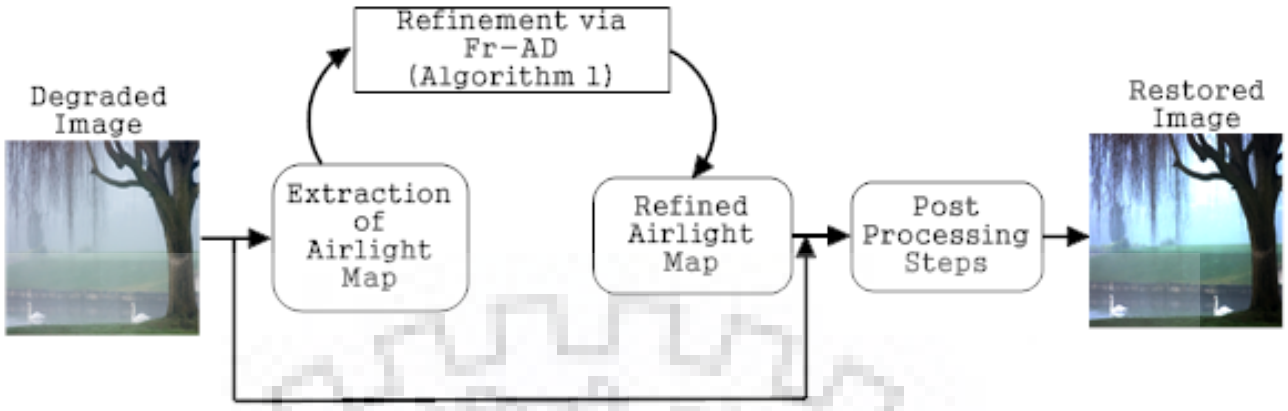

Figure 2.2: An illustration of the proposed algorithm

2.3.1 Implementation

In general, smoothing is considered as one of the impressive technique that has been used in several applications related to the restoration and enhancement of images. Here, the objective is to find a more refined/enhanced airlight map $A(x, y)$, so that the foggy image can be restored using the equation (5.7). If we perform a traditional smoothing filtering approach on $A_0(x, y)$ to get $A(x, y)$, it can contaminate the image features like lines, edges and textures from this initial airlight map. To evade the damage, smoothing has to be robustly controlled by the extent of smoothing and direction of smoothing. Non-linear diffusion theory proposed by Perona and Malik [117] is a classical example of adaptive smoothing, where the smoothing process is defined by PDEs. However, we generalize it to fractional order as the novelty. To do this, fractional-order derivatives are included instead of an integer order derivative. Let g be the diffusion function and t denotes the time, the anisotropic diffusion PDE for refining airlight map is given as

$$\partial_t A = div(g(\nabla A)\nabla A) \tag{2.7}$$

with $A(x, y, 0) = A_0(x, y)\ \forall x \in \Omega$ and $\partial_n A|_{\partial\Omega} = < \nabla A, n > |_{\partial\Omega} = 0$

The equation (2.7) is associated with the energy functional:

$$\mathrm{E}(A) = \int_{\Omega} f(|\nabla A|) d\Omega \tag{2.8}$$

where, Ω stands for image support and $f(.) \geq 0$ is an increasing function associated with the diffusion coefficient defined as

$$g(s^2) = \frac{f'(s)}{s^2} \tag{2.9}$$

Anisotropic diffusion is presented as an energy-consuming function that explores the energy functional minimum. We consider the following functional defined in the space of continuous images over a support of Ω

$$\mathrm{E}(A) = \int_{\Omega} f(|\mathrm{D}^{\alpha} A|) d\Omega \tag{2.10}$$

where D^{α} is the fractional derivative operator defined as $\mathrm{D}^{\alpha} A = (\mathrm{D}_x^{\alpha} A, \mathrm{D}_y^{\alpha} A)$ and $|\mathrm{D}^{\alpha} A| = \sqrt{(\mathrm{D}_x^{\alpha})^2 + (\mathrm{D}_y^{\alpha})^2}$. We can compute the Euler-Lagrange equation for this minimization problem by taking a test function $\eta \in \mathcal{C}^{\infty}(\Omega)$ as follows:

$$\Phi(a) = \int_{\Omega} f(|\mathrm{D}^{\alpha} A + a\mathrm{D}^{\alpha} \eta|) dxdy \tag{2.11}$$

We obtain its derivative at $a = 0$ as

$$\begin{aligned} \Phi'(0) &= \frac{d}{da} \int_{\Omega} f(|\mathrm{D}^{\alpha} A + a\mathrm{D}^{\alpha} \eta|) dxdy|_{a=0} \\ &= \int_{\Omega} \left(f'(|\mathrm{D}^{\alpha} A|) \frac{\mathrm{D}_x^{\alpha} A}{|\mathrm{D}^{\alpha} A|} \mathrm{D}_x^{\alpha} \eta + \right. \\ &\quad \left. f'(|\mathrm{D}^{\alpha} A|) \frac{\mathrm{D}_y^{\alpha} A}{|\mathrm{D}^{\alpha} A|} \mathrm{D}_y^{\alpha} \eta \right) dxdy \\ &= \int_{\Omega} ((\mathrm{D}_x^{\alpha})^* (c(|\mathrm{D}^{\alpha} A|^2) \mathrm{D}_x^{\alpha} A) \\ &\quad + (\mathrm{D}_y^{\alpha})^* (c(|\mathrm{D}^{\alpha} A|^2) \mathrm{D}_y^{\alpha} A)) \eta dxdy \end{aligned} \tag{2.12}$$

for all $\eta \in \mathcal{C}^{\infty}(\Omega)$, where $(\mathrm{D}_x^{\alpha})^*$ and $(\mathrm{D}_y^{\alpha})^*$ are adjoint of D_x^{α} and D_y^{α}, respectively. Hence, the Euler-Lagrange equation becomes

$$(\mathrm{D}_x^{\alpha})^* (c(|\mathrm{D}^{\alpha} A|^2) \mathrm{D}_x^{\alpha} A) + (\mathrm{D}_y^{\alpha})^* (c(|\mathrm{D}^{\alpha} A|^2) \mathrm{D}_y^{\alpha} A) = 0 \tag{2.13}$$

The Euler-Lagrange equation can be solved using the following gradient descent method:

$$\partial_t A = -(\mathrm{D}_x^{\alpha})^* (c(|\mathrm{D}^{\alpha} A|^2) \mathrm{D}_x^{\alpha} A) - (\mathrm{D}_y^{\alpha})^* (c(|\mathrm{D}^{\alpha} A|^2) \mathrm{D}_y^{\alpha} A) \tag{2.14}$$

taking initial condition as the observed airlight map $A_0(x, y)$. The solution is reached as $t \to \infty$ but the growth time can be stopped prior to attain the optimal trade off between fog removal and edge preservation.

When $\alpha = 1$, the equation (2.14) is absolutely the Perona-Malik equation (2.7); when $\alpha = 2$ (2.14) is absolutely the fourth order anisotropic diffusion in [166]; when $1 \leq \alpha \leq 2$, (2.14) leads to a "natural interpolation" between them fulfilling the main motivation of the proposed algorithm.

2.3.2 Numerical algorithm

For practical applications, firstly assume that initial discrete airlight map A_0 is of $m \times m$ pixels. It has been sampled from its continuous version at uniformly spaced points starting at $(0, 0)$, i.e. $A_0(x, y) = A_0(x\Delta x, y\Delta y)$ for $x, y = 0, ..., m-1$. The grid size Δx and Δy is chosen as $\Delta x, \Delta y = 1$.

Let K_1 and K_2 be purely diagonal operators in the spatial domain, defined by

$$\mathrm{K}_1 = \mathrm{F}^{-1}(diag((1 - exp(-j2\pi(\omega_1)/m))^{\alpha} \times exp(j\pi\alpha\omega_1/m)))$$

$$\mathrm{K}_2 = \mathrm{F}^{-1}(diag((1 - exp(-j2\pi(\omega_2)/m))^{\alpha} \times exp(j\pi\alpha\omega_2/m)))$$

where,

$$\mathrm{K}_1^* = \mathrm{F}^{-1}(diag(conj((1 - exp(-j2\pi(\omega_1)/m))^{\alpha} \times exp(j\pi\alpha\omega_1/m)))), \tag{2.15}$$

and

$$\mathrm{K}_2^* = \mathrm{F}^{-1}(diag(conj((1 - exp(-j2\pi(\omega_2)/m))^{\alpha} \times exp(j\pi\alpha\omega_2/m)))). \tag{2.16}$$

We compute the evolution of the initial airlight map A_0 , along flow (2.14) work in the spatial domain only. Moreover, we define

$$h_{xn} = c(|\mathrm{D}^{\alpha} A_n|^2)\mathrm{D}_x^{\alpha} A_n \tag{2.17}$$

and

$$h_{yn} = c(|\mathrm{D}^{\alpha} A_n|^2)\mathrm{D}_y^{\alpha} A_n \tag{2.18}$$

The final output image is recovered using the iterative scheme $u_{n+1} = u_n - g_n \times \Delta t$

where,

$$g_n = \mathrm{K}_1^* \circ h_{xn} + \mathrm{K}_2^* \circ h_{yn}$$

and $\Delta t = 4^{-\alpha}$.

To summarize, the proposed fog removal approach is done in following steps.

Algorithm 1 Numerical implementation of the Fr-AD

Input: Initial airlight map $A(x, y)$, maximum number of iterations n_{max}, α and $\Delta t = 4^{-\alpha}$
Output: Refined airlight map $\widehat{A}(x, y)$

1. Set $n = 0$, input image $u_0 = A(x, y)$, n_{max} and $t = k\Delta t$.
for $n = 0, 1, 2, \ldots, n_{max}$, **do**
2. Compute $\tilde{\mathrm{D}}_x^{\alpha} u_n$ and $\tilde{\mathrm{D}}_y^{\alpha} u_n$ using (2.3).
3. Compute $h_{xn} = c(|\mathrm{D}^{\alpha} u_n|^2)\mathrm{D}_x^{\alpha} u_n$ and $h_{yn} = c(|\mathrm{D}^{\alpha} u_n|^2)\mathrm{D}_y^{\alpha} u_n$ as defined in equations (2.17) and (2.18).
4. Compute $g_n = \mathrm{K}_1^* \circ h_{xn} + \mathrm{K}_2^* \circ h_{yn}$
5. Compute $u_{n+1} = u_n - g_n \times \Delta t$
End for
6. return $\widehat{A}(x, y) = u_n$

2.3.3 Analysis

The iterative scheme defined in the previous section needs to be converged for getting an enhanced airlight map $u = \widehat{A}(x, y)$. In this subsection, we briefly describe the convergence analysis of the scheme. The scheme defined in the Algorithm 1 converges for any choice of the initial image, if the energy function $f(|\nabla^{\alpha} u|)$ defined in equation (2.10) is smooth and convex [135]. Alternatively, there exists a unique solution of the diffusion PDE given in equation (2.14) if energy function defined in equation (2.10) is smooth and convex. From [167],the eigenvalues of the Hessian matrix of the energy function $f(|\nabla^{\alpha} u|)$ can be written as

$$\lambda_1 = \frac{f'(|\nabla^{\alpha} u|)}{|\nabla^{\alpha} u|} \qquad \text{and} \qquad \lambda_2 = f''(|\nabla^{\alpha} u|) \tag{2.19}$$

This gives $\lambda_1 = c(.)$. Here, the value of λ_1 is positive due to our choice of the function $c(s^2) = s^{-1}$, since $f'(s) = s^2.c(s^2)$. To make the anisotropic diffusion problem as a well-posed, the value of second

eigenvalue of the hessian matrix is quite important. In this scheme, we have

$$\lambda_2 = \frac{d}{ds} f'(s) = f''(s) = 1 > 0$$

due to the choice of the edge preserving function $c(s)$. This indicates that the Hessian matrix associated with the integrand of energy function f is positive definite and hence the function is strictly convex. In this case, the function f attains a unique global minima for any choice of initial image $u_0 = A(x, y)$ which is the airlight map extracted from the degraded image.

2.3.4 Post-processing

After estimating airlight map $\hat{A}$, the restored image $I_0(x, y)$ can be restored as

$$I(x, y, c) = \frac{(I_0(x, y, c) - \hat{A}(x, y))}{(1 - (A(x, y)/I_\infty(c)))} \tag{2.20}$$

where $c \in (r, g, b)$. The above method can also be applied for gray-scale images. The only difference will be the initial airlight map.

Histogram stretching is applied as a post-processing step of the proposed algorithm. The restored image $I(x, y, c)$ obtained from the improved airlight map may be of poor contrast. Thus, the restored image may be visually dim because of the difference in the brightness of the scene radiance and the atmospheric light. The later one finds a bit brighter. In general, histogram equalization is a favorite technique for contrast enhancement. However, it may not be that worthy due to the saturated output image of the fog removal step. Moreover, the histogram specification technique cannot be applied due to the absence of a standard reference image. Here, we adopted the histogram stretching in our algorithm for the task of contrast enhancement.

2.4 Results and discussions

This section presents the numerical results obtained with the proposed algorithm to enhance the digital images degraded by the fog effect. The proposed algorithm tests the performance on seven different

Table 2.1: Contrast gain (CG) obtained with the proposed algorithm with different fractional orders α with 30 iterations as stopping criteria.

$\alpha =$	**1.0**	**1.2**	**1.4**	**1.6**	**1.8**
Forest	0.1078	0.1082	**0.1086**	0.1084	**0.1086**
Wheat	0.0852	0.0853	0.0854	0.0854	**0.0856**
Tomb	0.0891	**0.0897**	0.0896	0.0895	0.0893
Ny17	0.1347	0.1351	**0.1352**	0.1351	0.1350
Swan	0.0752	0.0753	0.0753	0.0753	**0.0754**
N6	0.0729	0.0732	0.0734	0.0734	**0.0735**
Train	0.1064	0.1067	**0.1069**	**0.1069**	0.1065

images, namely Forest, Wheat, Tomb, Ny17, Swan, N6 and Train. These images are having different textural details and degraded with varying amounts of the fog. In this study, the fractional-order parameter α takes a real value in the interval $[1,\ 2)$. For the computational purpose, we choose five fixed values of $\alpha = \{1.0,\ 1.2,\ 1.4,\ 1.6,\ 1.8\}$ as taken in many references [9]. It is worth to mention that at $\alpha = 1$, the proposed scheme behaves similarly to AD scheme [146]. In the existing literature, different strategies were adopted to stop the iterative process of anisotropic diffusion. We follow the stopping criteria as in [9]. Four different metrics *contrast gain (CG), colorfulness index (CI)*, *contrast-to-noise ratio (CNR)* and *visible edges ratio (VER)* are used to measure the performance of the proposed algorithm.

The stopping criterion is chosen to be 30 iterations of the diffusion process based on all these metrics. The proposed algorithm uses the airlight map extracted from the degraded image as the initial image of the diffusion process. We compare the performance of the proposed algorithm with some of the existing algorithms such as DCP-based approach [58], Kernel regression model with DCP [158], Two-Layer Gaussian process regression (GPR) [44] and Integer order AD [146].

Table 2.1 lists the numerical results in terms of contrast gain (CG). In case of *Wheat*, *Swan* and *N6* images, fractional order $\alpha = 1.8$ gives the best CG value. For *Forest*, *Ny17* and *Train* images, $\alpha = 1.4$ is giving a slight better CG value. For *Tomb* image, the best CG value is obtained at $\alpha = 1.2$. It is

Table 2.2: Colorfulness index (CI) value obtained with the proposed algorithm with different fractional orders α with 30 iterations as stopping criteria.

$\alpha =$	**1.0**	**1.2**	**1.4**	**1.6**	**1.8**
Forest	0.1178	0.1188	0.1191	**0.1192**	**0.1192**
Wheat	0.0901	0.0905	0.0906	**0.0907**	**0.0907**
Tomb	0.1340	0.1349	0.1351	0.1351	**0.1352**
Ny17	0.4085	0.4122	0.4136	0.4141	**0.4142**
Swan	0.2394	0.2410	0.2416	0.2418	**0.2419**
N6	0.1628	0.1643	0.1648	0.1650	**0.1651**
Train	0.2901	0.2931	0.2941	0.2944	**0.2945**

also worth to mention that the results are significantly improved with fractional orders as compared to the case of $\alpha = 1$ (AD [146]).

The numerical results in terms of colorfulness index (CI) are listed in Table 2.2. The best CI values for all the images are obtained for the fractional orders $\alpha = 1.6$ & 1.8. This is due to the textural details of the image. Unlike the CG value, best CI values are obtained with $\alpha = 1.6$ for *Forest* and *Wheat* images. For the rest of the images, the best performance is found at $\alpha = 1.8$. However, in all these images, Fr-AD gives better results when compared to AD.

Similar types of results are obtained in case of contrast-to-noise ratio. Table 2.3 lists the values of CNR at different fractional orders in case of all these images. It is noticeable that the best results are obtained with fractional orders and not with $\alpha = 1.0$. It is also noticeable from table 2.4 that the FrAD-based approach gives better visible edges ratio (VER) than the AD. From these observations, the significance of fractional order derivatives in anisotropic diffusion can be observed especially in the restoration of fog affected images.

The performance of the proposed algorithm is compared with four different algorithms. Table 2.5 lists the results of this comparison study. We make the following remarks based on this comparison study.

1. In case of contrast gain, the proposed algorithm performs better than other all the four algorithms

Table 2.3: Contrast-to-noise ratio (CNR) obtained with the proposed algorithm with different fractional orders α with 30 iterations as stopping criteria.

$\alpha =$	**1.0**	**1.2**	**1.4**	**1.6**	**1.8**
Forest	19.9636	20.1646	22.1766	23.1968	**24.2256**
Wheat	5.6686	5.9215	6.8548	7.7767	**7.8552**
Tomb	6.0246	7.0256	7.0657	7.0689	**7.0805**
Ny17	5.5305	6.1981	6.2973	6.4577	**6.5920**
Swan	7.8502	8.1070	8.2166	8.4867	**8.6664**
N6	24.1493	25.1423	25.1987	25.2607	**25.3376**
Train	10.1965	10.5583	10.6444	10.7655	**10.8092**

Table 2.4: Visible edges ratio (VER) obtained with the proposed algorithm with different fractional orders α with 30 iterations as stopping criteria.

$\alpha =$	**1.0**	**1.2**	**1.4**	**1.6**	**1.8**
Forest	0.2245	0.2308	0.2308	**0.2326**	0.2289
Wheat	0.2340	0.2372	0.2372	**0.2390**	0.2353
Tomb	0.0123	**0.0263**	**0.0263**	0.0170	0.0193
Ny17	0.1578	0.1586	**0.1609**	**0.1609**	**0.1609**
Swan	0.5390	0.5419	**0.5535**	0.5506	0.5506
N6	0.7825	**0.7899**	**0.7899**	**0.7899**	0.7895
Train	0.2061	0.2121	0.2121	**0.2239**	**0.2239**

for *Forest* and *Tomb* images. The DCP algorithm performs better than the proposed algorithm in case of rest images. For *Ny17, Swan* and *Train* images, the proposed algorithm performs better than the three algorithms KRM, GPR and AD.

2. The proposed algorithm performs better in case of colorfulness index for *Ny17, Swan* and *Train* images. The KRM algorithm performs better than all algorithms for *Forest*, *Tomb* and *N6* images. The GPR algorithm performs best for *Wheat* image.

3. In case of metric CNR, the KRM algorithm performs better for *Tomb, Ny17* and *Swan* images.

Table 2.5: Comparison of the results obtained with existing algorithms DCP [58], KRM [158], GPR [44], AD [146] and the proposed algorithm

Metric	Algorithm	Forest	Wheat	Tomb	Ny17	Swan	N6	Train
CG	DCP	0.0567	**0.1628**	0.0635	**0.1989**	**0.1836**	**0.5418**	**0.3223**
	KRM	0.1040	0.1129	0.0756	0.1084	0.0637	0.0649	0.0967
	GPR	0.0218	0.0222	0.0824	0.1139	0.0561	0.0869	0.0623
	AD	0.1078	0.0852	0.0891	0.1347	0.0752	0.0729	0.1064
	Proposed	**0.1086**	0.0856	**0.0897**	0.1352	0.0754	0.0735	0.1069
CI	DCP	0.1529	0.1470	0.1156	0.1029	0.0965	0.0774	0.0780
	KRM	**1.1639**	0.0736	**2.4508**	0.3255	0.2154	**3.1454**	0.1703
	GPR	0.0927	**0.1578**	0.1252	0.3753	0.1095	0.2269	0.2156
	AD	0.1178	0.0901	0.1340	0.4085	0.2394	0.1628	0.2901
	Proposed	0.1192	0.0907	0.1352	**0.4142**	**0.2419**	0.1651	**0.2945**
CNR	DCP	12.4686	5.6009	10.5319	4.5410	5.7326	9.2940	6.4906
	KRM	11.7421	3.2639	**15.0357**	**12.5265**	**12.6067**	16.2957	7.2043
	GPR	23.2975	**9.6605**	2.4574	7.4326	7.9742	10.4769	8.4515
	AD	19.9636	5.6686	6.0246	5.5305	7.8502	24.1493	10.1965
	Proposed	**24.2256**	7.8552	7.0805	6.5920	8.6664	**25.3376**	**10.8092**
VER	DCP	0.0152	0.0012	0.0042	0.0893	0.2857	0.0573	0.0283
	KRM	0.1870	**0.7134**	**0.1583**	**0.3397**	0.3486	0.3844	**0.2925**
	GPR	0.0730	0.0171	0.0040	0.0674	0.4297	0.2078	0.0261
	AD	0.2245	0.2340	0.0123	0.1578	0.5390	0.7825	0.2061
	Proposed	**0.2326**	0.2390	0.0263	0.1609	**0.5535**	**0.7899**	0.2239

The proposed algorithm gives best results for *Forest, N6* and *Train* images. The GPR algorithm performs best for *Wheat* image. For *Swan* image, the proposed algorithm performs better than the three methods DCP, GPR and AD.

4. The proposed algorithm gives better VER value than DCP, KRM, GPR and AD for images *Forest*, *Swan* and *N6*. The KRM algorithm [158] performs better for other images. In case of visible edges ratio, the proposed algorithm performs better than the three methods DCP, GPR and AD for the images *Wheat, Tomb, Ny17* and *Train*.

Based on the overall comparison of the results, the proposed algorithm is a good choice to restore the foggy images. The computational time taken in the implementation of the proposed diffusion process is compared with a Fourier domain-based algorithm [9]. On a single processor, the proposed algorithm

Table 2.6: Computational time (in seconds) obtained in Fourier domain and by the proposed algorithm in spatial domain

Image	Fourier domain [9]	Proposed(Spatial)
Forest(256×256)	2.986921	1.007776
Wheat(256×256)	2.861586	1.012766
Tomb(256×256)	2.936528	0.985334
Ny17(256×256)	2.850443	1.010316
Swan(256×256)	2.661488	0.896816
N6 (256×256)	2.651796	0.895613
Train(256×256)	2.980296	1.048273

takes less than half of the computational time taken by other algorithms (See Table 2.6). In the case of multi-chip, the Fourier domain-based implementation may be a better choice. The computational complexity of DCP method [57] is of order $\mathcal{O}(m^7)$ [37]. This is mainly because of soft matting otherwise without matting it is of $\mathcal{O}(m^2)$. The complexity of the proposed algorithm Fr-AD is of order $\mathcal{O}(k \cdot m^2)$ on a $m \times m$ image with k number of iterations.

Figure 2.3 gives a qualitative representation of the results obtained with DCP, KRM, GPR and the proposed algorithm. These qualitative results affirm that the restored images with the proposed algorithm are visibly better than the other three existing algorithms. The results obtained with the KRM algorithm [158] has a whiteness along the edges which is smooth in case of the results obtained with the proposed algorithm. Hence, this apparently makes the proposed algorithm a better choice for image restoration where the fog degrades the original images.

2.5 Conclusions

In this chapter, the issue of defogging of the digital images by using a fractional-order generalization of the anisotropic diffusion is addressed. The quality of restored images in the proposed algorithm depends on the diffused airlight map. The proposed algorithm diffuses airlight map visually better when

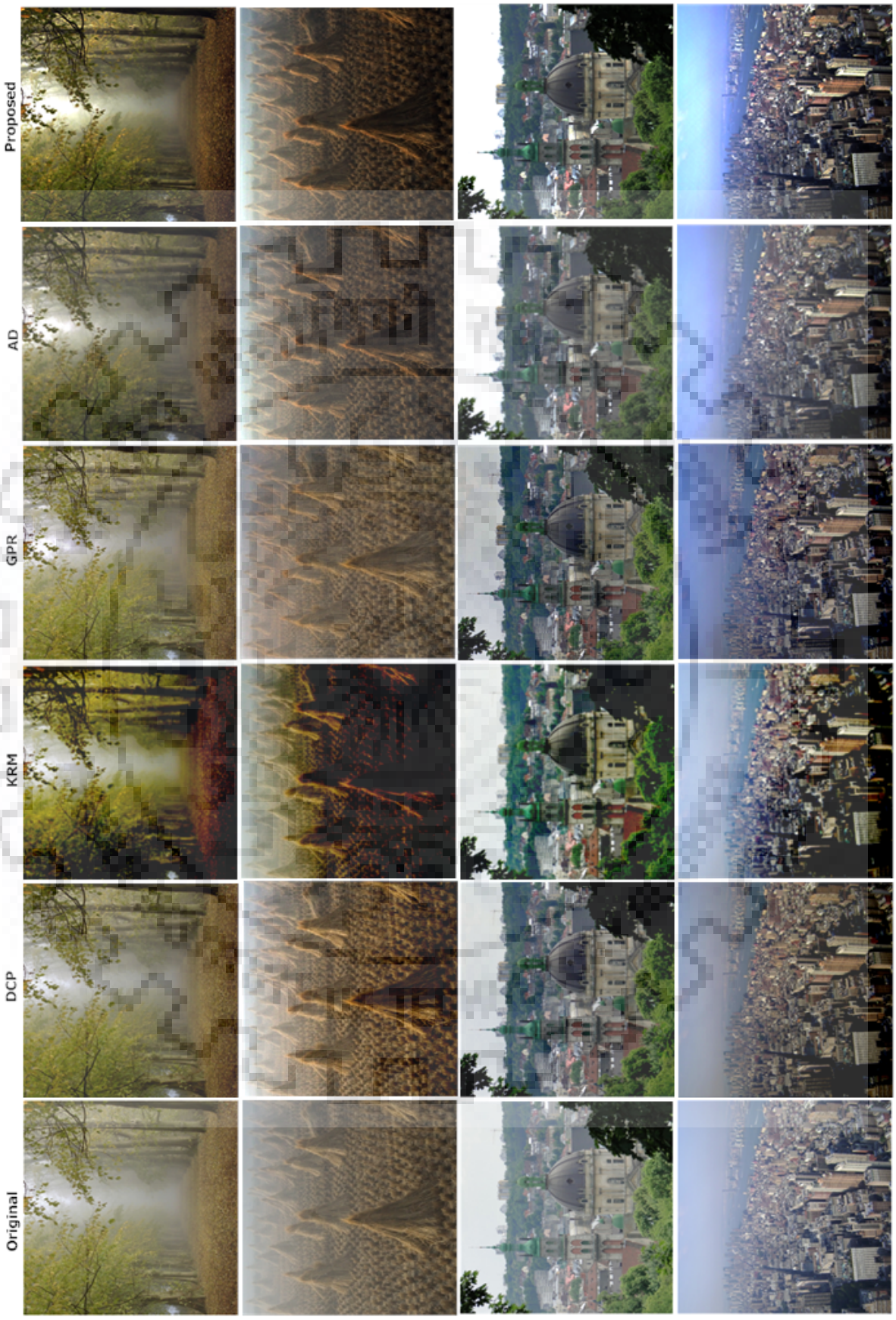

Figure 2.3: The original foggy images are given in first column. Restored images with DCP [58], KRM [158], GPR [44] and the proposed algorithm are shown in second, third, fourth and fifth columns, respectively.

Figure 2.4: The original foggy images are given in first column. Restored images with DCP [58], KRM [158], GPR [44] and the proposed algorithm are shown in second, third, fourth and fifth columns, respectively.

compared to classical anisotropic diffusion. The proposed algorithm gives restored images better than some of the benchmark algorithms based on different metrics. The computation of the fractional-order derivatives in the proposed algorithm takes lower computational efforts when compared to a Fourier domain-based implementation. In this chapter, five fixed values between $[1,\ 2)$ are considered for computing fractional-order derivatives. In the next chapter, the algorithm in this chapter is extended to multichannel images with a regularization term to balance the inter-channel correlations.

Chapter 3

Fractional order anisotropic diffusion for defogging of RGB images

3.1 Introduction

This chapter proposes a new algorithm for removing fog from multichannel images. Here, we implement the proposed algorithm on color(RGB) images having three channels. The fog in a scene is mostly due to the attenuation and airlight map which decreases the quality of the image of the scene. In particular, to enhance such images from the visual point of view, the proposed fractional-order anisotropic diffusion algorithm includes a p-Laplace norm to remove the fog and a coupling term to model the inter-channel correlations. The weights used in the coupling term stop the transmission of diffusion within the edges, hence balances the inter-channel data in the overall diffusion procedure. Experimental results validate the better performance of the proposed algorithm over some of the existing anisotropic diffusion-based methods. The proposed algorithm is independent of the measure of fog in the images, thus images with different amount of fog can be enhanced.

In the last two decades, anisotropic diffusion is a widely used technique in restoring the images [117, 152]. Anisotropic diffusion is associated with the energy-consuming procedure in which the energy

functional is minimized. Consider the energy functional [165]

$$\min_u E(u) = \frac{1}{p}\int_\Omega g(|\mathrm{D}^\alpha u|^p)d\Omega \tag{3.1}$$

Here, $1 \leq p \leq 2$. Ω is the image support. The function $g : [0, \infty] \to \mathrm{R}$ is a smooth increasing function with $g(|\mathrm{D}^\alpha u|) = 0$ when $|\mathrm{D}^\alpha u| = 0$. In equation (5.6), u_{min} is used to determine the image on the compact support Ω so that the energy function $E(u)$ has a minimum value. For $p = 2$ and $\alpha = 1$, equation (5.6) converts into the classical anisotropic diffusion scheme proposed by Perona and Malik [117]. The resulting images of Perona and Malik anisotropic diffusion are over smoothed and disturbs the position of edges. For $p = 1$, equation (5.6) is the classical Rudin, Osher, and Fatemi (ROF) [123] model which maintains the sharpness of the edges, however, it gives the staircasing effect. Therefore, to reduce the staircasing effect, appropriate values of p can be chosen. Thus considering the value of p in the interval $(1, 2)$ gives the diffusion in between the total variation and the more generic the fourth-order anisotropic diffusion. An energy functional for the multispectral images was introduced in [135]

$$\min_u E(I) = \int_\Omega \phi(|\nabla I^i|)d\Omega + \lambda\sum_{j=1}^{N}\int_\Omega [(\omega^i \mathrm{D}I^j - \omega^j \mathrm{D}I^i)]^2 d\Omega \tag{3.2}$$

Zhang et al [171] introduced an inpainting model in which the p-Laplace operator was used. They compared the physical attributes of the total variational model with p-Laplace operator and concluded that the anisotropic diffusion with p-Laplace operator gives better results than the TV model [123]. The staircasing effect is also reduced, however, edges are preserved equivalently in both of the models. In [29], the p-Laplace diffusion was introduced with nonlinear regularization depending on the gradient and curvature of the image. In the existing literature, some diffusion equations with the p-Laplace operator emerged which were based on the local operator of the image [36, 85, 98]. These local operators were not so good to deal with the texture and the sharp details because the nature of the sharp details is not local generally.

The fractional-order diffusion equations accommodate in between the first order TV models and the models with the higher-order derivatives. The methods with exponent as fractional order have applications in many fields such as image inpainting [172], image denoising [34, 73, 118], enhancement

of texture and other details [148, 149]. In addition, fractional-order derivatives have global property, therefore they acquire not just the local property but the attributes of the whole function.

In the previous chapter, a fractional-order anisotropic diffusion algorithm for removing fog from gray images is given. In that approach, each band/channel of the image have been diffused independently. However, in this chapter, a regularization term is added to avoid the diffusion of different channels in the recovered image. The weights in the coupling term stops the transmission of diffusion near edges. This maintains the inter-channel correlations for color or multispectral images. The mathematical and visual results show the efficiency of the proposed model irrespective of the amount of haze in outdoor as well as indoor synthetic hazy images and naturally hazy images.

3.2 Proposed model

3.2.1 Diffusion PDE

Let $I : \Omega \subset \mathrm{R}^2 \to \mathrm{R}^3$ be a color (RGB) foggy image having three channels. Here, Ω is the domain of the initial image $I = (I^R, I^G, I^B)$. The mathematical form of Perona-Malik anisotropic diffusion for $i = R, G, B$ and $x \in \Omega$ is

$$\partial_t I^i = div(g(|\nabla I^i|)\nabla I^i); \quad I^i(x, 0) = I_0^i(x). \tag{3.3}$$

where, the rate of diffusion is controlled by the function $g : \mathrm{R}^+ \cup 0 \to \mathrm{R}^+ \cup 0$ known as flux function and $I_0 = (I^R, I^G, I^B)$ is the initial degraded image. The channel-wise approach in Perona-Malik anisotropic diffusion given in equation (3.3) overlooks the interchannel correlations occurring in the color images. This leads to the diffused and blended bands in the final image. Therefore, a regularization term is added to the right-hand side of the Perona-Malik diffusion equation to evade the diffusion of bands. For which the coupled PDE is given as [135]

$$\partial_t I^i = div(g(|\nabla I^i|)\nabla I^i) + \alpha \sum_{j=1}^{3} (\omega^i \Delta I^j - \omega^j \Delta I^i); \quad i = 1, \cdots, 3. \tag{3.4}$$

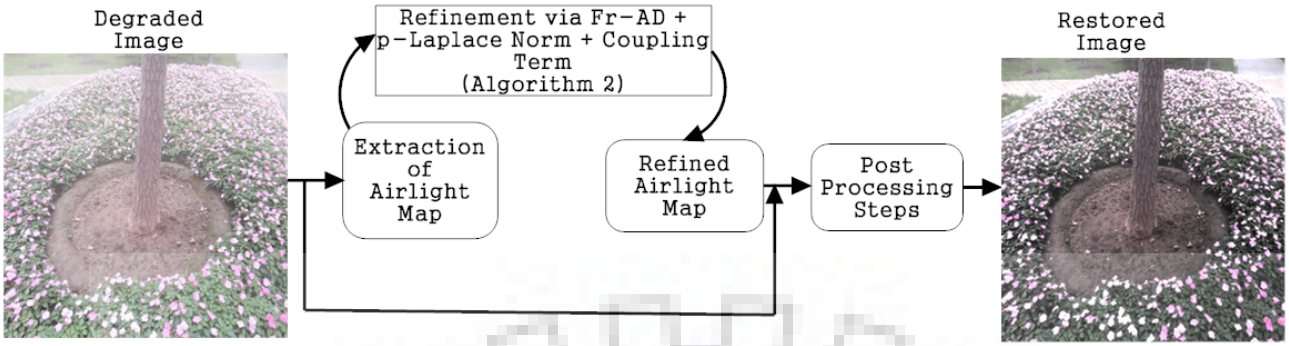

Figure 3.1: An illustration of the proposed algorithm

These weights are chosen in the adaptive manner as follows:

$$\omega^i = \nabla_\rho I_0^i = G_\rho * \nabla {I_0}^i \tag{3.5}$$

where $*$ represents the convolution function and the Gaussian kernel $G_\rho = \frac{1}{2\pi\rho} exp{-}(|x|^2)/2\rho$ is used to smooth the initial image. An interpretation of the proposed algorithm is shown in Figure 3.1.

3.2.2 Proposed model

The proposed fractional PDE for the anisotropic diffusion of color images is given as

$$\partial_t A^i = div(g(|\nabla^\alpha A^i|^p)\nabla^\alpha A^i) + \lambda \sum_{j=1}^{3} (\omega^i \Delta^\alpha A^j - \omega^j \Delta^\alpha A^i), \quad i = R, G, B \tag{3.6}$$

together with initial condition $A^i(\Omega, 0) = A_0^i(x, y)$ obtained from the i^{th} channel of the initial airlight map, and A^i denotes the diffused/filtered version of the i^{th} channel of the airlight map. Here, initial airlight map $A_0(x, y)$ is extracted from the foggy image $I_0(x, y)$ for each channel separately. A detailed description about the relation between airlight map, foggy image and the recovered image has been described in Chapter 2.

The energy functional for the equation (3.6) is given by

$$\mathrm{E}(A) = \frac{1}{p} \int_\Omega \phi(|\mathrm{D}^\alpha A^i|^p) d\Omega + \lambda \sum_{j=1}^{3} \int_\Omega [(\omega^i \mathrm{D}^\alpha A^j - \omega^j \mathrm{D}^\alpha A^i)]^2 d\Omega, \quad \alpha, p \in [1, 2) \tag{3.7}$$

Here, g is an increasing function correlated with the diffusion coefficient function as

$$g(s^2) = \frac{f'(s)}{s^2}. \tag{3.8}$$

The adaptive factor p which depends on the local features of an image is defined as [29, 165]

$$p = 1 + \frac{curv^{\alpha}}{curv^{\alpha} + |\mathrm{D}^{\alpha} A^i|}$$

and

$$curv^{\alpha} = div^{\alpha}\left(\frac{\mathrm{D}^{\alpha} A^i}{|\mathrm{D}^{\alpha} A^i|}\right) = (-1)^{\alpha}\left(\mathrm{D}_x^{\alpha *}\left(\frac{\mathrm{D}^{\alpha} A^i}{|\mathrm{D}^{\alpha} A^i|}\right) + \mathrm{D}_y^{\alpha *}\left(\frac{\mathrm{D}^{\alpha} A^i}{|\mathrm{D}^{\alpha} A^i|}\right)\right)$$

where, $\mathrm{D}_x^{\alpha *}$ and $\mathrm{D}_y^{\alpha *}$ are adjoints of gradients D_x^{α} and D_y^{α} in x and y directions respectively. Now, consider any test function $\eta^i \in \mathcal{C}^{\infty}(\Omega)$ for each channel and then define a new function $\Phi(a)$ is defined as

$$\Phi(a) = \frac{1}{p}\int_{\Omega} (\phi(|\mathrm{D}^{\alpha} A^i + a\mathrm{D}^{\alpha}\eta^i)|^p + \lambda \sum_{j=1}^{3} (\omega^i(\mathrm{D}^{\alpha} A^j + a\mathrm{D}^{\alpha}\eta^j) - \omega^j(\mathrm{D}^{\alpha} A^i + a\mathrm{D}^{\alpha}\eta^i))^2) d\Omega. \tag{3.9}$$

Then, the necessary condition to have an extremum gives

$$\begin{aligned}
\Phi'(a)|_{a=0} = & \int_{\Omega}\left(\phi'(|\mathrm{D}^{\alpha} A^i + a\mathrm{D}^{\alpha}\eta^i|^p)\frac{\mathrm{D}_x^{\alpha} A^i + a\mathrm{D}_x^{\alpha}\eta^i}{|\mathrm{D}_x^{\alpha} A^i + a\mathrm{D}_x^{\alpha}\eta^i|^{1-p}}\mathrm{D}_x^{\alpha}\eta^i\right) d\Omega|_{a=0} \\
& + \int_{\Omega}\left(\phi'(|\mathrm{D}^{\alpha} A^i + a\mathrm{D}^{\alpha}\eta^i|^p)\frac{\mathrm{D}_y^{\alpha} A^i + a\mathrm{D}_y^{\alpha}\eta^i}{|\mathrm{D}_y^{\alpha} A^i + a\mathrm{D}_y^{\alpha}\eta^i|^{1-p}}\mathrm{D}_y^{\alpha}\eta^i\right) d\Omega|_{a=0} \\
& + 2\lambda \sum_{j=1}^{3} (\omega^i(\mathrm{D}^{\alpha} A^j + a\mathrm{D}^{\alpha}\eta^j) - \omega^j(\mathrm{D}^{\alpha} A^i + a\mathrm{D}^{\alpha}\eta^i)) \\
& \left[\omega^i \frac{\mathrm{D}_x^{\alpha} A^j + a\mathrm{D}_x^{\alpha}\eta^j}{|\mathrm{D}_x^{\alpha} A^j + a\mathrm{D}_x^{\alpha}\eta^j|}\mathrm{D}_x^{\alpha}\eta^j - \omega^j \frac{\mathrm{D}_x^{\alpha} A^i + a\mathrm{D}_x^{\alpha}\eta^i}{|\mathrm{D}_x^{\alpha} A^i + a\mathrm{D}_x^{\alpha}\eta^i|}\mathrm{D}_x^{\alpha}\eta^i\right. \\
& \left. + \omega^i \frac{\mathrm{D}_y^{\alpha} A^j + a\mathrm{D}_y^{\alpha}\eta^j}{|\mathrm{D}_y^{\alpha} A^j + a\mathrm{D}_y^{\alpha}\eta^j|}\mathrm{D}_y^{\alpha}\eta^j - \omega^j \frac{\mathrm{D}_y^{\alpha} A^i + a\mathrm{D}_y^{\alpha}\eta^i}{|\mathrm{D}_y^{\alpha} A^i + a\mathrm{D}_y^{\alpha}\eta^i|}\mathrm{D}_y^{\alpha}\eta^i\right] d\Omega|_{a=0}
\end{aligned} \tag{3.10}$$

After simplifying the above equation and putting $a = 0$, we get

$$\begin{aligned}
\Phi'(a)|_{a=0} = & \int_{\Omega}\left[(\mathrm{D}_x^{\alpha})^*\left(c(|\mathrm{D}^{\alpha} A^i|^{2p})\frac{\mathrm{D}_x^{\alpha} A^i}{|\mathrm{D}^{\alpha} A^i|^{1-2p}}\right) + (\mathrm{D}_y^{\alpha})^*\left(c(|\mathrm{D}^{\alpha} A^i|^{2p})\frac{\mathrm{D}_y^{\alpha} A^i}{|\mathrm{D}^{\alpha} A^i|^{1-2p}}\right)\right]\eta^i d\Omega + \\
& \sum_{j=1}^{3} 2\lambda[\omega^i(\mathrm{D}^{\alpha} A^j) - \omega^j(\mathrm{D}^{\alpha} A^i)][\omega^i(\mathrm{D}_x^{\alpha} A^j \mathrm{D}_x^{\alpha *} + \mathrm{D}_y^{\alpha} A^j \mathrm{D}_y^{\alpha *}) - \omega^j(\mathrm{D}_x^{\alpha} A^i \mathrm{D}_x^{\alpha *} + \mathrm{D}_y^{\alpha} A^i \mathrm{D}_y^{\alpha *})]\eta^i d\Omega
\end{aligned} \tag{3.11}$$

where, the function $\eta(x, y) \in \mathcal{C}^{\infty}(\Omega)$. Also, $\mathrm{D}_x^{\alpha *}$ and $\mathrm{D}_y^{\alpha *}$ are the adjoint of functions D_x^{α} and D_y^{α} respectively. Now, since the function η is arbitrary, we will have the Euler-Lagrange's equations as

follows

$$(\mathrm{D}_x^\alpha)^*\left(c(|\mathrm{D}^\alpha A^i|^{2p})\frac{\mathrm{D}_x^\alpha A^i}{|\mathrm{D}^\alpha A^i|^{1-2p}}\right)+(\mathrm{D}_y^\alpha)^*\left(c(|\mathrm{D}^\alpha A^i|^{2p})\frac{\mathrm{D}_y^\alpha A^i}{|\mathrm{D}^\alpha A^i|^{1-2p}}\right)+ \sum_{j=1}^{3}2\lambda[\omega^i(\frac{\mathrm{D}^\alpha A^j}{\mathrm{D}^\alpha A})-\omega^j(\frac{\mathrm{D}^\alpha A^i}{\mathrm{D}^\alpha A})][\omega^i(\mathrm{D}_x^\alpha A^j\mathrm{D}_x^{\alpha*}+\mathrm{D}_y^\alpha A^j\mathrm{D}_y^{\alpha*})-\omega^j(\mathrm{D}_x^\alpha A^i\mathrm{D}_x^{\alpha*}+\mathrm{D}_y^\alpha A^i\mathrm{D}_y^{\alpha*})]=0 \tag{3.12}$$

The Euler-Lagrange's equations can be solved by using the gradient descent method and given as

$$\partial_t A^i=-(\mathrm{D}_x^\alpha)^*\left(c(|\mathrm{D}^\alpha A^i|^{2p})\frac{\mathrm{D}_x^\alpha A^i}{|\mathrm{D}^\alpha A^i|^{1-2p}}\right)-(\mathrm{D}_y^\alpha)^*\left(c(|\mathrm{D}^\alpha A^i|^{2p})\frac{\mathrm{D}_y^\alpha A^i}{|\mathrm{D}^\alpha u^i|^{1-2p}}\right) -\sum_{j=1}^{3}2\lambda[\omega^i(\frac{\mathrm{D}^\alpha A^j}{\mathrm{D}^\alpha A^i})-\omega^j(\frac{\mathrm{D}^\alpha A^i}{\mathrm{D}^\alpha A^i})][\omega^i(\mathrm{D}_x^\alpha A^j\mathrm{D}_x^{\alpha*}+\mathrm{D}_y^\alpha A^j\mathrm{D}_y^{\alpha*})-\omega^j(\mathrm{D}_x^\alpha A^i\mathrm{D}_x^{\alpha*}+\mathrm{D}_y^\alpha A^i\mathrm{D}_y^{\alpha*})] \tag{3.13}$$

An algorithmic implementation of the above procedure is summarized briefly in Algorithm 2. Here, all the computational steps for implementing the proposed methodology are described from the view of numerical computation.

Algorithm 2 Computational algorithm for fractional order anisotropic diffusion with p-Laplace term

Step 1: Set input airlight map A_0 as u_0, k, Δt and $t=k\Delta t$.
Step 2: Compute α -order fractional derivatives $\tilde{\mathrm{D}}_x^\alpha A_n$ and $\tilde{\mathrm{D}}_y^\alpha A_n$ using (2.3)
Step 3: Compute
$h_{x,y}^\alpha=(\mathrm{D}_x^\alpha)^*\left(c(|\mathrm{D}^\alpha A^i|^{2p})\frac{\mathrm{D}_x^\alpha A^i}{|\mathrm{D}^\alpha A^i|^{1-2p}}\right)+(\mathrm{D}_y^\alpha)^*\left(c(|\mathrm{D}^\alpha A^i|^{2p})\frac{\mathrm{D}_y^\alpha A^i}{|\mathrm{D}^\alpha A^i|^{1-2p}}\right)$
Step 4: Compute $s_{x,y}^\alpha=\sum_{j=1}^{3}2\lambda[\omega^i(\frac{\mathrm{D}^\alpha A^j}{\mathrm{D}^\alpha A^i})-\omega^j(\frac{\mathrm{D}^\alpha A^i}{\mathrm{D}^\alpha A^i})][\omega^i(\mathrm{D}_x^\alpha A^j\mathrm{D}_x^{\alpha*}+\mathrm{D}_y^\alpha A^j\mathrm{D}_y^{\alpha*})-\omega^j(\mathrm{D}_x^\alpha A^i\mathrm{D}_x^{\alpha*}+\mathrm{D}_y^\alpha A^i\mathrm{D}_y^{\alpha*})]$ as in (3.13)
Step 5: Compute $g_n=h_{x,y}^\alpha+s_{x,y}^\alpha$
Step 6: Set iteration $A_{n+1}=A_n-g_n\times\Delta t$ and set $n=n+1$; if $n=k$, stop; else go to 2)

3.2.3 Restoration and post-processing

After getting the diffused airlight map $A^i(x,y)$ using the above algorithm, the final image can be recovered as

$$I^i(x,y)=\frac{({I_0}^i(x,y,i)-A^i(x,y))}{(1-(A^i(x,y)/I_\infty(i)))} \tag{3.14}$$

where i stands for the color channels. Since, the refined airlight map has lower contrast, therefore, histogram stretching has been used to increase the contrast of the final image.

3.3 Convergence analysis

The scheme defined in the Algorithm 2 converges independent of choice of the initial image, if the energy function $f(|\nabla^{\alpha}u|)$ defined in equation (3.7) is smooth and convex [135]. Also, if energy function defined in equation (3.7) is smooth and convex, the diffusion PDE given in equation (3.13) will have unique solution. From [167],the eigenvalues of the Hessian matrix of the energy function $f(|\nabla^{\alpha}u|)$ can be written as

$$\lambda_1 = \frac{f'(|\nabla^{\alpha}I_0|)}{|\nabla^{\alpha}I_0|} \qquad \text{and} \qquad \lambda_2 = f''(|\nabla^{\alpha}I_0|) \tag{3.15}$$

This gives $\lambda_1 = c(.)$. Here, the value of λ_1 is positive due to our choice of the function $c(s^2) = s^{-1}$, since $f'(s) = s^2.c(s^2)$. To make the anisotropic diffusion problem as a well-posed, the value of second eigenvalue of the hessian matrix is quite important. In this scheme, we have

$$\lambda_2 = \frac{d}{ds}f'(s) = f''(s) = 1 > 0$$

due to the choice of the edge preserving function $c(s)$. This indicates that the Hessian matrix associated with the integrand of energy function f is positive definite and hence the function is strictly convex. In this case, the function f attains a unique global minima for any choice of initial image $u_0 = A(x, y)$ which is the airlight map extracted from the degraded image.

3.4 Simulation and results

In this section, image restoration results are shown from numerical and visual perspectives. The proposed algorithm is evaluated on seven indoor images having synthetic haze namely *Cable*, *Playtable*, *Kitchen*, *Door*, *Basin*, *Girl* and *Wall*. The measure of fog is dense in all these images, however, the proposed algorithm works well for all the cases. In our experimental study, we have implemented the proposed algorithm using the fractional-order viz. $\alpha = 1.2$, 1.4, 1.6 and 1.8. The proposed algorithm is executed in the MatLab environment. To check the feasibility of the algorithm, the metrics like Contrast gain, Visible edges ratio, Colorfulness index and Structural similarity are used for all of the

Table 3.1: Contrast gain (CG) obtained with the proposed algorithm with different fractional orders α with 30 iterations as stopping criteria.

$\alpha =$	**1.0**	**1.2**	**1.4**	**1.6**	**1.8**
Cable	0.1452	0.1601	0.1949	0.2317	**0.2363**
PlayTable	0.1180	0.1192	0.1231	0.1285	**0.1302**
Kitchen	0.1225	0.1232	0.1247	0.1266	**0.1271**
Door	0.1376	0.1384	0.1393	0.1400	**0.1401**
Basin	0.1175	0.1174	0.1184	0.1196	**0.1199**
Girl	0.1222	0.1231	0.1250	0.1305	**0.1337**
Wall	0.1752	0.1764	0.1787	0.1850	**0.1881**

Table 3.2: Visible edges ratio (VER) obtained with the proposed algorithm with different fractional orders α with 30 iterations as stopping criteria.

$\alpha =$	**1.0**	**1.2**	**1.4**	**1.6**	**1.8**
Cable	0.0057	0.0278	0.0437	**0.0933**	0.0789
PlayTable	0.0704	0.0704	0.0812	**0.0923**	0.0812
Kitchen	0.2824	0.2907	0.2865	0.2907	**0.2948**
Door	0.0867	0.0923	**0.0979**	0.0867	0.0867
Basin	0.8279	0.8333	0.8333	**0.9038**	0.8333
Girl	0.2004	**0.2042**	**0.2042**	**0.2042**	0.2008
Wall	0.4206	**0.4308**	0.4264	0.4219	0.4219

images with different fractional orders. The stopping criteria is chosen as 30 iterations in this study as no significant diffusion is noticed after the 30 iterations. Table 3.1 shows the numerical results for the metric Contrast gain. The contrast gain should be higher for the recovered images as compared to the foggy image. In the case of all these images, contrast gain (CG) is increasing with the fractional orders as compared to the integer-order. Also, maximum CG is obtained with the fractional order 1.8. The numerical results for the metric Visible edges ratio (VER) are shown in Table 3.2. The maximum VER for images Cable, Playtable and Basin is obtained at fractional-order 1.6. For Wall image, the maximum VER value is found at fractional-order 1.2. However, the fractional-order VER values are

Table 3.3: Colorfulness index (CI) obtained with the proposed algorithm with different fractional orders α with 30 iterations as stopping criteria.

$\alpha =$	**1.0**	**1.2**	**1.4**	**1.6**	**1.8**
Cable	0.3017	0.3704	0.4769	**0.5477**	0.5329
PlayTable	1.1837	1.1956	1.2399	1.3171	**1.6053**
Kitchen	0.7750	0.7884	0.8500	0.9415	**0.9649**
Door	0.5865	0.5938	0.6122	0.6289	**0.6323**
Basin	0.2332	0.2637	0.3732	0.4061	**0.5968**
Girl	0.2933	0.3026	0.3348	0.4237	**0.4936**
Wall	0.8439	0.8657	0.9734	1.4365	**1.7743**

better than the integer-order in other images also. Similar results are obtained in the case of metric Colorfulness index. Table 3.3 lists the values of CI at different fractional orders in case of all these images. It can be noted that the fractional-order gives better results as compared to the integer-order for all of the images.

To test the importance of the fractional orders-based diffusion and additional cross-channel term, a comparison study is listed in Table 3.4. In this table, the results obtained with the proposed algorithm are compared with the following four algorithms:

1. Dark channel prior (DCP) [57].
2. Fractional order anisotropic diffusion without p-Laplace term and without cross channel diffusion (FrAD) [111].
3. Integer order anisotropic diffusion with cross channel term (ADC) as proposed in [135].
4. Fractional order anisotropic diffusion with p-Laplace norm (FrADP).

DCP performs better for *Door* image in case of metrics CG and VER. It can be seen that the proposed algorithm performs better than the above listed four algorithms in case of the other three comparison metrics. Hence, the inclusion of cross channel term with fractional order gradients is effective to remove fog from color images. Figure 3.2 and figure 3.3 shows the visual results of the considered images. The

Table 3.4: Comparison of the results obtained with existing algorithms DCP [57], FrAD [111], ADC [135], FrADP and the proposed algorithm

Metric	Algorithm	Cable	Playtable	Kitchen	Door	Basin	Girl	Wall
CG	DCP	0.0549	0.0898	0.0884	**0.1556**	0.0382	0.0935	0.0837
	FrAD	0.1790	0.1160	0.0987	0.1310	0.1022	0.1173	0.1427
	ADC	0.1499	0.1081	0.0772	0.1121	0.0844	0.0889	0.1054
	FrADP	0.1845	0.1275	0.1260	0.1363	0.1175	0.1279	0.1767
	Proposed	**0.2363**	**0.1302**	**0.1271**	0.1401	**0.1199**	**0.1337**	**0.1881**
VER	DCP	0.0209	0.0306	0.2751	**0.1322**	0.2035	0.0422	0.2177
	FrAD	0.0521	0.0571	0.1684	0.0130	0.8514	0.0199	0.2323
	ADC	0.0555	0.0916	0.2237	0.0874	0.9028	0.0277	0.2788
	FrADP	0.0825	0.0836	0.2419	0.0821	0.8608	0.2005	0.2366
	Proposed	**0.0933**	**0.0923**	**0.2948**	0.0979	**0.9038**	**0.2042**	**0.4308**
CI	DCP	0.2436	0.2334	0.0991	0.0987	0.0891	0.1470	0.0719
	FrAD	0.3394	1.5538	0.6799	0.5551	0.4673	0.4363	1.1878
	ADC	0.4489	0.5579	0.2177	0.2861	0.2281	0.2012	0.2766
	FrADP	0.4262	1.5352	0.7976	0.6255	0.2903	0.3775	0.8546
	Proposed	**0.5477**	**1.6053**	**0.9649**	**0.6323**	**0.5968**	**0.4936**	**1.7743**

first column shows the initially foggy image, the second column shows the recovered images using DCP [57], third and fourth columns show the images obtained using FrAD [111] and ADC [135] respectively. The fifth and sixth columns show the recovered images using FrADP and the proposed algorithm respectively and the last column is the ground truth images of the considered foggy images. For the 30 iterations, we get the optimum visual and quantitative results with each fractional order on all of the images. It can be clearly seen in the qualitatively results that the images recovered with method ADC [135] are overly enhanced. This can be observed as there is much difference in the recovered image as compared to the ground truth image. This is not a case with the proposed algorithm. Also, the defoggy images using the proposed algorithm are very much similar to the respective ground truth images. Thus the proposed algorithm has better defogging results than the other techniques.

The proposed algorithm is performed on the outdoor images also. Considered images are Forest, Wheat, Tomb, Ny17, Swan, N6 and Train. Table 3.5 shows the results for the metric Contrast gain (CG) with different fractional orders in range $[1, 2)$. It can be seen from Table 3.5 that the CG value

Figure 3.2: The original foggy images are given in first column. Restored images with DCP [57], FrAD [111], ADC [135], FrADP and the proposed algorithm are shown in second, third, fourth, fifth and sixth columns, respectively. The last column shows the ground truth images.

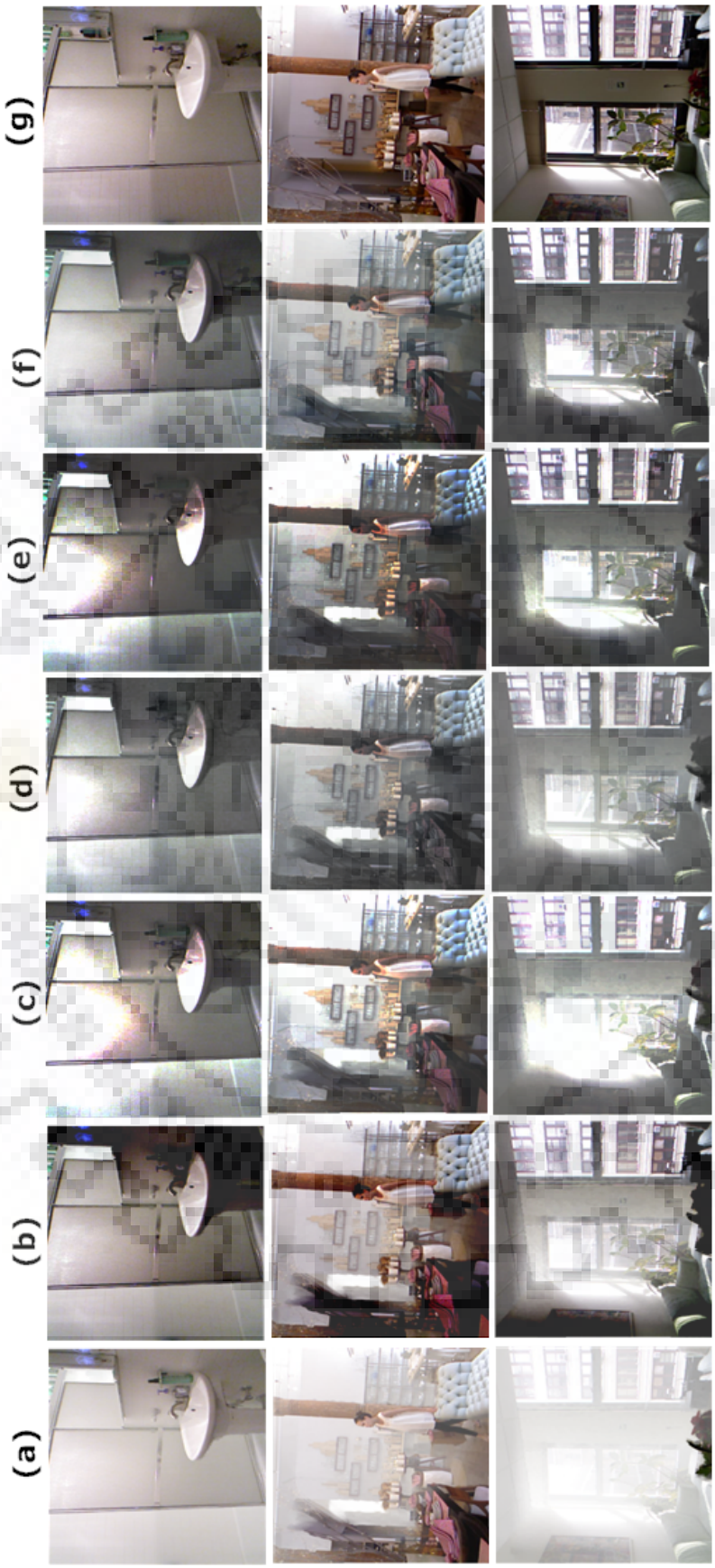

Figure 3.3: The original foggy images are given in first column. Restored images with DCP [57], FrAD [111], ADC [135], FrADP and the proposed algorithm are shown in second, third, fourth, fifth and sixth columns, respectively. The last column shows the ground truth images.

Table 3.5: Contrast gain (CG) obtained with the proposed algorithm with different fractional orders α with 30 iterations as stopping criteria.

$\alpha =$	**1.0**	**1.2**	**1.4**	**1.6**	**1.8**
Forest	0.1964	0.1971	0.1984	0.2005	**0.2013**
Wheat	0.1327	0.1333	0.1354	0.1378	**0.1380**
Tomb	0.1554	0.1558	0.1563	0.1596	**0.1606**
Ny17	0.1640	0.1648	0.1674	0.1728	**0.1735**
Swan	0.0894	0.0899	0.0915	0.0943	**0.0950**
N6	0.0819	0.0825	0.0841	**0.0876**	0.0826
Train	0.1139	0.1240	0.1232	0.1275	**0.1394**

Table 3.6: Visible edges ratio (VER) obtained with the proposed algorithm with different fractional orders α with 30 iterations as stopping criteria.

$\alpha =$	**1.0**	**1.2**	**1.4**	**1.6**	**1.8**
Forest	0.7257	**0.8431**	0.8171	0.7748	0.8085
Wheat	0.7953	0.8871	0.8571	**0.8958**	0.8915
Tomb	0.2654	0.3194	0.3457	0.3767	**0.4143**
Ny17	0.1448	0.1495	0.1541	0.1606	**0.1730**
Swan	0.5623	0.5697	0.5774	0.5799	**0.5848**
N6	0.7925	0.7980	0.7980	**0.8016**	0.7995
Train	0.2031	0.2314	0.2290	0.2694	**0.2928**

Table 3.7: Colorfulness index (CI) obtained with the proposed algorithm with different fractional orders α with 30 iterations as stopping criteria.

$\alpha =$	**1.0**	**1.2**	**1.4**	**1.6**	**1.8**
Forest	0.1284	0.1298	0.1321	0.1353	**0.1473**
Wheat	0.1918	0.1931	0.1966	0.2023	**0.2034**
Tomb	0.4265	0.4270	0.4287	0.4322	**0.4336**
Ny17	0.4110	0.4164	0.6061	0.7092	**0.9625**
Swan	0.2766	0.2834	0.3566	**0.5369**	0.3274
N6	0.1762	0.1765	0.1786	0.1808	**0.1813**
Train	0.3783	0.3820	0.4083	0.4972	**0.6042**

Table 3.8: Comparison of the results obtained with existing algorithms DCP [57], FrAD [111], ADC [135], FrADP and the proposed algorithm

Metric	Algorithm	Forest	Wheat	Tomb	Ny17	Swan	N6	Train
CG	DCP	0.0567	**0.1628**	0.0635	**0.1989**	**0.1836**	**0.5418**	**0.3223**
	FrAD	0.1086	0.0856	0.0897	0.1352	0.0754	0.0735	0.1069
	ADC	0.1059	0.0869	0.0677	0.1063	0.0569	0.0834	0.1234
	FrADP	0.1094	0.1055	0.0929	0.1733	0.0908	0.0846	0.1074
	Proposed	**0.2013**	0.1380	**0.1606**	0.1735	0.0950	0.0876	0.1394
VER	DCP	0.0152	0.0012	0.0042	0.0893	0.2857	0.0573	0.0283
	FrAD	0.2326	0.2390	0.0263	0.1609	0.5535	0.7899	0.2239
	ADC	0.0566	0.1568	0.1818	0.0399	0.3604	0.3344	0.2239
	FrADP	0.2686	0.5569	0.0570	0.1718	0.5643	0.7693	0.2756
	Proposed	**0.8431**	**0.8958**	**0.4143**	**0.1730**	**0.5848**	**0.8016**	**0.2928**
CI	DCP	**0.1529**	0.1470	0.1156	0.1029	0.0965	0.0774	0.0780
	FrAD	0.1192	0.0907	0.1352	0.4142	0.2419	0.1651	0.2945
	ADC	0.0382	0.0346	0.0507	0.0944	0.0326	0.0235	0.0493
	FrADP	0.1360	0.1967	0.2018	0.5259	0.1396	0.1728	0.3387
	Proposed	0.1473	**0.2034**	**0.4336**	**0.9625**	**0.5369**	**0.1813**	**0.6042**

is increasing with the fractional order and the best CG value is obtained at fractional-order 1.8 for images Forest, Wheat, Tomb, Ny17, Swan and Train. For N6 image, the best CG value is obtained at fractional-order 1.6. Table 3.6 and 3.7 shows the results for metrics VER and CI respectively. In tables 3.6 and 3.7, the fractional-order are giving the better values than the integer-order ($\alpha = 1$).

Table 3.8 shows the results of the proposed algorithm compared with the methods DCP, FrAD, ADC and FrADP. For Forest and Tomb images, the proposed algorithm performs best in case of metric CG. DCP performs best for the rest of the images. Also, the proposed algorithm performs better than the methods FrAD, ADC and FrADP for all of the images. For metric VER, the proposed algorithm results are better than the results of compared methods. In the case of metric CI, the proposed algorithm results are best than the compared algorithms for all of the considered images except for Forest image. The visual results for outdoor hazy images are shown in Figure 3.4 and Figure 3.5.

Table 3.9 and Table 3.10 shows the computational time in seconds of existing algorithms DCP

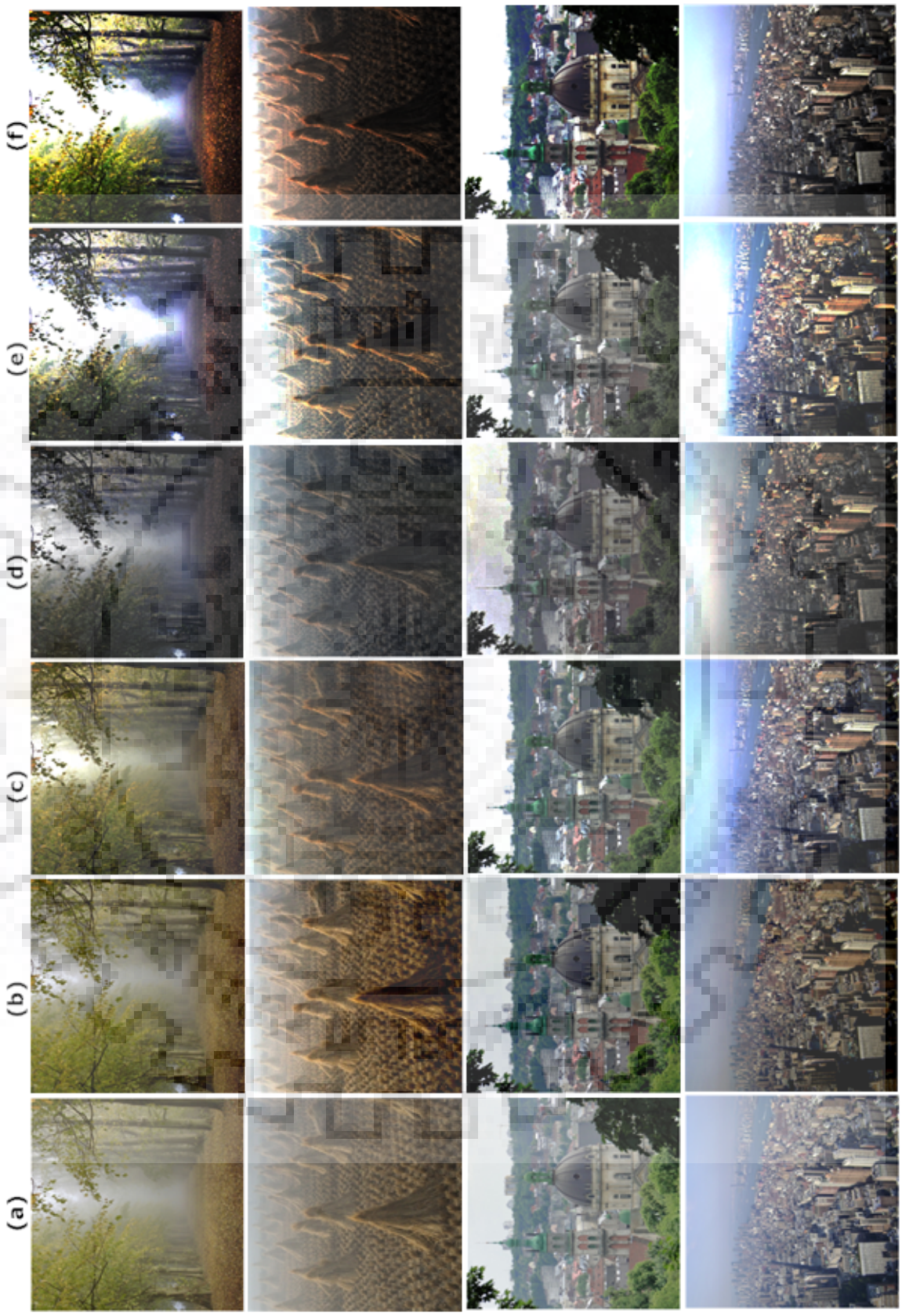

Figure 3.4: The original foggy images are given in first column. Restored images with DCP [57], FrAD [111], ADC [135], FrADP and the proposed algorithm are shown in second, third, fourth, fifth and last columns, respectively.

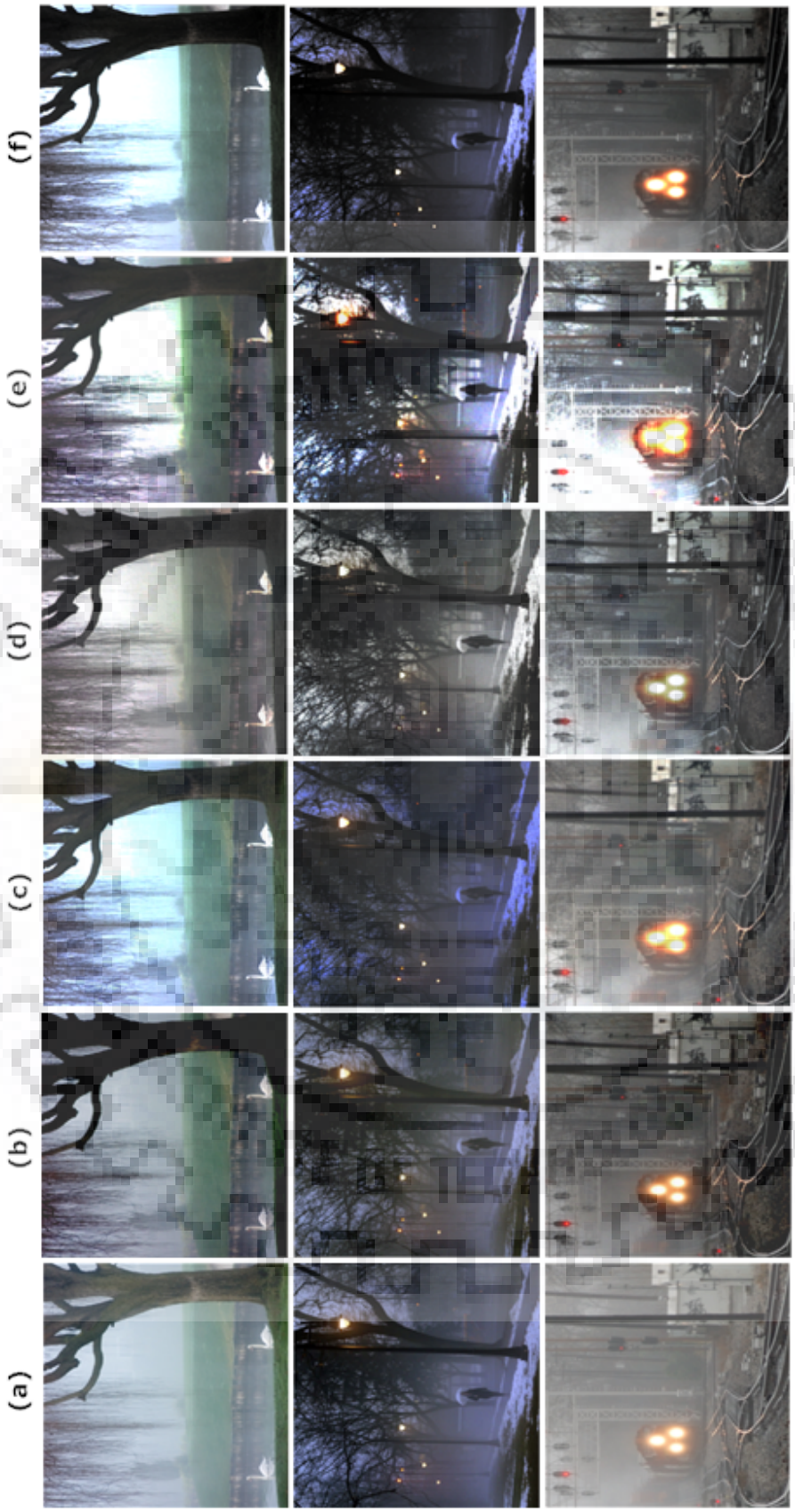

Figure 3.5: The original foggy images are given in first column. Restored images with DCP [57], FrAD [111], ADC [135], FrADP and the proposed algorithm are shown in second, third, fourth, fifth and last columns, respectively.

Table 3.9: Computational time (in seconds) comparison of the existing algorithms DCP [57], FrAD [111], ADC [135], FrADP and the proposed algorithm for synthetic haze indoor images

Image	DCP	FrAD	ADC	FrADP	Proposed
Cable	71.867973	2.332974	19.032299	9.618144	37.463209
Playtable	66.137749	2.357865	18.617090	9.784842	35.942652
Kitchen	60.204942	2.382506	17.098123	9.246703	35.749047
Door	63.389802	3.474613	19.682674	9.951501	40.638893
Basin	60.680395	2.332210	20.391771	10.767846	38.140616
Girl	61.929150	4.124971	14.175003	8.688140	39.909420
Wall	58.545615	3.341451	14.485783	8.500389	39.428176

Table 3.10: Computational time (in seconds) comparison of the existing algorithms DCP [57], FrAD [111], ADC [135], FrADP and the proposed algorithm for outdoor images

Image	DCP	FrAD	ADC	FrADP	Proposed
Forest	75.576042	1.007776	12.534592	9.223176	37.178636
Wheat	44.813626	1.012766	12.290939	8.385562	32.290020
Tomb	37.371847	0.985334	11.872720	9.641324	28.711996
Ny17	35.727895	1.010316	12.489287	9.884836	29.023324
Swan	39.964103	0.896816	16.719809	9.170654	28.097046
N6	45.174675	0.895613	16.068072	8.437273	36.457866
Train	44.261135	1.048273	13.414152	8.553134	31.833540

[57], FrAD [111], ADC [135], FrADP and the **proposed algorithm** for synthetic indoor hazy images and outdoor hazy images respectively. It can be seen from Table 3.9 and Table 3.10 that the DCP scheme takes longer computational time than all the algorithms. However, the proposed algorithm takes more time than FrAD, ADC and FrADP methods which is mainly because of the additional cross channel term and the p-Laplace norm. The computational complexity of DCP [57] is reported of order $\mathcal{O}(m^7)$ as per the source [37]. This is mainly because of soft matting otherwise without matting it is of $\mathcal{O}(m^2)$. The complexity of algorithms FrAD [111], ADC [135], FrADP and the proposed one is of order $\mathcal{O}(k \cdot m^2)$ on a $m \times m$ image with k number of iterations. We have also checked the efficiency of

Table 3.11: Comparison of quantitative results of the proposed algorithm using metric SSIM with existing methods DCP [57], FrAD [111], ADC [135] and FrADP

Image	DCP	FrAD	ADC	FrADP	Proposed
Building	0.8200	0.6716	0.8452	0.7949	**0.9153**
Lady	0.6807	0.7448	0.8132	0.7563	**0.8509**
Light	0.8496	0.7378	0.8795	0.8152	**0.9009**
Pond	0.6957	0.6015	0.7424	0.7236	**0.8012**
Street	0.6479	0.7268	0.7830	0.7651	**0.8329**

the proposed algorithm using metric structural similarity (SSIM). Considered images *Building*, *Lady*, *Light*, *Pond* and *Street* are from *SOTS* [93] dataset, where outdoor hazy images and their respective ground truth images are available. Table 3.11 shows the quantitative results for the SSIM metric. Figure 3.6 shows the visual results of these outdoor hazy images. It can be seen from the quantitative results that the SSIM value is near to 1 for the proposed scheme and better than the other methods. Also, we can see from the visual results that the image recovered using the proposed algorithm is quite good.

3.5 Conclusions

A fractional-order method with p-Laplace anisotropic diffusion for the color (RGB) images are being presented. It has been found that the factor p controls the diffusion of intensities and the direction also. The fractional-order generalization of the derivatives gives a flexibility in order to get a better-recovered image when compared to its integer-order counterpart ($\alpha = 1$). Moreover, the obtained results clearly show the importance of the additional cross channel term. Hence, the proposed algorithm is better than the existing algorithms when the input images have more than one channel.

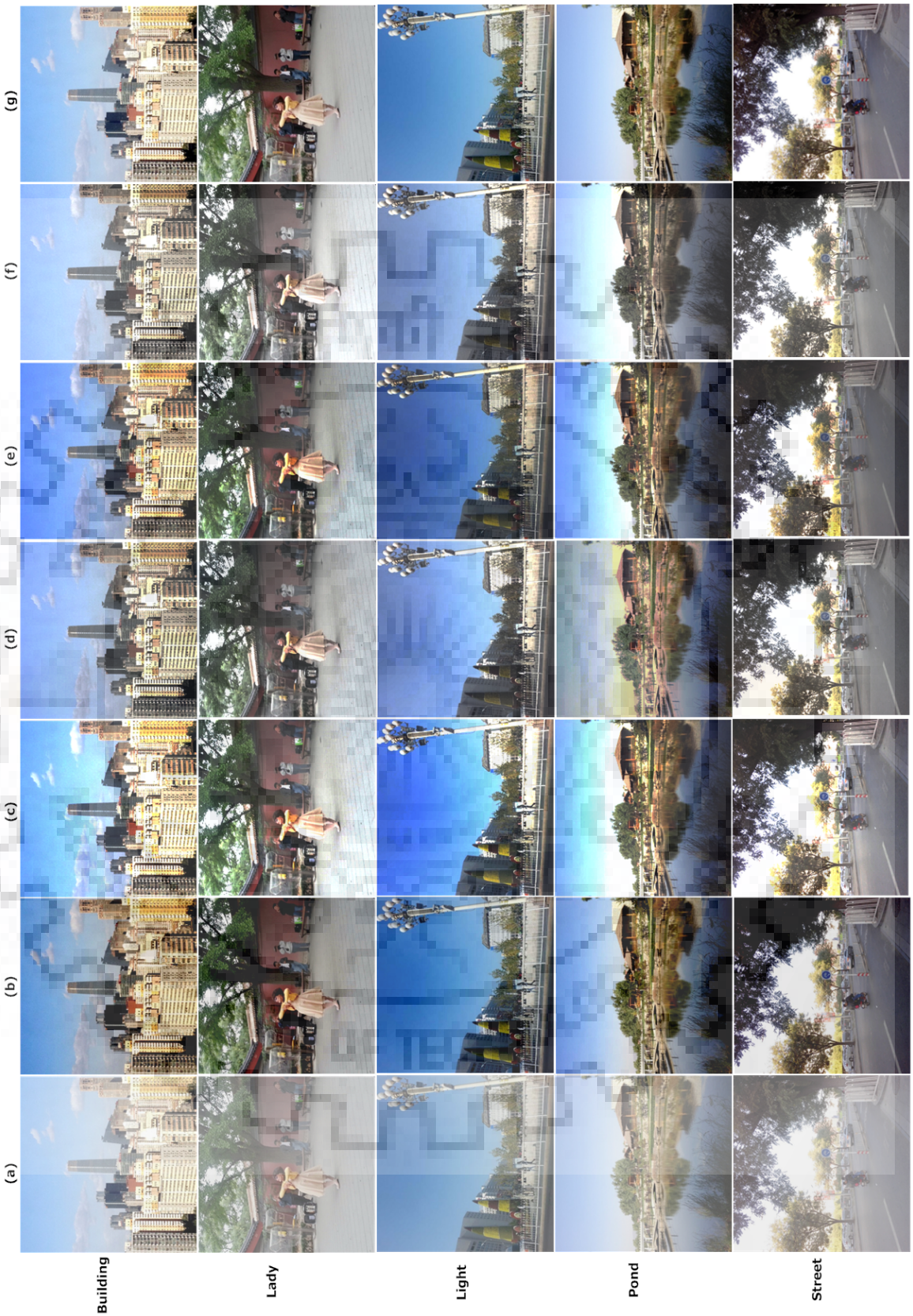

Figure 3.6: (a) Hazy images; Dehazing results of (b) DCP; (c) FrAD; (d) ADC; (e) FrADP; (f) the proposed algorithm; (g) ground truth images

Chapter 4

Image denoising in fractional quaternion wavelet transform domain

4.1 Introduction

In the previous two chapters, the image defogging based restoration algorithms were discussed. This chapter presents an image denoising algorithm using fractional quaternion wavelet transform(FrQWT). In particular, images corrupted with additive Gaussian noise are considered and FrQWT is performed via hard and semi-soft thresholds. The thresholding on the wavelet coefficients reveals the capabilities of wavelet transform in the restoration of an image degraded by the additive noise. FrQWT is simple and adaptive since the estimation of threshold parameters depends on the data of wavelet coefficients. Wavelet analysis is a popular tool to deal with image analysis for the last three decades. In image/signal analysis, Gabor functions were used extensively as filters. Gabor filters are bounded and well described using a general window function. This important aspect proposed a way to the introduction of windowed Fourier transform [52]. It opened the scope for the development of the wavelet analysis [35, 53]. Simultaneous analysis of time-frequency details and property of multiresolution analysis have proved wavelet transform as a breakthrough as a mathematical tool [21, 104]. In recent years, wavelet analysis

is coming out as one of the biggest important tools in signal analysis, pattern recognition, image processing, and other fields [108]. Wavelet transform breaks down an image into different frequency and space sub-images, and the coefficients of these sub-images are then processed. The complex discrete wavelet transform(CDWT) is a generalization of real-valued wavelet transform [83, 97]. The dual-tree complex wavelet transform or in short 'CDWT' was proposed by Kingsbury [82, 84]. The magnitudes of the transform coefficients found to be shift-invariant as real and imaginary parts of CDWT make an Hilbert-pair. The CDWT is then extended to quaternion wavelet transform (QWT) by various authors employing a quaternionic Haar kernel to overcome the low directional selectivity of CDWT [20, 164]. Soulard and Carr have proposed an effective method for texture distribution which uses coherent multi-scale analysis derived from the phase data and magnitude information of the QWT [134]. In [25], a multi-scale flow estimation algorithm was given for finding the disparity maps of between frames from a video sequence [26]. Kumar et al. [87] proposed a new algorithm for the implementation of the FrQWT using a dual-tree computation structure. The definition of their FrQWT was based on the 2D Fourier spectrum up to a single quadrant and fractional Hilbert operator.

The thresholding based methods in addition to the wavelet transforms are the most studied methods for image denoising. The thresholding technique filters the coefficients below a particular threshold and remaining coefficients are unchanged. In literature, there are several adaptive and non-adaptive thresholding based techniques [32, 39, 41, 130]. There have been two types of methods for modeling the wavelet coefficients i.e. deterministic and statistical. The deterministic approach based methods use tree structure of the wavelet coefficients, however, statistical approach based methods makes use of correlation of wavelet coefficients at different scales. The Independent Component Analysis (ICA) technique de-noises images having noise of Gaussian as well as non-Gaussian distribution. This scheme has higher computational complexity when compared to wavelet transforms [64].

In this chapter, fractional quaternion wavelet transform (FrQWT) is proposed. The fractional wavelet transform (FrWT) is defined as a generalization of the wavelet transform in the fractional Fourier domain. The rotation by an arbitrary angle in the time-frequency plane, fractional wavelet transform

(FrWT) uniquely illustrates the information of time as well as of frequency domain. However, the wavelet transform has a multiresolution property. To be specific, FrQWT is a combination of fractional domain and quaternion wavelet transform consisting of four quadratures (one real and three imaginary components). The quadratures are organized to obtain in a 2D analytic wavelet and its resulting FrQWT bases. A detailed experimental study is given for utility of the proposed approach.

4.2 Preliminaries

4.2.1 Discrete wavelet transform

Wavelet transform [108] can be defined as the decomposition of a signal with a family of real orthonormal bases. The basis elements are formed by doing shifting of scaling function $\phi(x)$ together with scaling and shifting of the wavelet functions $\psi(x)$. Mathematically, the functions $\phi_{j_0,n}(x) = 2^{\frac{j_0}{2}}\phi(2^{j_0}x - n)$ and $\psi_{j,n}(x) = 2^{\frac{j}{2}}\psi(2^j x - n)$, $j \geq j_0$, $n \in \mathbf{Z}$ form an orthonormal basis and because of the orthonormal property, we can express any signal $f(x) \in L_2(R)$ as

$$f(x) = \sum_n c_{j_0,n}\phi_{j_0,n}(x) + \sum_{j=j_0}\sum_n d_{j,n}\psi_{j,n}(x) \tag{4.1}$$

where,

$$c_{j_0,n} = \langle f, \phi_{j_0}\rangle = \sum_x f(x)\phi_{j_0,n}(x)$$

and

$$d_{j,n} = \langle f, \psi_j\rangle = \sum_x f(x)\psi_{j,n}(x)$$

Hence, the transformed signal can be seen as a combination of the translation and the scale parameters. The function $\psi(j)$ is known as mother wavelet. The mother wavelet is defined as a small wave that points out to window function and has compact support. The smaller wavelet coefficients usually represent the noise in the image as opposed to the coefficients with a larger magnitude value which contains more signal information than noise. By removing the noisy(smaller) coefficients and taking

the inverse wavelet transform may head towards a reconstruction that has a reduced amount of noise. Figure 4.1 illustrates this concept of noise removal in the DWT domain.

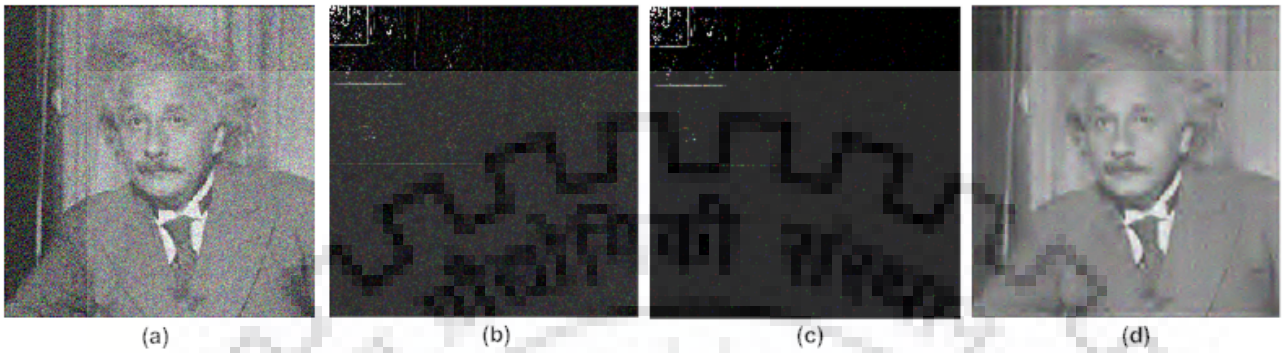

Figure 4.1: Wavelet based denoising: (a) Noisy image; (b) DWT of Noisy image; (c) Coefficients after thresholding; (d) Image after denoising

4.2.2 Complex wavelet transform(CWT)

The complex wavelet transform(CWT) was introduced to overcome few limitations of DWT [12]. One of the such drawbacks was the lack of phase information in case of real mother wavelet function. The CWT uses complex valued filtering that disintegrates the 2-D signal into real and imaginary components in the frequency domain. Basically, the real and imaginary components from the wavelet coefficients are used to calculate the magnitude information and phase angle. Like the case of Fourier representation, a mother wavelet for the CWT can be expressed as

$$\psi^c(x) = \psi^{Real}(x) + i\psi^{Imag}(x)$$

where, $\psi^{Real}(x)$ and $\psi^{Imag}(x)$ are even and odd functions, respectively, and constitute an orthogonal set of functions by using Hilbert transform.

4.2.3 Quaternion wavelet transform (QWT)

The complex wavelet transform gives information about magnitude and one phase only. Thus, it has low directional selectivity. The complex wavelet transforms are extended to quaternion wavelet transform by using a quaternionic Haar kernel. QWT is derived from the Hilbert 2-D transform theory, which comes close to shift invariance and removes the mentioned limitations of low directional selectivity of CWT. A standard DWT tensor product is used to form each quaternion wavelet, together with 1-D Hilbert transform based 1-D wavelets [24]. To be specific, the following procedure explains the implementation of QWT.

1. Calculate H_x, H_y and H_{xy} on the real tensor product wavelets as follows:

$$H_x\{\psi_h(x)\psi_h(y)\} = \psi_g(x)\psi_h(y) \tag{4.2}$$

$$H_y\{\psi_h(x)\psi_h(y)\} = \psi_h(x)\psi_g(y) \tag{4.3}$$

$$H_y\mathcal{H}_x\{\psi_h(x)\psi_h(y)\} = \psi_g(x)\psi_g(y) \tag{4.4}$$

   where, H_x and H_y denotes the 1-D Hilbert transform operators along the x and y coordinates, respectively.

2. The above four wavelet components are organized in order to get a quaternion wavelet as follows

$$\psi^q(x,y) = \psi_h(x)\psi_h(y) - i\psi_g(x)\psi_h(y) - j\psi_h(x)\psi_g(y) + k\psi_g(x)\psi_g(y) \tag{4.5}$$

In general, the original image is assumed to be degraded by the presence of white Gaussian noise having zero mean. The linearity of the QWT, the additive model of the noise remains invariant in QWT domain also [75]. hence, the noise can be filtered out for achieving the denoising, i.e.,

$$w_{k,l}(x,y) = f_{k,l}(x,y) + \eta_{k,l}(x,y)$$

where, $w_{k,l}(x,y)$ represents noisy QWT coefficients, while $f_{k,l}(x,y)$ represents noise-free coefficients in the transform domain. The term $\eta_{k,l}(x,y)$ represents the noise components of scale k and orientation l in the noisy image.

4.3 FrQWT-based denoising approach

4.3.1 Definition and construction

FrQWT is defined in a similar fashion as QWT [87]. Here, we make use of fractional Hilbert operator in place of the classical Hilbert operator to generalize the QWT in the FrQWT. The fractional quaternion wavelet is defined as

$$\psi^H(x,y) = f_H(x,y) + if_{H_1}(x,y) + jf_{H_2}(x,y) + kf_{H_3}(x,y) \tag{4.6}$$

where, the fractional wavelet components $f_{H_1}(x,y)$ and $f_{H_2}(x,y)$ are given as

$$f_H(x,y) = \psi_h(x)\phi_h(y)$$

$$f_{H_1}(x,y) = \mathcal{H}_{x,\tau_1}\{\psi_h(x)\phi_h(y)\} = \cos(\pi\tau_1)\psi_h(x)\phi_h(y) - \sin(\pi\tau_1)\psi_g(x)\phi_h(y)$$

$$f_{H_2}(x,y) = \mathcal{H}_{y,\tau_2}\{\psi_h(x)\phi_h(y)\} = \cos(\pi\tau_2)\psi_h(x)\phi_h(y) - \sin(\pi\tau_2)\psi_h(x)\phi_g(y)$$

similarly, the texture detail part $f_{H_3}(x,y)$ is given as

$$f_{H_3}(x,y) = \mathcal{H}_{y,\tau_2}\mathcal{H}_{x,\tau_1}\{\psi_h(x)\phi_h(y)\}$$

where, one-dimensional dual tree CDWT is used to compute each wavelet component. In order to derive a fractional quaternion wavelet basis along a horizontal sub-bannd, the four wavelet components can be utilized as given in the theory of the quaternion algebra. Similarly, the expressions for the other two sub-bands, i.e. vertical sub-band $\phi_h(x)\psi_h(y)$ and diagonal sub-band $\psi_h(x)\psi_h(y)$ can also be obtained using tensor product.

A 2D implementation of dual-tree filter bank is used separately for computing the FrQWT coefficients. The details about the filter bank implementation can be found in [87]. Finally, the 2D fractional quaternionic analytic signal of a real-valued signal $f(x,y)$ is given as

$$f_A^{\alpha}(x,y) = f_H(x,y) + if_{H_1}(x,y) + jf_{H_2}(x,y) + kf_{H_3}(x,y), \tag{4.7}$$

where, the functions $f_{H_1}(x,y)$, $f_{H_2}(x,y)$ and $f_{H_3}(x,y)$ are the wavelet tensor product components for a horizontal sub-bands.

4.3.2 Image denoising

The FrQWT provides three phases, two of which gives local displacement while the third contains the texture information. Here, we are using thresholding on the FrQWT coefficients to remove the noise. In addition to this, we are also using phase regularization on thresholded coefficients to further denoise the image.

4.3.2.1 Thresholding

In general, the process of thresholding can be considered as a simple non-linear filtering operates at one wavelet coefficient at a time [71]. Basically, thresholding is performed by comparing a coefficient against a threshold value. In particular, it works like a high-pass filtering, i.e., if the coefficient is smaller than the threshold, it is set to zero; otherwise kept as it is or modified. This replacement of the small noisy coefficients by zero and inverse wavelet transform on the resulting coefficients may give a reconstruction with the important signal properties with reduced noise. We use the two types of thresholding mechanisms: hard and semi-soft thresholding. The hard thresholding can be achieved as

$$\begin{cases} w, & |w| > \lambda; \\ 0, & \text{Otherwise.} \end{cases}$$

The semi-soft thresholding is performed based on the following criteria:

$$D(w, \lambda) = [sgn(w)].\max\{0, |w| - \lambda\}$$

A hard threshold can be seen as an eliminating or no-change strategy. It is more intuitively appealing. On the other hand, semi-soft thresholding [39] use to shorten the coefficients by an amount of the threshold, those are having absolute values above the threshold λ. In general, hard thresholding seems like a filtering and more appealing naturally. However, the dependency on the threshold makes it a not preferable choice. For example, a small threshold may generate a result close to the input value, but the noise may still be present in the signal/image. The choice of a large threshold results in the loss of texture details from the image. Figure 4.2 illustrates a flowchart of the proposed denoising scheme.

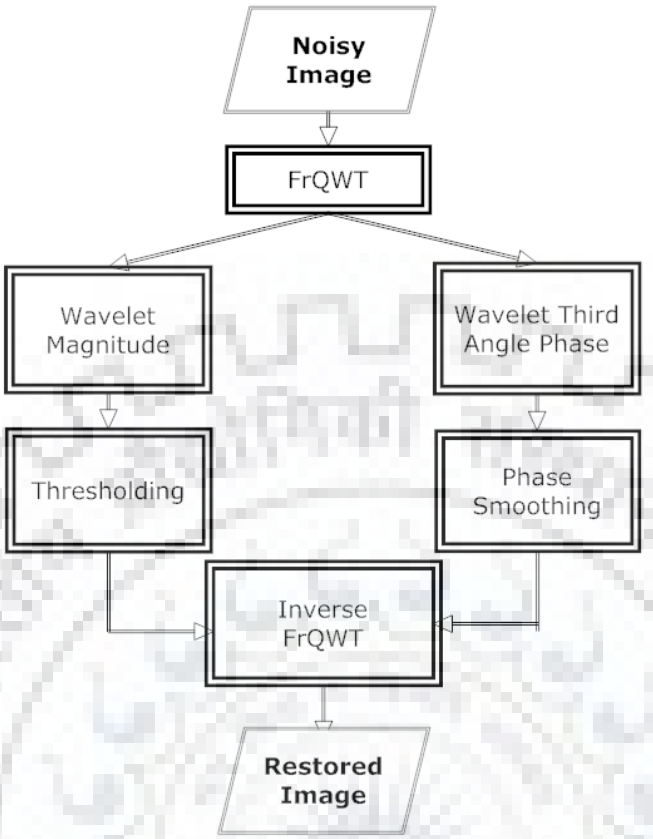

Figure 4.2: Flowchart for denoising using FrQWT

4.3.2.2 Phase regularization

The thresholding use to be done only on the magnitude of the FrQWT coefficients. We need to perform some regularization on the phases of the transform to utilize the information encoded with them. We know that the three-phase angles obtained with FrQWT are separable. The shift information is encoded with the first two phases, while the third one conceals the textural details. The first two phases found to be shift-invariant in the QWT domain [20]. This shift theorem also holds for FrQWT domain, especially for a local QFT analysis. Consider a small shift $\tau = (\tau_1, \tau_2)$ which translate a 2-D signal $I(x, y)$ to $I(x - \tau_1, y - \tau_2)$. In the transformed domain, the following variations occur in transformed signals.

$$(\theta_1(\mu), \theta_2(\mu), \theta_3(\mu)) \rightarrow (\theta_1(\mu) - 2\pi\mu\tau_1, \theta_2(\mu) - 2\pi\mu\tau_2, \theta_3(\mu))$$

where, θ_i for $i = 1,\ 2,\ 3$ represents the three-phase angels of the quaternion transform in the wavelet domain. It can be noticed down that, there is no change in the third phase angle, while the first two phases follow the shift-invariant property. Therefore, we need to implement a regularization process on the third phase angle to achieve the smoothness. The choice of such a regularizer becomes a typical first-order regularizer $R(\theta_3) = C\theta_3$, where C is taken as a finite matrix. One of the obvious choice of such a matrix is the median filter [75]. This particular choice of regularizer, enforce spatial smoothness in the transformed coefficients, which is required after the thresholding based removal of the noise from the images. Hence, the transformed signal can be represented in the polar form with the following expression:

$$w_{k,l}(x,y) = (|w_{k,l}(x,y)|_T)e^{i\theta_1}e^{j\theta_2}e^{kC\theta_3}$$

Here, the regularization of the third phase angle together with a thresholding on the magnitude of fractional quaternion wavelet coefficients result into a perfect technique for image denoising. Moreover, by using median filter as the regularization matrix C, smoothness of the resulting image is guaranteed.

4.4 Experiment results

A detailed experimental analysis has been carried out with eight different images. All the images were taken of the same size and Gaussian noise with zero mean and variance of amount 0.006 and 0.01 were added to the images. We have applied a single threshold value for all the images for a particular variance. In that context, the hard threshold value of 0.03 and 0.0001 is used for variances 0.006 and 0.01 respectively. The set of original images and the noisy images after adding the Gaussian noise are illustrated in figure 4.3 and 4.4. The images are chosen in such a way that they are different in terms of feature/texture details. The results obtained with the proposed (FrQWT based) approach were compared with DWT(having Daubechies mother wavelet function), CDWT and QWT. The thresholding of frequency coefficients was performed based on the semi-soft and hard thresholds strategy. PSNR and MSE are the two measures that are used to carry out comparative analysis. The results in the

Image	**Noisy**	**DWT**	**CWT**	**QWT**	**FrQWT**
Cameraman	22.3843	26.7851	26.6109	28.1256	29.7794
		25.9638	26.7090	28.1850	29.7973
Einstein	22.2130	27.4505	27.7502	28.3116	28.7984
		26.9309	27.8547	28.3586	28.8033
House	22.2874	24.7965	26.9070	27.2739	29.1260
		23.8104	26.7021	27.2512	29.1213
Campus	22.3456	25.6071	26.4631	27.5628	28.2301
		24.8875	26.5900	27.3458	28.2575
MainBuilding	22.3144	25.3257	26.5237	25.6330	27.8118
		24.9469	26.5612	25.9501	27.6499
Bridge	22.3679	25.2909	27.1314	26.4175	29.9000
		24.3904	27.1464	26.6740	29.8958
Tower	22.1821	26.8065	27.6546	27.8078	28.3646
		26.1604	27.9374	28.1626	28.3725
GoldenGate	22.2581	24.5673	26.2799	26.7928	29.0596
		23.9423	26.7669	26.8157	29.0206

Table 4.1: PSNR values after denoising with different wavelets and in case of the proposed algorithm (last column). The noisy image are created by adding Gaussian noise with variance 0.006. The two rows for each image shown the results against hard and semi-soft thresholding.

case of low variance ($\sigma^2 = 0.006$) have been listed in Table 4.1. The first column describes the image, while the second column gives the PSNR value between the original (ground truth) and their respective noisy images. Denoising aims to increase this PSNR between the restored and original images. The third, fourth and fifth columns represent the PSNR values between restored and original images. In the case of the cameraman image, the performance of FrQWT was found better than other variants of wavelet. The QWT stood second and then DWT and CDWT. However, in the rest of the images, the performance in the increasing order can be seen as DWT, CDWT, QWT, and FrQWT. Hence the proposed approach performed better than other schemes. In the case of Bridge and Golden-gate, FrQWT performance is quite better than the rest. In general, a gain of PSNR about 7 units was noticed when compared to the noisy image. The other observation can be noticed that in most of the images, semi-soft thresholding done a better work when compared to the hard thresholding. In the second set of images with the noise of variance 0.01, the performance of FrQWT is found better than DWT, CDWT, and QWT in the case of all the images. The results for the same have been listed in Table 4.2. Figure 4.5 illustrated the restored images for this set of experiments. Again, the semi-soft scheme of thresholding performed marginally better than the hard thresholding. The PSNR gain in

Image	Noisy	DWT	CWT	QWT	FrQWT
Cameraman	20.2083	26.5807	24.6276	26.4996	29.9626
		27.0448	24.9378	26.5828	29.9379
Einstein	20.0239	27.5598	25.8454	26.7576	29.0172
		27.9640	25.6505	26.6252	29.0055
House	20.0822	24.7817	25.1730	25.9344	29.3464
		25.3782	25.0366	26.0179	29.3203
Campus	20.4255	26.4372	23.7162	26.3957	28.5502
		26.8713	24.5872	26.4811	28.5026
MainBuilding	20.2552	25.4101	23.8689	24.7237	27.8738
		26.3103	24.3575	24.3521	27.8403
Bridge	20.2509	25.2627	24.8958	25.7182	30.0223
		26.0559	25.3037	25.4567	30.0299
Tower	20.0127	27.3957	26.2044	26.3615	28.5953
		27.3530	25.9454	26.4315	28.5740
GoldenGate	20.0323	24.7322	25.0534	25.4248	33.6949
		25.1707	24.6031	25.3487	33.6891

Table 4.2: PSNR values after denoising with different wavelets and in case of the proposed algorithm (last column). The noisy image are created by adding Gaussian noise with variance 0.01. The two rows for each image show the results against hard and semi-soft thresholding.

this set of experiments was found of the order of approximately 8.0 to 13.0, and we obtained almost the same or better PSNR as it was found in the case of earlier experiment. In an explicit comparison with QWT [164], gains of 2-4 decibels in PSNR are achieved which can be considered as a good sign of improvement. In figure 4.6, the different noises are used such as salt and pepper noise, additive white Gaussian noise of variance 0.01 and speckle noise of variance 0.04 respectively. Hence, the addition of an increased amount of the noise does not degrade the performance of FrQWT based denoising.

4.5 Conclusions

In this chapter, removal of noise from the images has been done in the fractional quaternion wavelet transform domain. From the experimental results, it has been observed that better denoising results are obtained in the FrQWT domain when compared to earlier existing techniques. Further, it has been found that the choice of hard or semi-soft thresholding depends on the image. In a few of the images, the semi-soft threshold performs marginally better than a hard threshold. However, in a few cases, it was found that the choice of hard threshold is better. In the next chapter, we make use of anisotropic diffusion and wavelet transform together for image denoising.

Figure 4.3: Ground truth images used in experimental study

Figure 4.4: Noisy images used in experimental study

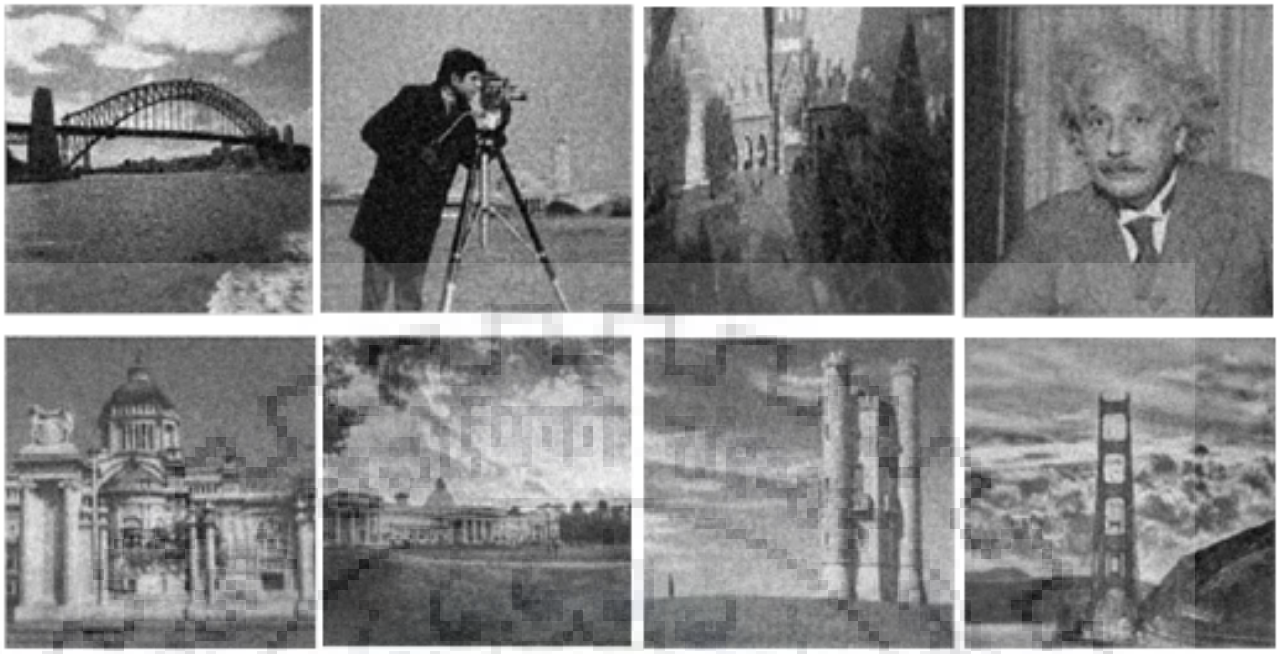

Figure 4.5: Recovered images after performing FrQWT on noisy images

Figure 4.6: Recovered images after performing FrQWT on images with different types of noise and variance

Chapter 5

Generalized order anisotropic diffusion model for image denoising using wavelet based subspace decomposition

5.1 Introduction

In this chapter, an improved context-adaptive fractional order anisotropic diffusion (FOAD) model for image denoising is presented. The proposed FOAD model includes an improved version of Perona-Malik diffusion coefficient. A fractional order derivative is applied to reduce the staircasing effect and to preserve the fine characteristics, whereas, the improved diffusion coefficient protects edges and corners from getting over-smoothed. Discrete wavelet transform is used to decompose the image into low frequency parts, those are further enhanced using diffusion process.

The existing denoising algorithms are lacking in absolute perseverance of the sharp details of the image. However, partial differential equations (PDEs) based methods are capable to preserve fine details in the smoothing process up to some extent. Witkin introduced the scale space representation [156], based on which Perona-Malik [117] and Rudin-Osher-Fatemi [123] introduced nonlinear PDEs in the

image restoration process. Perona-Malik [117] introduced the non-linear operator in order to remove the noise and to preserve the edges. However, in case of noisy signal with white noise, the noise inserts the large oscillations of the gradient of the image. There is no stopping criteria of diffusitivity in the case of nonlinear PDEs based methods. Weickert et al. [151] introduced an operator based on the local variations of the gradient orientation. Considering the viewpoint of robust statistics, Black et al. [18] suggested another diffusivity function using Tukeys Biweight concept. This diffusion process could preserve sharp boundaries and better continuity of edges.

In literature, subspace decomposition based techniques are also used for image enhancement [175], since there is different importance for the low frequency and high frequency components of an image. These techniques also accelerate the solution of PDEs on parallel machines. Pu et al. [119] has shown that methods based on fractional differential preserves low-frequency contour features in smooth regions. They also proved that fractional differentiation retains high-frequency marginal features in regions that particularly have large gray-level variabilities, and can also enhance the texture details in those regions which do not have significant gray-level variabilities.

In recent times, wavelet transforms in frequency domain has acquired generous attention from many researchers. It provides multi scale signal decomposition with multi-resolution analysis which gives the entire idea of details occurring at different locations [104]. Nowadays, subspace decomposition methods [175] plays a significant role in the large scale computations. In subspace decomposition, the different frequency parts of the initial noisy image are denoised independently followed by their fusion. In this chapter, an algorithm is designed in which fractional order anisotropic diffusion is applied in various sub-bands of the image in wavelet transform domain. The implementation of diffusion filters is directionally sensitive and preserves sharp details up to large extent when compared to classical implementation. Such an implementation is carried out by designing four filters, one for each wavelet sub-band of the image.

5.2 Fractional order anisotropic diffusion

In general, there is no unified formula to illustrate fractional derivatives. Many mathematicians have figured out the problem at hand from different point of view and came along various definitions of fractional derivatives. Out of all the definitions, three definitions, namely Grunwald-Letnikov, Riemann-Liouville and Caputo are quite popular. Since Grunwald-Letnikov definition uses only one coefficient and is less complex, it made its way easily in this work.

$$a^{\alpha}_{D_b} f(t) = \lim_{h \to 0} h^{-\alpha} \sum_{i=0}^{\frac{b-a}{h}} (-1)^i f(t - ih) \binom{\alpha}{i} \tag{5.1}$$

where, α denotes the fractional order in the interval $[1, 2)$. The integral part of $\frac{b-a}{h}$ is $\left\lceil \frac{b-a}{h} \right\rceil$ and $\binom{\alpha}{i} = \frac{\alpha!}{i!(\alpha-i)!}$ is the binomial coefficient.

5.3 Proposed model

In imaging, the simplest model for degradation of an image I due to the additive noise η can be written in the following form

$$I_0 = I + \eta \tag{5.2}$$

where, $I_0 : \Omega \to \mathrm{R}$ is a noisy image which needs to be denoised. The noise η in the above equation is additive white Gaussian noise (AWGN). The domain of the image $\Omega \subseteq \mathrm{R}^2$ is bounded which is usually a rectangle in image denoising.

5.3.1 Wavelet based subspace decomposition

The noisy image I_0 is firstly decomposed using a 2-D discrete wavelet transform which gives an approximation part A and three detail components H, V and D. Then, three different images are reconstructed in the following way

$$I_H = A \oplus H; \tag{5.3}$$

$$I_V = A \oplus V; \tag{5.4}$$

Figure 5.1: The first row shows the image decomposition using wavelet transform into A, H, V, D parts; The second row shows the reconstructed detail parts I_H, I_V and I_D; The third row shows the edge details of images I_H, I_V and I_D using Canny edge detector.

$$I_D = A \oplus D; \tag{5.5}$$

where, $\oplus$ represents the inverse DWT operated on the two parts together while the other two parts are totally smooth detail parts, i.e. I_H is obtained using the inverse DWT on A, H and the plain V and D parts. Figure 5.1 illustrates this on the test image *Lena*. Here, the main idea is to diffuse these three parts in different direction for a better edge prevention.

5.3.2 Direction adaptive filtering using FrAD

To restore the image $I(x, y)$ from the degraded version $I_0(x, y)$, one needs to solve the following PDE

$$\frac{\partial I}{\partial t} = div(g(|\nabla I|^2)\nabla I) \tag{5.6}$$

with conditions $I(x, y, 0) = I_0(x, y) \ \ \forall\ x, y \in \Omega$ and natural boundary conditions. This PDE can be approximated using a numerical scheme based on the finite differences as given in [117]. However, we use the following fractional order diffusion PDE

$$\frac{\partial I}{\partial t} = div\left(g(|\nabla I_\sigma^\alpha|^2)\nabla I\right) \tag{5.7}$$

with conditions $I(x, y, 0) = I_0(x, y) \ \ \forall\ x, y \in \Omega$ and natural boundary conditions. We can approximate the above PDE by using the following grid based numerical scheme:

$$\begin{aligned} {I_k}^{t+1} = {I_k}^t + \lambda(c_N \cdot \bigtriangledown_N^\alpha I + c_S \cdot \bigtriangledown_S^\alpha I + c_W \cdot \bigtriangledown_W^\alpha I + c_E \cdot \bigtriangledown_E^\alpha I + \\ c_{NE} \cdot \bigtriangledown_{NE}^\alpha I + c_{NW} \cdot \bigtriangledown_{NW}^\alpha I + c_{SE} \cdot \bigtriangledown_{SE}^\alpha I + c_{SW} \cdot \bigtriangledown_{SW}^\alpha I) \end{aligned} \tag{5.8}$$

where, the conduction coefficient is defined as

$$c_i = \frac{1}{1 + (\frac{\nabla_i{}^\alpha I}{\hat{\kappa}})^2}$$

Here, i denotes the directions viz. $N, S, E, W, NE, NW, SE, SW$ in which the fractional order anisotropic diffusion is being applied. The diffusion coefficients in the above equation (5.8) depend on the direction i with following rules:

- On the approximation part A, the diffusion is applied in all the directions.
- For the updated horizontal part I_H, the diffusion is applied in the perpendicular direction so the diffusion coefficients will be c_N and c_S only and others will be zero.
- For the updated vertical part I_V, the diffusion is applied perpendicularly and the diffusion coefficients will be c_E and c_W only and others will be vanished.

- For the updated vertical part I_D, the diffusion is applied in the diagonal directions viz. NE, NW, SE, SW. Thus, the diffusion coefficients in equation (5.8) will be $c_{NE}, c_{NW}, c_{SE}, c_{SW}$.

Also, $\hat{\kappa}$ in the diffusion coefficient is the threshold parameter that controls the amount of conduction. It is defined in the following way:

- For the first two iterations of the numerical scheme (5.8), $\hat{\kappa}$ is normalized as $n \cdot \kappa$ where $n = \left(\frac{\alpha+\frac{\alpha*(\alpha-1)}{2}+1}{2}\right)^{10}$ and κ is the parameter from the Perona-Malik scheme. After two iterations, this parameter will behave like in Perona-Malik method.

Generally, the image gradient varies near the edges which corresponds to the high frequency components. The low frequency part is the weak textured region where the gradient magnitude is low. The edges and the higher gradient region can be well preserved by the fractional differential operators. Using G-L definition, the backward difference scheme of fractional order partial derivatives of order α on the left side of pixel (x, y) can be expressed as:

$$\nabla_x^\alpha I(x,y) = I(x,y) + (-\alpha)I(x-1,y) + (-\alpha)\frac{-\alpha+1}{2}I(x-2,y) + \cdots + \frac{\Gamma(-\alpha+1)}{i!\,\Gamma(-\alpha+i+1)}I(x-i,y) \quad (5.9)$$

and

$$\nabla_y^\alpha I(x,y) = I(x,y) + (-\alpha)I(x,y-1) + (-\alpha)\frac{-\alpha+1}{2}I(x,y-2) + \cdots + \frac{\Gamma(-\alpha+1)}{i!\,\Gamma(-\alpha+i+1)}I(x,y-i) \quad (5.10)$$

where, Γ denotes the Gamma function. The symbol $\bigtriangledown$ in equation (5.8) specifies the nearest neighbor differences and can be calculated by convolving the masks M, M_H, M_V, M_D on the respective components $k = A, I_H, I_V, I_D$.

$$\mathrm{M} = \begin{array}{|c|c|c|c|c|} \hline \frac{\alpha^2-\alpha}{2} & 0 & \frac{\alpha^2-\alpha}{2} & 0 & \frac{\alpha^2-\alpha}{2} \\ \hline 0 & -\alpha & -\alpha & -\alpha & 0 \\ \hline \frac{\alpha^2-\alpha}{2} & -\alpha & 8 & -\alpha & \frac{\alpha^2-\alpha}{2} \\ \hline 0 & -\alpha & -\alpha & -\alpha & 0 \\ \hline \frac{\alpha^2-\alpha}{2} & 0 & \frac{\alpha^2-\alpha}{2} & 0 & \frac{\alpha^2-\alpha}{2} \\ \hline \end{array} \qquad M_H = \begin{array}{|c|c|c|c|c|} \hline 0 & 0 & \frac{\alpha^2-\alpha}{2} & 0 & 0 \\ \hline 0 & 0 & -\alpha & 0 & 0 \\ \hline 0 & 0 & 2 & 0 & 0 \\ \hline 0 & 0 & -\alpha & 0 & 0 \\ \hline 0 & 0 & \frac{\alpha^2-\alpha}{2} & 0 & 0 \\ \hline \end{array}$$

$$M_V = \begin{array}{|c|c|c|c|c|} \hline 0 & 0 & 0 & 0 & 0 \\ \hline 0 & 0 & 0 & 0 & 0 \\ \hline \frac{\alpha^2-\alpha}{2} & -\alpha & 2 & -\alpha & \frac{\alpha^2-\alpha}{2} \\ \hline 0 & 0 & 0 & 0 & 0 \\ \hline 0 & 0 & 0 & 0 & 0 \\ \hline \end{array} \quad M_D = \begin{array}{|c|c|c|c|c|} \hline \frac{\alpha^2-\alpha}{2} & 0 & 0 & 0 & \frac{\alpha^2-\alpha}{2} \\ \hline 0 & -\alpha & 0 & -\alpha & 0 \\ \hline 0 & 0 & 4 & 0 & 0 \\ \hline 0 & -\alpha & 0 & -\alpha & 0 \\ \hline \frac{\alpha^2-\alpha}{2} & 0 & 0 & 0 & \frac{\alpha^2-\alpha}{2} \\ \hline \end{array}$$

Finally, we update the denoised image using the Perona-Malik based numerical scheme (5.8) and the final recovered image is computed as the weighted subspace fusion of the above filtered images.

5.3.3 Numerical scheme

To refine the image, we have applied the fractional order anisotropic diffusion in the perpendicular direction to the edges. Thus, in case of the horizontal details, the diffusion is applied in the vertical direction using the filter M_H. In case of vertical details, the diffusion is performed in horizontal direction by using the filter M_V. Hence, the iterative scheme used to solve the PDE (5.6) is given as

$$\begin{aligned} I(x,y)_k^{(t+1)} = I(x,y)_k(t) + \lambda(cN.DN + cS.DS + cW.DW + cE.DE \\ +cNE.DNE + cNW.DNW + cSE.DSE + cSW.DSW) \end{aligned} \tag{5.11}$$

The modified diffusion coefficient is defined in the following way

$$cZ(x) = \frac{1}{1+(\frac{x}{k})^2};\ Z = N, S, W, E, NE, NW, SE, SW$$

Now, to calculate the gradient matrices in horizontal, vertical and diagonal directions, the convolution masks used in the respective directions are given by M_H, M_V and M_D respectively. The algorithm 3 gives a brief overview of the overall implementation.

In 3, the weighted average is taken by considering weights $w_1 = 1$, $w_2 = 0.2$, $w_3 = 0.2$ and $w_4 = 0.6$. Here, weights can take any value but increasing values of the weights leads to enormous brightness or darkness in the output image. Thus for image naturalization, the above values of weights are considered in order to evade the excessive contrast of the recovered image.

Algorithm 3 Computational Algorithm for image denoising

Step 1: Input I_0 as the initial noisy image, λ, *niter*.
Step 2: Perform DWT on the initial image I_0 giving the approximation part A and the detail parts as H, V and D.
Step 3: Update the detail components as $I_H = A \oplus H$; $I_V = A \oplus V$; $I_D = A \oplus D$
Step 4: Apply FOAD filters M on the approximation part A producing the updated image J.
Step 5: Apply FOAD filters M_H, M_V and M_D on the updated detail parts obtained in step 3 respectively giving the updated images J_H, J_V and J_D.
Step 6: Perform the weighted subspace fusion of the images J, J_H, J_V and J_D as

$$I = \frac{J + (0.2)J_H + (0.2)J_V + (0.6)J_D}{2}$$

5.4 Experimental results

In order to test the effectiveness of the proposed algorithm, we have done the evaluation on the five test images of size 512×512 pixels namely Lena, Pentagon, Wallpaint, Boat and Pepper. The considered images have the additive white Gaussian noise with zero mean and varying noise variances in range $0.010 - 0.035$ with an interval of 0.005. The performance of the proposed algorithm is compared with the existing approaches like Gaussian smoothing, Bilateral filtering [144] and the Perona-Malik method [117]. The metrics used to test the efficiency of the proposed algorithm are peak signal to noise ratio (PSNR), the mean square error (MSE) and structural similarity (SSIM) as defined in Chapter 1.
To show the accuracy of the proposed algorithm in case of edge or the details perseverance, images having horizontal and vertical edges are considered. All the existing algorithms and the proposed algorithm are applied on these images and measured the qualitative as well as the quantitative results. Table 5.1 shows the quantitative results for the metrics PSNR, MSE and SSIM. The proposed algorithm gives the best PSNR gain viz. 33 decibels for the horizontal and vertical details images. The proposed algorithm gives least MSE values than the compared algorithms which shows the better image restoration. Also, the SSIM values are 0.85 for the horizontal and vertical details. The visual results for these detailed images are shown in Figure 5.2.

Table 5.2, Table 5.3 and Table 5.4 show the denoising results on these noisy images with different

Table 5.1: Comparison of the average PSNR, MSE & SSIM results obtained with algorithm Gaussian smoothing, Bilateral filtering [144], Perona-Malik [117] and the proposed algorithm with variance 0.001

Image	Sigma	Noisy	GS	BF	PM	Proposed
Horizontal	PSNR	20.3088	24.0754	28.1274	31.2400	33.7655
	MSE	52.7529	48.9240	42.9274	35.7823	27.4966
	SSIM	0.3869	0.4050	0.5672	0.6947	0.8595
Vertical	PSNR	20.2818	24.0440	28.0974	31.1997	33.6415
	MSE	53.2873	49.6710	43.2874	36.3621	28.0138
	SSIM	0.3836	0.3974	0.5562	0.6920	0.8563

variance for the metrics PSNR, MSE & SSIM respectively. In Table-5.2, the first rows of each considered image shows the PSNR value in unit decibel for the noisy image. Similarly, the second and third rows for each image shows the PSNR values using the methods Gaussian smoothing and Bilateral filtering respectively. The fourth row shows the denoising results of the anisotropic diffusion based on Perona-Malik method.

The last rows for each image shows the PSNR results with the proposed algorithm. For the Lena image, the average PSNR value for noisy image with variance 0.010 is 17.071. The average PSNR value for the methods Gaussian Smoothing, Bilateral Filtering [144] and Perona-Malik method [117] are 20.9047, 19.1912 and 27.105 respectively. However, the average PSNR value of the proposed algorithm is 28.5149. The average PSNR value of the proposed algorithm is greater for all the images than the three existing algorithms. For Boat image, the average PSNR gain for the noisy image is 17.124. The average PSNR value for methods Gaussian Smoothing, Bilateral Filtering and Perona-Malik are 20.9604, 19.8756 and 25.5791 respectively. The average PSNR gain for the proposed algorithm is 28.2173. Thus, the proposed algorithm gives an overall gain of 3 decibels than the Perona-Malik method for the Boat image.

The PSNR values for each image with the varying variances are shown in Table 5.2. In particular, for the variance 0.010, the proposed algorithm gives an increase of nearly 10 decibels for the recovered image. However, the gain in the PSNR value for the other three methods is maximum of 7 decibels.

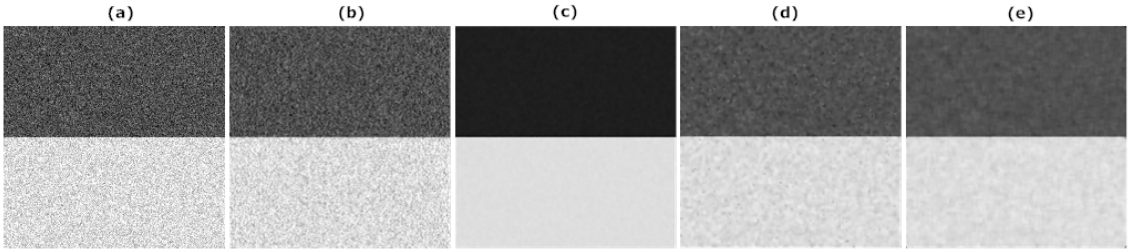

(a) Horizontal details

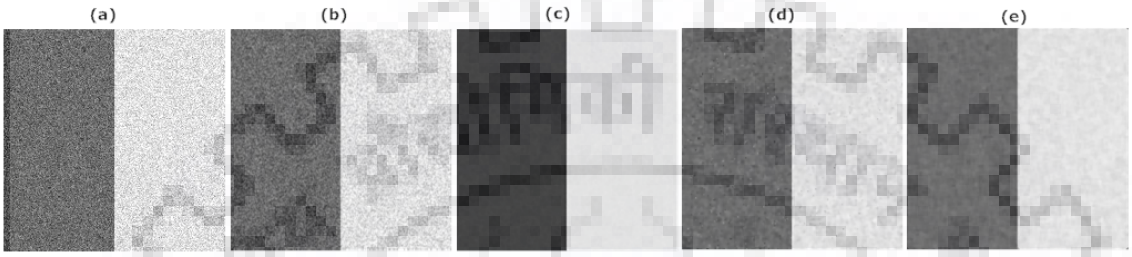

(b) Vertical details

Figure 5.2: Visual denoising results of images with horizontal and vertical details (a) Noisy image; (b) Gaussian smoothing; (c) Bilateral filtering [144]; (d) Perona-Malik [117]; (e) the proposed algorithm

When the image is having the higher variance 0.035, the gain in the PSNR value is 13 decibels for the proposed algorithm which is greater than the PSNR gain of all the methods Gaussian Smoothing, Bilateral Filtering and Perona-Malik method. The proposed algorithm performs better than all these three algorithms with an average PSNR gain of 27.5556 decibels. Also, the proposed algorithm gives more PSNR gain of average 2.5 decibels than the Perona-Malik method which is better than the Gaussian smoothing and the Bilateral filtering. Hence, the overall performance of the proposed algorithm is better for different noise variances.

Table 5.3 shows the quantitative results for metric mean square error (MSE) for all of the images and the noise variances. The MSE value should be less for the better performance of a method. It can be seen from the Table 5.3 that the proposed algorithm is giving the least MSE value when compared to the other three methods. The average MSE value for the noisy Pentagon image is 72.8941. However, the average MSE value for methods Gaussian Smoothing, Bilateral Filtering and Perona-Malik methods are 68.0283, 61.7973 and 56.8570 respectively. The proposed algorithm gives less MSE value than

the compared methods viz. 52.4778 which shows that the proposed algorithm is better than the other existing methods.

Table 5.4 shows the results for the metric SSIM. SSIM should be higher and near to 1 for the structural similarity of the original and the recovered images. The proposed algorithm gives the better SSIM values than the compared methods. The average SSIM value for the proposed algorithm is 0.7851 for Lena image and 0.7962 for the Boat image. Perona-Malik method performs better than methods Gaussian Smoothing, Bilateral Filtering. The increase in the SSIM value is 0.03-0.16 when compared to Perona-Malik method. Thus, the proposed algorithm performs best when compared to the three existing algorithms in case of all the metrics.

The visual results for the noise variance 0.015 are shown in Figure 5.3 - Figure 5.7 respectively. The first image in each figure shows the noisy images. The second and third images shows the recovered images using the Gaussian smoothing and the bilateral filtering method. The fourth image shows the denoising results of Perona-Malik method [117]. The fifth image in each figure shows the images recovered using the proposed algorithm and the last image is the respective ground truth image. It can be seen from each of the figures that the recovered image using the proposed algorithm preserves edges and removes noise better than other three methods. Hence, this analysis shows the proposed algorithm performs better than the existing algorithms in case of edge perseverance as well as in case of noise removal.

5.5 Conclusions

A fractional order anisotropic diffusion method has been developed using the wavelet transform based subspace decomposition in order to remove the additive white Gaussian noise. The method was found directionally sensitive in order to preserve the edges in a better way. From the experimental results, it has been observed that the proposed algorithm over-performed with all three existing methods used in the comparison study. Moreover, fractional derivatives based convolution filter implemented in the

Table 5.2: Comparison of the PSNR results obtained with algorithms Gaussian smoothing, Bilateral filtering [144], Perona-Malik [117] and the proposed algorithm with varying variances

Image	Sigma	0.010	0.015	0.020	0.025	0.030	0.035
Lena	Noisy	20.0653	18.3618	17.1787	16.2818	15.5679	14.9737
	GS	23.8992	22.1941	21.0121	20.1221	19.3957	18.8053
	BF	23.0920	20.9658	19.3870	18.1379	17.1786	16.3863
	PM	27.2132	27.2118	27.1458	27.1161	27.0059	26.9286
	Proposed	**30.0059**	**29.4316**	**28.7680**	**28.2085**	**27.6334**	**27.0425**
Pentagon	Noisy	20.0018	18.2634	17.0301	16.1028	15.3472	14.7354
	GS	23.6508	21.9712	20.7723	19.8639	19.1184	18.5120
	BF	19.3748	18.3193	17.3577	16.5200	15.8029	15.1812
	PM	23.6086	23.6180	23.6108	23.6101	23.6209	23.6045
	Proposed	**26.9572**	**26.6891**	**26.3613**	**25.9714**	**25.5803**	**25.1753**
Wallpaint	Noisy	20.1733	18.4746	17.2941	16.4010	15.6771	15.0672
	GS	24.0004	22.2868	21.1058	20.2063	19.4809	18.8579
	BF	24.4110	21.7795	19.9827	18.6416	17.5996	16.7604
	PM	24.4310	24.3866	23.9242	23.3083	22.8488	22.3583
	Proposed	**27.3394**	**26.9876**	**26.5535**	**26.1296**	**25.7518**	**24.0602**
Boat	Noisy	20.1115	18.4256	17.2460	16.3420	15.6350	15.0347
	GS	23.9495	22.2624	21.0726	20.1668	19.4598	18.8515
	BF	24.5343	21.8062	19.9840	18.6313	17.5711	16.7267
	PM	27.4148	26.4195	25.6636	25.0236	24.5364	24.0569
	Proposed	**29.6003**	**29.0407**	**28.4876**	**27.9210**	**27.4150**	**26.8395**
Pepper	Noisy	20.1621	18.4663	17.2726	16.3763	15.6719	15.0776
	GS	23.9807	22.2823	21.0791	20.1814	19.4734	18.8799
	BF	22.3272	20.5430	19.1142	17.9841	17.0626	16.3070
	PM	27.6189	27.5070	27.3764	27.1944	27.0727	26.9161
	Proposed	**29.7989**	**29.0773**	**28.4841**	**27.7688**	**27.2514**	**26.7488**

subspace based decomposition image which is easy to implement. The proposed algorithm can be implemented easily on parallel chips for efficient computation.

Table 5.3: Comparison of the MSE results obtained with algorithms Gaussian smoothing, Bilateral filtering [144], Perona-Malik [117] and the proposed algorithm with varying variances

Image	Sigma	0.010	0.015	0.020	0.025	0.030	0.035
Lena	Noisy	51.0939	61.6988	68.2040	73.0663	77.1616	79.9997
	GS	43.4090	54.4257	61.2509	66.5747	70.9836	74.0162
	BF	37.8628	39.2769	42.3936	45.9277	52.1469	56.9670
	PM	22.6129	29.9291	38.7897	44.1331	46.4495	49.0773
	Proposed	**21.3129**	**26.6278**	**30.6464**	**33.4016**	**35.7124**	**38.2358**
Pentagon	Noisy	59.0129	67.0430	72.8855	76.6868	79.6588	82.0778
	GS	55.5219	63.6421	66.9998	70.9525	74.2113	76.8424
	BF	52.9669	61.0734	63.8009	63.9147	63.8466	65.1814
	PM	49.9857	52.6390	54.4711	57.8136	61.7573	64.4750
	Proposed	**42.8636**	**47.8729**	**53.5123**	**56.0237**	**57.0331**	**57.5613**
Wallpaint	Noisy	54.6510	65.3596	72.1793	76.8656	81.2895	84.5612
	GS	51.4266	60.0139	66.3006	71.2677	76.1563	79.6767
	BF	48.7609	58.9813	62.3142	64.9803	67.7275	70.0222
	PM	48.0269	54.5534	59.0594	63.0050	66.0220	69.5165
	Proposed	**38.7730**	**46.8909**	**54.1603**	**59.9798**	**65.6248**	**68.2251**
Boat	Noisy	52.0104	63.2914	69.9670	75.3015	78.3225	81.4156
	GS	46.5790	59.3553	63.3172	69.1534	74.9108	75.7451
	BF	44.7300	56.3019	51.3005	54.7549	72.3707	61.3017
	PM	33.7158	49.1827	45.0550	52.4750	55.7535	58.0517
	Proposed	**29.3322**	**37.7812**	**41.4907**	**44.7120**	**46.9661**	**48.9135**
Pepper	Noisy	56.9715	66.1138	72.7064	77.1338	82.4249	85.0895
	GS	53.1690	59.6645	66.6145	71.3152	77.1776	79.9733
	BF	48.3671	49.8659	52.2312	64.7672	62.2046	66.1371
	PM	33.1250	40.4624	48.2731	54.6979	59.2250	61.2849
	Proposed	**30.9879**	**35.1705**	**38.5463**	**41.6561**	**45.4086**	**47.7725**

Table 5.4: Comparison of the SSIM results obtained with algorithms Gaussian smoothing, Bilateral filtering [144], Perona-Malik [117] and the proposed algorithm with varying variances

Image	Sigma	0.010	0.015	0.020	0.025	0.030	0.035
Lena	Noisy	0.5064	0.4316	0.3807	0.3469	0.3162	0.2955
	GS	0.5757	0.4991	0.4456	0.4095	0.3757	0.3534
	BF	0.5231	0.5076	0.4888	0.4849	0.4690	0.5245
	PM	0.7958	0.7746	0.7583	0.7457	0.7340	0.7230
	Proposed	**0.8342**	**0.8136**	**0.7940**	**0.7762**	**0.7544**	**0.7383**
Pentagon	Noisy	0.5696	0.4985	0.4448	0.4054	0.3750	0.3495
	GS	0.6178	0.5517	0.4993	0.4603	0.4293	0.4031
	BF	0.2078	0.4033	0.3707	0.2159	0.3223	0.3751
	PM	0.5625	0.5335	0.5107	0.4944	0.4807	0.4695
	Proposed	**0.6618**	**0.6546**	**0.6441**	**0.6327**	**0.6197**	**0.6072**
Wallpaint	Noisy	0.6337	0.5634	0.5109	0.4697	0.4343	0.4087
	GS	0.6881	0.6217	0.5704	0.5284	0.4929	0.4664
	BF	0.3226	0.3533	0.3846	0.3331	0.3785	0.3261
	PM	0.6465	0.6107	0.5804	0.5566	0.5366	0.5200
	Proposed	**0.7445**	**0.7342**	**0.7226**	**0.7081**	**0.6947**	**0.6824**
Boat	Noisy	0.5551	0.5523	0.4767	0.4256	0.3586	0.3327
	GS	0.6226	0.6193	0.5432	0.4907	0.4195	0.3916
	BF	0.6591	0.6580	0.6550	0.6584	0.6495	0.6579
	PM	0.7716	0.7711	0.7424	0.7192	0.6875	0.6754
	Proposed	**0.8365**	**0.8348**	**0.8166**	**0.7834**	**0.7621**	**0.7439**
Pepper	Noisy	0.4894	0.4196	0.3698	0.3369	0.3106	0.2882
	GS	0.5535	0.4831	0.4311	0.3958	0.3669	0.3425
	BF	0.5126	0.5004	0.5169	0.5009	0.4965	0.5074
	PM	0.7690	0.7493	0.7320	0.7171	0.7053	0.6942
	Proposed	**0.7951**	**0.7777**	**0.7589**	**0.7407**	**0.7222**	**0.7056**

Figure 5.3: (a) Noisy Lena image with variance 0.015; the recovered images using methods (b) Gaussian smoothing; (c) Bilateral filtering [144]; (d) Perona-Malik [117]; (e) the proposed algorithm; (f) ground truth image.

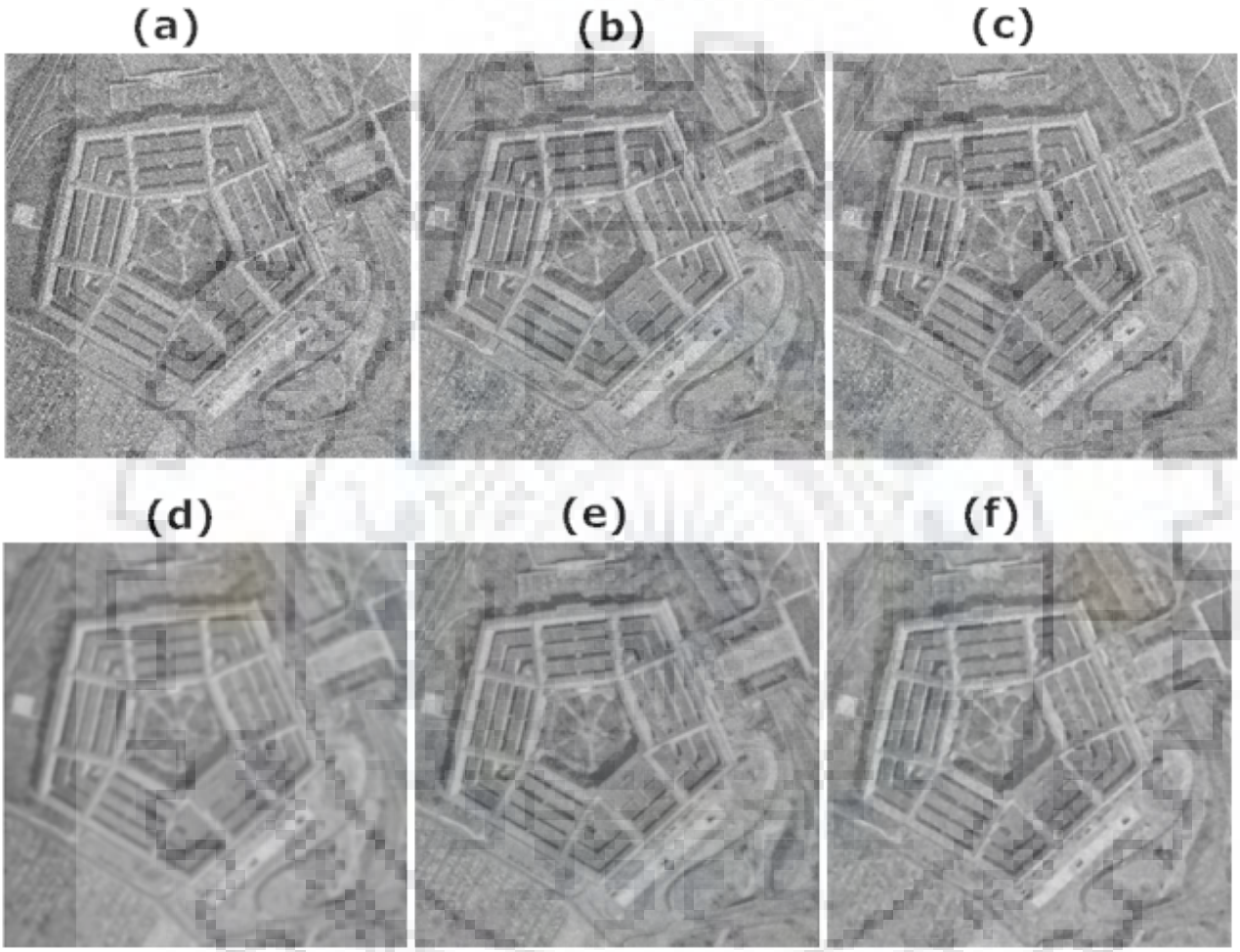

Figure 5.4: (a) Noisy Pentagon image with variance 0.015; the recovered images using methods (b) Gaussian smoothing; (c) Bilateral filtering [144]; (d) Perona-Malik [117]; (e) the proposed algorithm; (f) ground truth image.

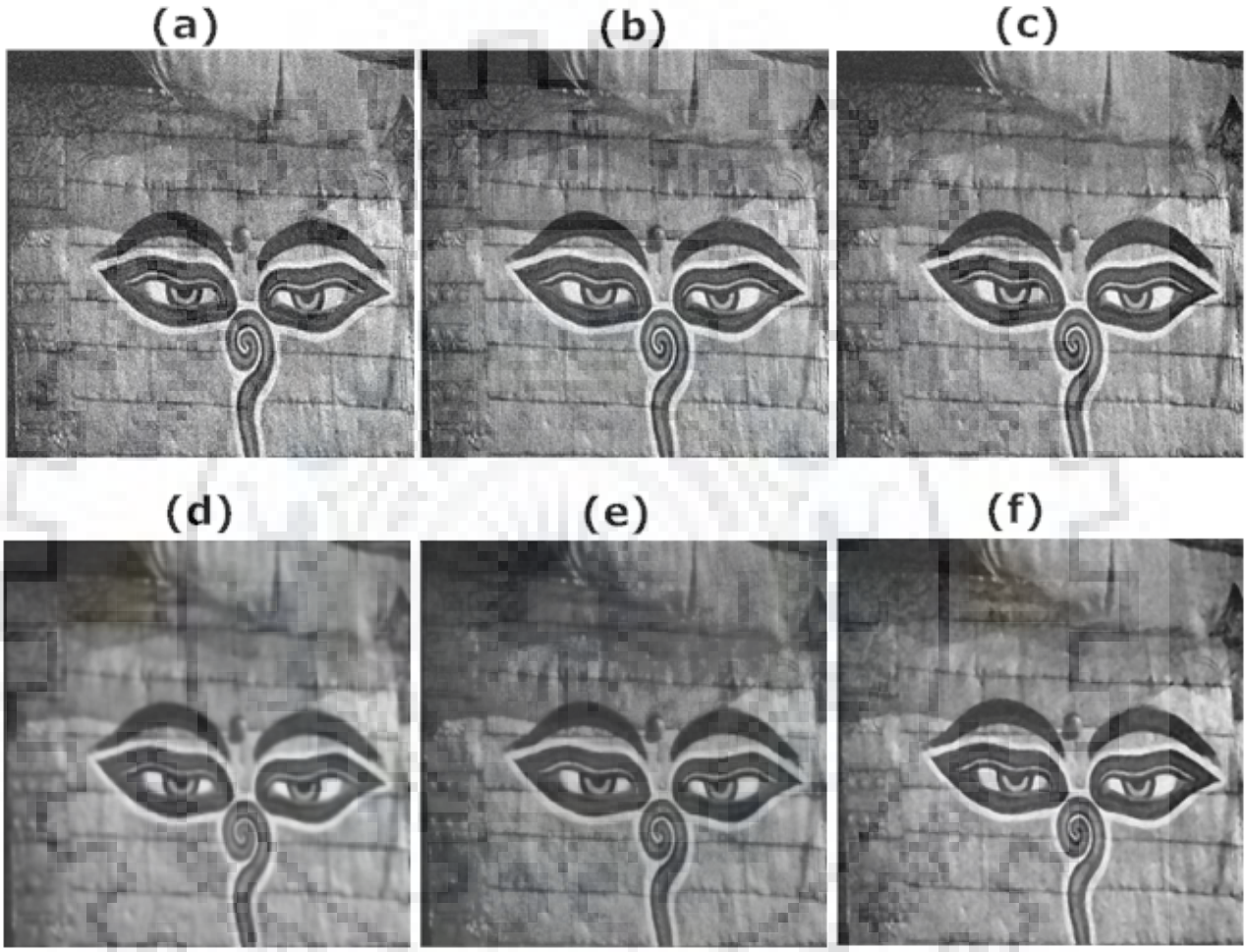

Figure 5.5: (a) Noisy Wallpaint image with variance 0.015; the recovered images using methods (b) Gaussian smoothing; (c) Bilateral filtering [144]; (d) Perona-Malik [117]; (e) the proposed algorithm; (f) ground truth image.

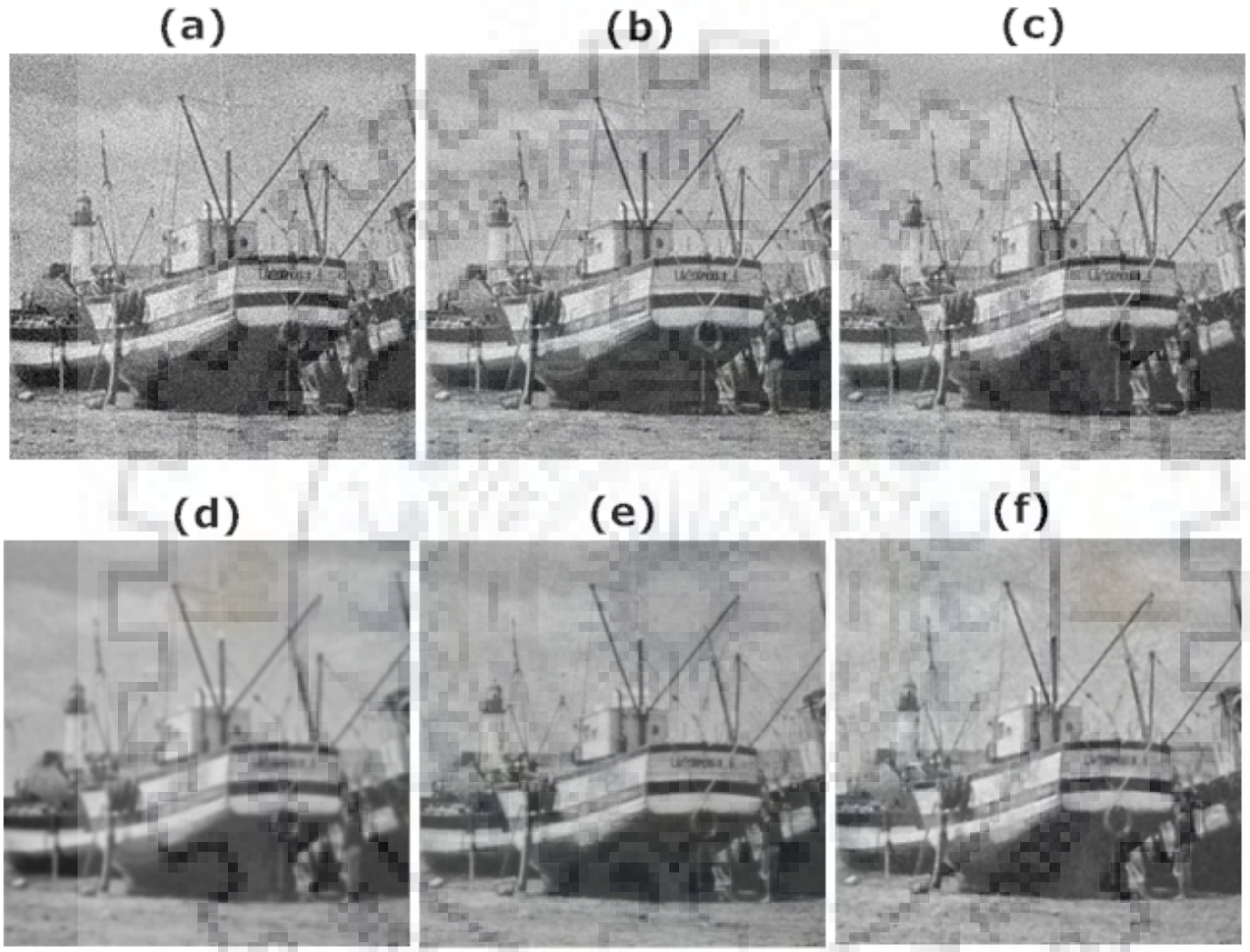

Figure 5.6: (a) Noisy Boat image with variance 0.015; the recovered images using methods (b) Gaussian smoothing; (c) Bilateral filtering [144]; (d) Perona-Malik [117]; (e) the proposed algorithm; (f) ground truth image.

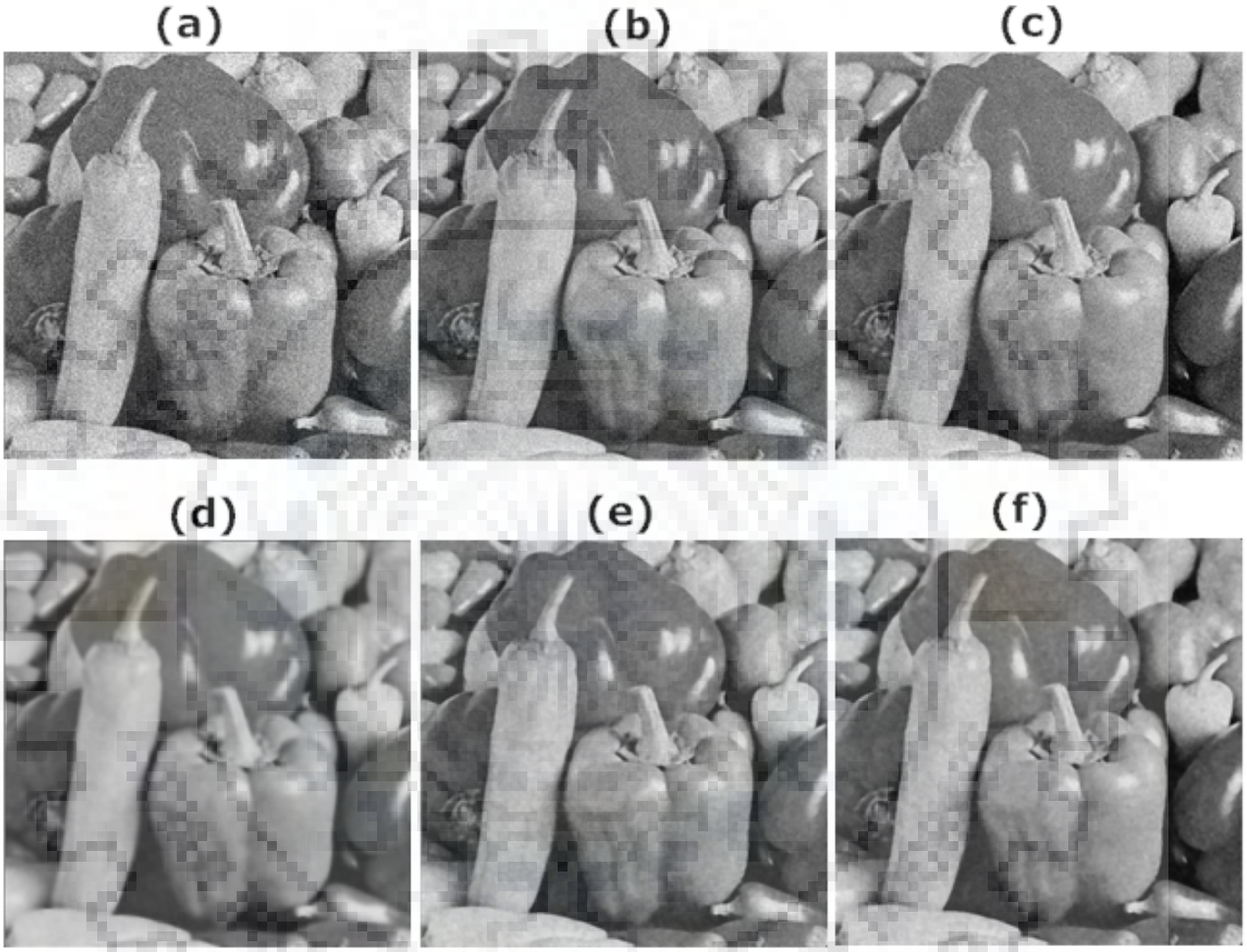

Figure 5.7: (a) Noisy Pepper image with variance 0.015; the recovered images using methods (b) Gaussian smoothing; (c) Bilateral filtering [144]; (d) Perona-Malik [117]; (e) the proposed algorithm; (f) ground truth image.

Chapter 6

Image denoising and defogging using fractional gradient based improved diffusion coefficient

6.1 Introduction

In previous chapter, the image denoising problem is dealt in various sub-bands of wavelet domain by choosing appropriate diffusion directions. In this chapter, a new non-linear fractional order diffusion coefficient is proposed. The proposed diffusion coefficient makes use of *tansig* function as the diffusion coefficient with fractional order gradients. This diffusion coefficient along with anisotropic diffusion of fractional order gradients is applied to image restoration problems (image defogging and image denoising) to have improved results. The convergence of the proposed algorithm can be speed up by modifying the tangent direction. The fractional order derivatives are used in Riemann-Liouville sense which is just a convolution of two functions. The proposed algorithm is adapted for noisy as well as hazy images which are corrupted due to natural or synthetic haze and additive noise.

In literature, many image filtering based methods were designed to improve noisy images corrupted

under uncertain camera sensor situations. Perona and Malik defined two diffusion coefficients for edge prevention based on gradient of an image [117]. After that, there has been many enhancements in diffusion functions for better image restoration. Catte et al. regularized the Perona-Malik diffusion function by smoothing the gradient by using a Gaussian kernel to get a unique solution. Later on, this diffusion coefficient has been rectified by Whitaker et al. [154]. Authors [96] then suggested to decrease the contrast parameter which followed by Gaussian convolution of the exponential filter defined by [129, 145]. There has been many improvements in the diffusion coefficients for better edge preservation and enhancement [15, 18]. In 2016, Tebini et al. [142] presented a new mathematical model to avoid the drawbacks of existing models. This model used the tansig function to optimize the trade-off between noise removal and edge preservation. This function is designed in order to have a fast real-time implementation.

In hazy conditions also, the quality of outdoor images is bad because of water droplets and dust particles in the atmosphere. The water droplets in the air scatters the light which causes poor visibility of an image. Thus it is essential to recover the degraded images. Image defogging is also an ill-posed problem like image denoising, thus needs to recover the haze free image from the degraded one. In this chapter, the proposed algorithm recovers the noisy and hazy images by using tansig function as the diffusion coefficient with fractional order smoothed gradients. Only few parameters are needed to select manually in the proposed algorithm. The presented results validate the performance of the proposed algorithm for image denoising and image defogging.

6.2 The proposed algorithm

6.2.1 Image denoising model

The image denoising model can be mathematically defined as

$$I = I_0 + \eta \tag{6.1}$$

where, I_0 is the image which needs to be restored and η stands for the additive white Gaussian noise (AWGN). The amount of noise is dependent on image i.e. noise is higher for higher intensity values of the noise free image. For grey images, the intensity of the pixels lies in range $[0, 255]$, where, 0 is the least intensity value which represents black and 255 is the highest intensity value which represents white. It is not easy that just smoothing of noisy image will get the work done. It is needed to maintain the sharp features of the images lost due to the presence of noise η.

6.2.2 Diffusion scheme

To restore a noise free image, we need to solve the following PDE

$$\frac{\partial I}{\partial t} = div\left(g(|\nabla I|^2)\nabla I\right) \tag{6.2}$$

with conditions $I(x, 0) = I_0(x) \quad \forall\ x \in \Omega$ and natural boundary conditions. This PDE can be approximated using a numerical scheme based on the finite differences as given in [117]. The conduction coefficients defined by Perona-Malik [117] are given as

$$g_1(|\nabla I|^2) = exp\left(-\left(\frac{\nabla I}{\kappa}\right)^2\right) \quad or \quad g_2(|\nabla I|^2) = \frac{1}{1 + (\frac{\nabla I}{\kappa})^2}$$

The gradients in the Perona-Malik scheme are calculated in eight directions viz. $N, S, E, W, NW, SW, NE, SE$ as follows:

$$\nabla_N I(i,j) = I(i-1,j) - I(i,j)$$

$$\nabla_S I(i,j) = I(i+1,j) - I(i,j)$$

$$\nabla_E I(i,j) = I(i,j+1) - I(i,j)$$

$$\nabla_W I(i,j) = I(i,j-1) - I(i,j)$$

$$\nabla_{NE} I(i,j) = I(i-1,j+1) - I(i,j)$$

$$\nabla_{SE} I(i,j) = I(i+1,j+1) - I(i,j)$$

$$\nabla_{SW} I(i,j) = I(i+1,j-1) - I(i,j)$$

$$\nabla_{NW} I(i,j) = I(i-1,j-1) - I(i,j)$$

Tebini et al. [142] provided a new non-linear diffusion function based on tansig function defined as:

$$g_3(|\nabla I|) = \frac{1}{2}\left[\left(1 + \text{tansig}\left(-\text{abs}\left(\frac{\nabla I}{k}\right)\right)\right) + \left(1 + \text{tansig}\left(-\text{abs}\left(\frac{\Delta I}{k}\right)\right)\right)\right] \tag{6.3}$$

However, to recover image from the noisy one, we have considered the following fractional order PDE

$$\frac{\partial I}{\partial t} = div\left(g(|\nabla^\alpha I|^2)\nabla^\alpha I\right) \tag{6.4}$$

where, $\nabla^\alpha I$ is the fractional order gradient having fractional orders in range $(1, 2)$. The fractional order anisotropic diffusion have been applied with smoothed fractional order gradients and a different fractional order diffusion coefficient as defined below:

$$g(|\nabla I|) = \left[\left(1 + \text{tansig}\left(-\text{abs}\left(\frac{(\nabla^\alpha I)}{k}\right)\right)\right)\right] \tag{6.5}$$

where, ∇ is the gradient operator, and k is the threshold parameter which controls the diffusion process and determines the contrast of the edges which needs to be retained. Here, the considered function is tansig function as the diffusion coefficient with fractional order gradients. The proposed conductance function is better than the conductance function by Tebini et al. [142] because of the following reasons:

- The proposed function contains derivatives with fractional order gradients, whereas, in Tebini et al. [142] diffusion function, both first and second order gradients were considered.
- Tebini et al. [142] diffusion function lies in range $[-1, 1]$, however, the proposed function range is $[0, 1]$ only.
- It has better convergence speed than Tebini et al. [142] diffusion function.

Figure 6.1 shows a graph of various diffusion coefficients and the proposed diffusion coefficient with a $\alpha = 1.5$. The diffusion coefficient should act in a way that most of the filtering has to be done in the areas with small gradients. In the areas of larger gradients, filtering amount should be less. From Figure 6.1, we can see that the proposed diffusion function converges faster than other methods. It can be seen from Figure 6.1 that, the diffusion functions of Perona-Malik scheme and Tebini et al. method

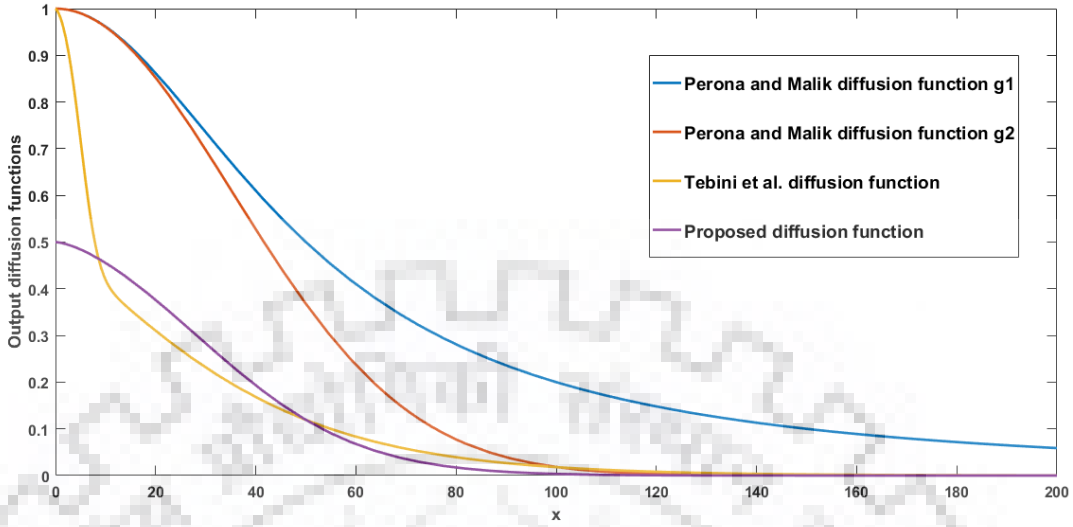

Figure 6.1: Diffusion functions of various models

converges very gently and it continues to perform smoothing and filters the image. However, the proposed diffusion function reaches to zero value at a faster rate as compared to other three diffusion functions. It implies that the diffusion process is stopped after a fix period of time and does not over-smooth the recovered image. Thus, the proposed diffusion function preserves the edges better than the other three diffusion functions. The proposed diffusion function smoothes the low gradient areas rapidly and slows down the process in high gradient areas.

6.2.3 Implementation

To restore images, the proposed algorithm uses the following fractional order PDE

$$\frac{\partial I}{\partial t} = div\left(g(|\nabla^{\alpha} I|^2)\nabla^{\alpha} I\right) \tag{6.6}$$

where, $g|\nabla^{\alpha} I|$ is the fractional order diffusion function defined as

$$g(|\nabla I|) = \left[\left(1 + \text{tansig}\left(-\text{abs}\left(\frac{|\nabla_i^{\alpha} I|}{k}\right)\right)\right)\right] \tag{6.7}$$

where, i denotes the directions viz. $N, S, E, W, NE, NW, SE, SW$ in which the fractional order anisotropic

diffusion is being applied. The filter M_{∇^α} is used to calculate the fractional order gradients in all the directions. The filter M_{∇^α} is the generic filter which changes based on the direction of the gradients.

$$M_{\nabla^\alpha} = \begin{array}{|c|c|c|c|c|} \hline \frac{\alpha^2-\alpha}{2} & 0 & \frac{\alpha^2-\alpha}{2} & 0 & \frac{\alpha^2-\alpha}{2} \\ \hline 0 & -\alpha & -\alpha & -\alpha & 0 \\ \hline \frac{\alpha^2-\alpha}{2} & -\alpha & 8 & -\alpha & \frac{\alpha^2-\alpha}{2} \\ \hline 0 & -\alpha & -\alpha & -\alpha & 0 \\ \hline \frac{\alpha^2-\alpha}{2} & 0 & \frac{\alpha^2-\alpha}{2} & 0 & \frac{\alpha^2-\alpha}{2} \\ \hline \end{array}$$

For example, to calculate the fractional order gradient in N direction, filter will be defined as below:

$$M_{\nabla^\alpha_N} = \begin{array}{|c|c|c|c|c|} \hline 0 & 0 & \frac{\alpha^2-\alpha}{2} & 0 & 0 \\ \hline 0 & 0 & -\alpha & 0 & 0 \\ \hline 0 & 0 & 8 & 0 & 0 \\ \hline 0 & 0 & 0 & 0 & 0 \\ \hline 0 & 0 & 0 & 0 & 0 \\ \hline \end{array}$$

The proposed diffusion function is non-linear in nature and has a threshold value of 1. It can be customized in order to speed up the convergence by changing the tangent directions.

The scheme used to find solution of fractional order PDE given in (6.6) is same as the scheme used in previous chapter. Only difference is that, here wavelet subbands based filtering have not been considered. The PDE (6.6) is approximated using the following numerical scheme:

$$\begin{aligned} {I_k}^{t+1} = {I_k}^t + \lambda(g_N \cdot \bigtriangledown^\alpha_N I + g_S \cdot \bigtriangledown^\alpha_S I + g_W \cdot \bigtriangledown^\alpha_W I + g_E \cdot \bigtriangledown^\alpha_E I + \\ g_{NE} \cdot \bigtriangledown^\alpha_{NE} I + g_{NW} \cdot \bigtriangledown^\alpha_{NW} I + g_{SE} \cdot \bigtriangledown^\alpha_{SE} I + g_{SW} \cdot \bigtriangledown^\alpha_{SW} I) \end{aligned} \tag{6.8}$$

6.2.4 Properties of flow function

The flow function $\phi(I)$ of an image $f(I)$ is defined as

$$\phi(I) = I \cdot g(|\nabla I|)$$

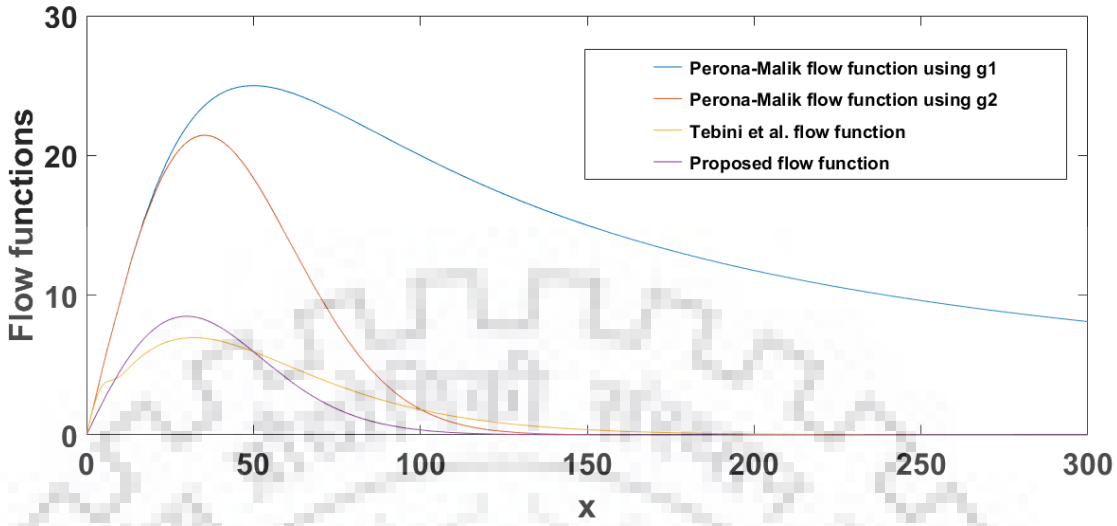

Figure 6.2: Flow functions of different models

where, $g(|\nabla I|)$ is the diffusion function. Flow function for Perona-Malik diffusion coefficients are defined as

$$\phi_1(I) = I \cdot g_1(|\nabla I|) \tag{6.9}$$

$$\phi_2(I) = I \cdot g_2(|\nabla I|) \tag{6.10}$$

The flow function of Tebini et al. method [142] is defined as

$$\phi_3(I) = I \cdot g_3(|\nabla I|) \tag{6.11}$$

Here, the proposed flow function is defined as

$$\phi_{proposed}(I) = I \cdot \left[\left[\left(1 + tansig\left(-abs\left(\frac{(\nabla^{\alpha} I)}{k}\right)\right)\right)\right]\right] \tag{6.12}$$

Figure 6.2 shows the graphs for flow functions ϕ_1, ϕ_2, ϕ_3 and $\phi_{proposed}$. In function $\phi_{proposed}$, we have used the fractional order as 1.5. This function increases when smoothing is performed in the smooth regions and goes on decreasing for smoothing in sharp details region. Figure 6.2 shows that proposed flow function decreases at a faster rate than the compared flow functions.

Table 6.1: Structural similarity (SSIM) obtained with the proposed algorithm with different fractional orders α with variance 0.002 and 3 iterations as stopping criteria.

$\alpha =$	Noisy Image	**1.0**	**1.2**	**1.4**	**1.6**	**1.8**
Lena	0.6895	0.9099	**0.9120**	0.9113	0.9118	0.9115
Stone	0.6064	0.8916	0.8926	0.8922	0.8930	**0.8932**
Rice	0.7495	0.9086	0.9102	0.9105	0.9108	**0.9109**
Sparrow	0.7074	0.9175	0.9180	0.9186	**0.9193**	0.9189
Tower	0.6643	0.9015	0.9029	0.9022	0.9018	**0.9030**
Flower	0.6590	0.9003	0.9010	0.9013	0.9015	**0.9021**
Average	0.6793	0.9049	0.9061	0.9060	0.9063	**0.9066**

6.3 Simulation results

6.3.1 Results on image denoising

In order to check the efficiency of the proposed algorithm in case of denoising, a set of test images namely *Lena*, *Stone*, *Rice*, *Sparrow*, *Tower* and *Flower* have been considered. The considered test images are corrupted with additive white Gaussian noise (AWGN) with a variance of 0.002. The metrics used to testify the proposed algorithm performance are structural similarity (SSIM), Peak signal to noise ratio (PSNR) and Mean square error (MSE). The metric values of SSIM and PSNR should be higher for better performance of a method.

Table 6.1 shows the quantitative results of the proposed algorithm with different fractional orders in range $[1, 2]$. For $\alpha = 1$, this method reduce into integer order for the proposed algorithm. The initial noisy images have an average of SSIM value of 0.6793. The proposed algorithm gives average SSIM values in range 0.9061-0.9066, however, the integer order has a maximum average SSIM value of 0.9049. The numerical results of proposed fractional order method are better than the integer order for each image. Table 6.2 shows the numerical results for metric PSNR. It can be seen from table 6.2 and table 6.3 that our method clearly performs better than the integer order. PSNR values lies in range $32.3975 - 32.4900$ decibels. Similar results holds for metric mean square error (MSE).

Table 6.2: Peak signal to noise ratio (PSNR) obtained with the proposed algorithm with different fractional orders α with variance 0.002 and 3 iterations as stopping criteria.

$\alpha =$	Noisy Image	**1.0**	**1.2**	**1.4**	**1.6**	**1.8**
Lena	27.8381	32.4145	**32.4555**	32.4210	32.4309	32.4371
Stone	27.1413	31.8690	32.0576	32.0712	**32.2484**	32.1723
Rice	28.3251	32.5054	32.5262	32.5140	32.5638	**32.5976**
Sparrow	28.0165	32.7333	32.7454	32.7514	32.7348	**32.7525**
Tower	27.9697	32.7599	32.8294	32.7694	32.8403	**32.8405**
Flower	27.5674	32.1032	32.1142	**32.1410**	32.1221	32.1208
Average	27.8096	32.3975	32.4546	32.4445	**32.4900**	32.4870

Table 6.4 shows the comparison of the proposed algorithm with existing methods such as Perona and Malik [117], Guided filtering [57] and adaptive and anisotropic filtering (AAF) [142]. Figure 6.3 - Figure 6.8 shows the visual denoising results of the proposed algorithm along with some of the existing algorithms. The first image in each figure shows the noisy images. The second, third and fourth images shows the images recovered using Perona and Malik method [117], Guided image filtering [57] and adaptive and anisotropic filtering (AAF) method [142]. The proposed visual results are shown in fifth image and the last image in each figure shows the ground truth images. From numerical as well as visual results, it can be clearly observed that the proposed algorithm results are much better than the existing algorithms.

6.3.2 Results on image dehazing

The proposed algorithm ia also implemented on the outdoor hazy images. The considered hazy images are *Building*, *Lady*, *Light*, *Pond* and *Street* taken from SOTS data set [93]. The accuracy of the proposed algorithm is evaluated in terms of metric like structural similarity (SSIM) and colorfulness index (CI). The values of both the metrics must be higher for better performance. Table 6.5 shows the SSIM results of our method with varying fractional order α in range $[1, 2)$. The average SSIM values

Table 6.3: Mean square error (MSE) obtained with the proposed algorithm with different fractional orders α with variance 0.002 and 3 iterations as stopping criteria.

$\alpha =$	Noisy Image	**1.0**	**1.2**	**1.4**	**1.6**	**1.8**
Lena	106.9726	11.4827	11.4170	11.4316	**11.1932**	11.2074
Stone	114.0656	9.5661	**9.0768**	9.3256	9.3067	9.2625
Rice	95.6248	13.0148	12.6933	**12.4555**	12.5697	12.6891
Sparrow	102.6681	12.8689	12.2561	**12.1210**	12.3155	11.7924
Tower	103.7801	11.5963	11.5012	**11.2355**	11.3656	11.5787
Flower	113.6389	12.4582	12.4238	12.3694	12.3310	**12.1940**
Average	106.1250	11.8311	11.5613	11.4900	11.5138	**11.4540**

Table 6.4: Comparison of the results obtained with existing algorithms Perona-Malik [117], Guided Filtering [57], AAF [142] and the proposed algorithm

Metric	Algorithm	Lena	Stone	Rice	Sparrow	Tower	Flower
SSIM	Perona-Malik	0.7487	0.8014	0.7495	0.7189	0.7661	0.7491
	Guided Filtering	0.8839	0.8830	0.8872	0.8838	0.8804	0.8866
	AAF	0.8930	0.8894	0.8942	0.9021	0.8958	0.8914
	Proposed	**0.9120**	**0.8932**	**0.9109**	**0.9193**	**0.9030**	**0.9021**
PSNR	Perona-Malik	25.5408	25.8552	24.2539	25.2644	26.2466	24.9774
	Guided Filtering	31.5112	31.9650	30.8569	31.4311	32.0038	31.5760
	AAF	31.8731	31.3678	31.0628	31.7622	31.8947	31.8210
	Proposed	**32.4555**	**32.2484**	**32.5976**	**32.7525**	**32.8405**	**32.1410**
MSE	Perona-Malik	41.3766	32.0810	61.0460	40.7486	32.8500	34.5626
	Guided Filtering	19.0871	14.8374	25.0184	19.8362	18.0814	18.4338
	AAF	12.6724	10.3879	12.9248	13.2981	13.0648	14.2784
	Proposed	**11.1932**	**9.0768**	**12.4555**	**12.1210**	**11.2355**	**12.1940**

Table 6.5: Structural similarity (SSIM) obtained with the proposed algorithm with different fractional orders α with 3 iterations as stopping criteria.

$\alpha =$	**1.0**	**1.2**	**1.4**	**1.6**	**1.8**
Building	0.8139	0.8148	0.8161	0.8162	**0.8166**
Lady	0.8585	0.8614	0.8637	0.8652	**0.8657**
Light	0.8159	**0.8202**	0.8180	0.8189	0.8197
Pond	0.8846	0.8909	0.8976	0.9042	**0.9107**
Street	0.8197	0.8265	0.8338	0.8409	**0.8481**
Average	0.8388	0.8428	0.8460	0.8490	**0.8524**

Figure 6.3: Comparison of the filtering method results for the Lena image: (a) Lena noisy image; (b) Perona and Malik based scheme [117]; (c) Guided filtering based scheme [57]; (d) Adaptive anisotropic filtering (AAF) based scheme [142]; (e) the proposed algorithm; (f) ground truth image.

Table 6.6: Colorfulness index (CI) obtained with the proposed algorithm with different fractional orders α with 3 iterations as stopping criteria.

$\alpha =$	**1.0**	**1.2**	**1.4**	**1.6**	**1.8**
Building	1.0478	1.0488	1.0496	1.0508	**1.0512**
Lady	0.2874	0.2877	0.2882	0.2885	**0.2889**
Light	0.8256	0.8259	0.8261	0.8264	**0.8266**
Pond	0.4436	0.4438	0.4442	**0.4447**	0.4445
Street	0.2285	0.2288	0.2290	**0.2307**	0.2296
Average	0.5668	0.5672	0.5674	**0.5684**	**0.5684**

Table 6.7: Comparison of the results obtained with existing algorithms DCP [58], FrADP, AAF [142] and the proposed algorithm

Metric	Algorithm	Building	Lady	Light	Pond	Street
SSIM	DCP	0.8200	0.6807	0.8496	0.6957	0.6479
	FrADP	**0.9153**	0.8509	**0.9009**	0.8012	0.8329
	AAF	0.8067	0.8451	0.8142	0.8962	0.8261
	Proposed	0.8166	**0.8657**	0.8202	**0.9107**	**0.8481**
CI	DCP	0.2734	0.1100	0.2999	0.2117	0.0882
	FrADP	0.2624	0.0506	0.2058	0.2802	0.0951
	AAF	1.0074	0.2785	0.8174	0.4396	0.2169
	Proposed	**1.0512**	**0.2889**	**0.8266**	**0.4447**	**0.2307**

of recovered images varies in between $0.8428 - 0.8524$. Since these values are near to 1, we can say that the proposed algorithm is performing good. Also, Table 6.6 shows the colorfulness index values for all of the images. On this metric also, the proposed algorithm results are better than the integer order. Table 6.7 shows the comparison with some of existing algorithms like Dark channel prior (DCP) [58], FrADP, Adaptive and anisotropic filtering (AAF) [142]. For only two images namely *Building* and *Light*, FrADP method is performing better in case of metric SSIM. However, for all of the images proposed algorithm results are better than the existing ones with both of the metrics. Also, we can see the visual results for all of the algorithms in Figure 6.9 - Figure 6.13. The restored images using the proposed algorithm are very much similar to the ground truth images. Hence, from this study, the proposed algorithm is efficient in removing noise as well as haze from various degraded images.

6.4 Conclusions

In this chapter, a new diffusion coefficient known as tansig function with fractional order gradients is proposed. Also, a smoothed version of fractional order anisotropic diffusion is applied in order to have a better solution. The proposed algorithm is applied on noisy as well as hazy images. The hazy images are outdoor images whose ground truth images are also available. Also, there is no blurring artifacts in the recovered images. The edges and other sharp details like corners are well preserved using the

proposed algorithm.

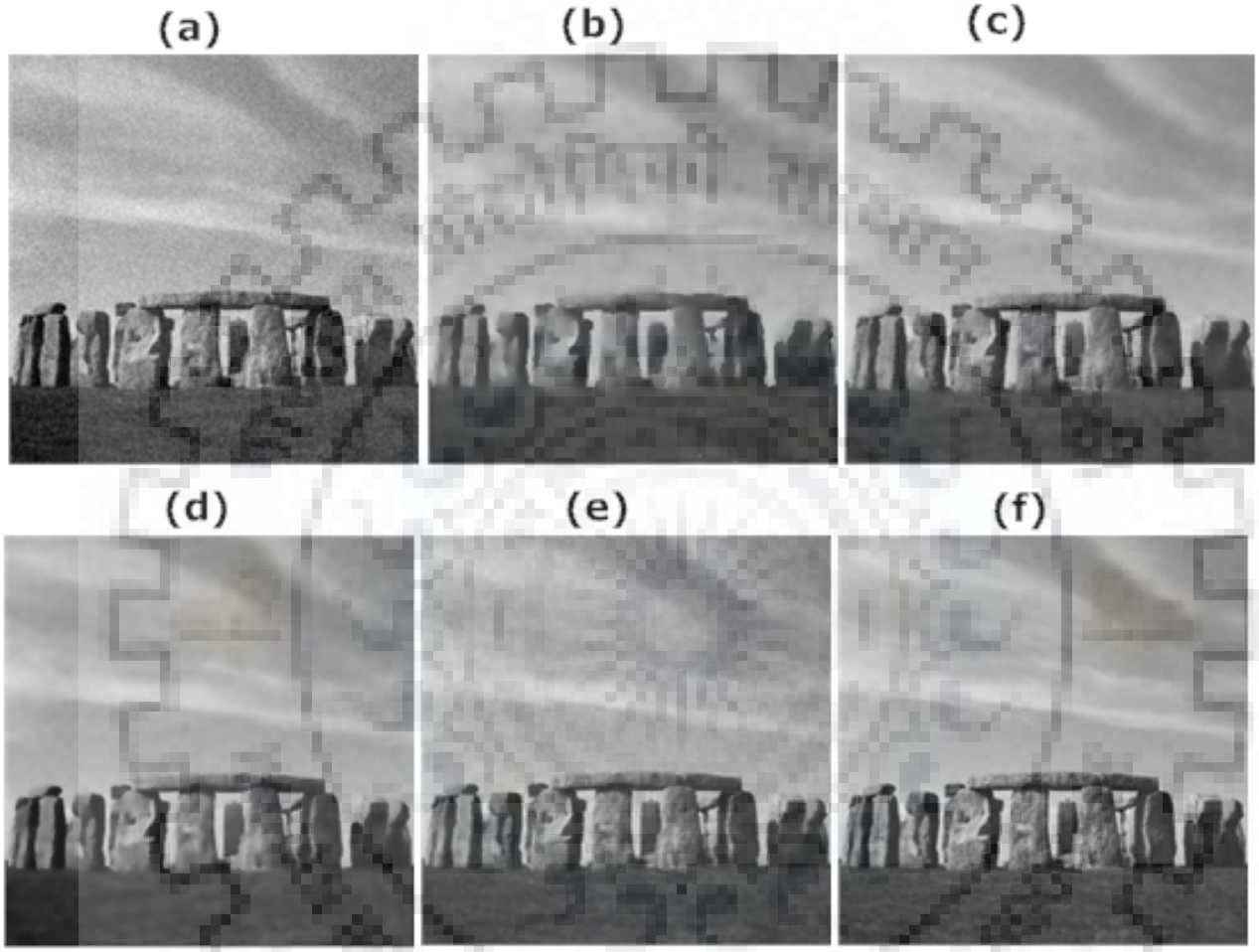

Figure 6.4: Comparison of the filtering method results for the Stone image: (a) Stone noisy image; (b) Perona and Malik based scheme [117]; (c) Guided filtering based scheme [57]; (d) Adaptive anisotropic filtering (AAF) based scheme [142]; (e) the proposed algorithm; (f) ground truth image.

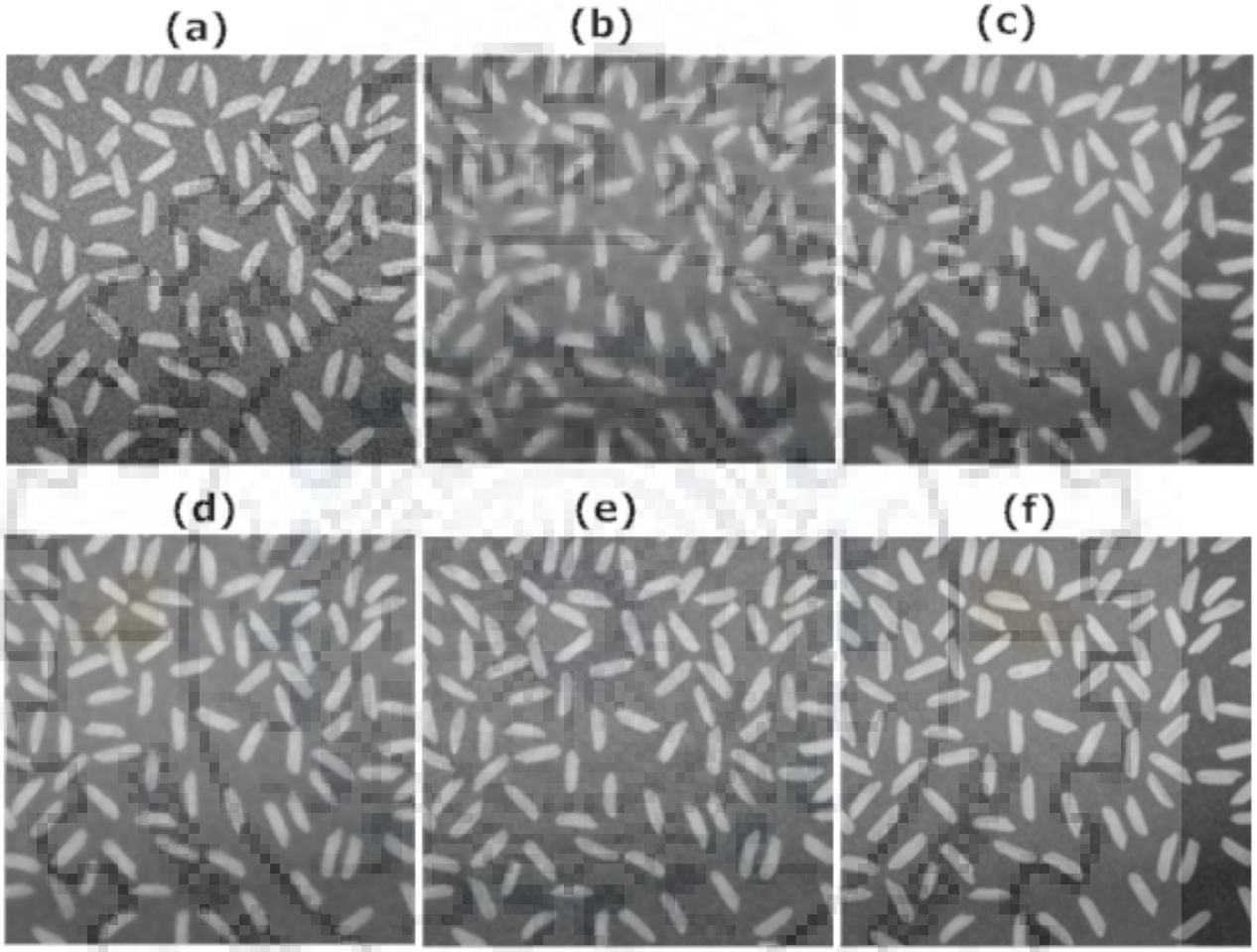

Figure 6.5: Comparison of the filtering method results for the Rice image: (a) Rice noisy image; (b) Perona and Malik based scheme [117]; (c) Guided filtering based scheme [57]; (d) Adaptive anisotropic filtering (AAF) based scheme [142]; (e) the proposed algorithm; (f) ground truth image.

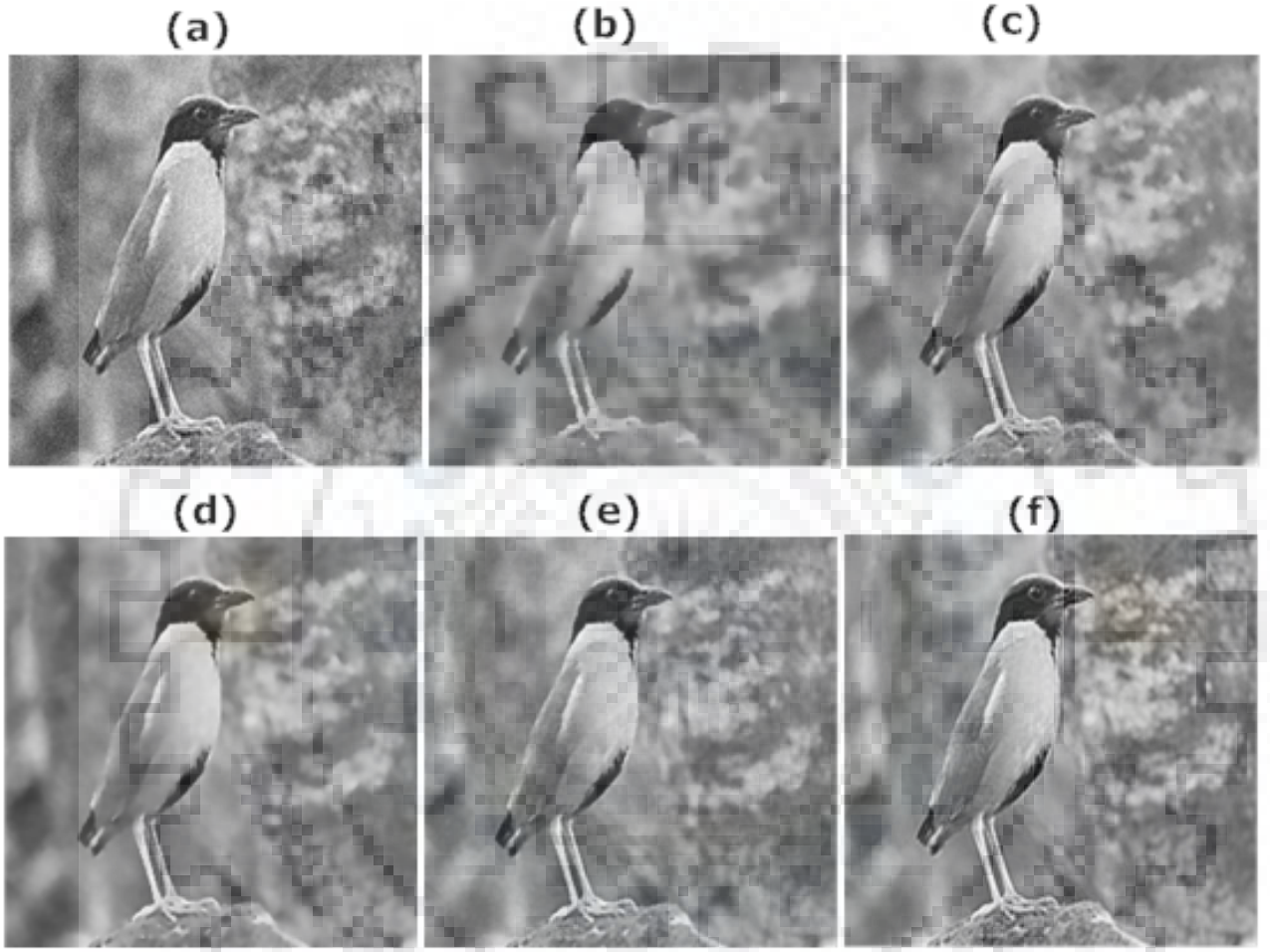

Figure 6.6: Comparison of the filtering method results for the Sparrow image: (a) Sparrow noisy image; (b) Perona and Malik based scheme [117]; (c) Guided filtering based scheme [57]; (d) Adaptive anisotropic filtering (AAF) based scheme [142]; (e) the proposed algorithm; (f) ground truth image.

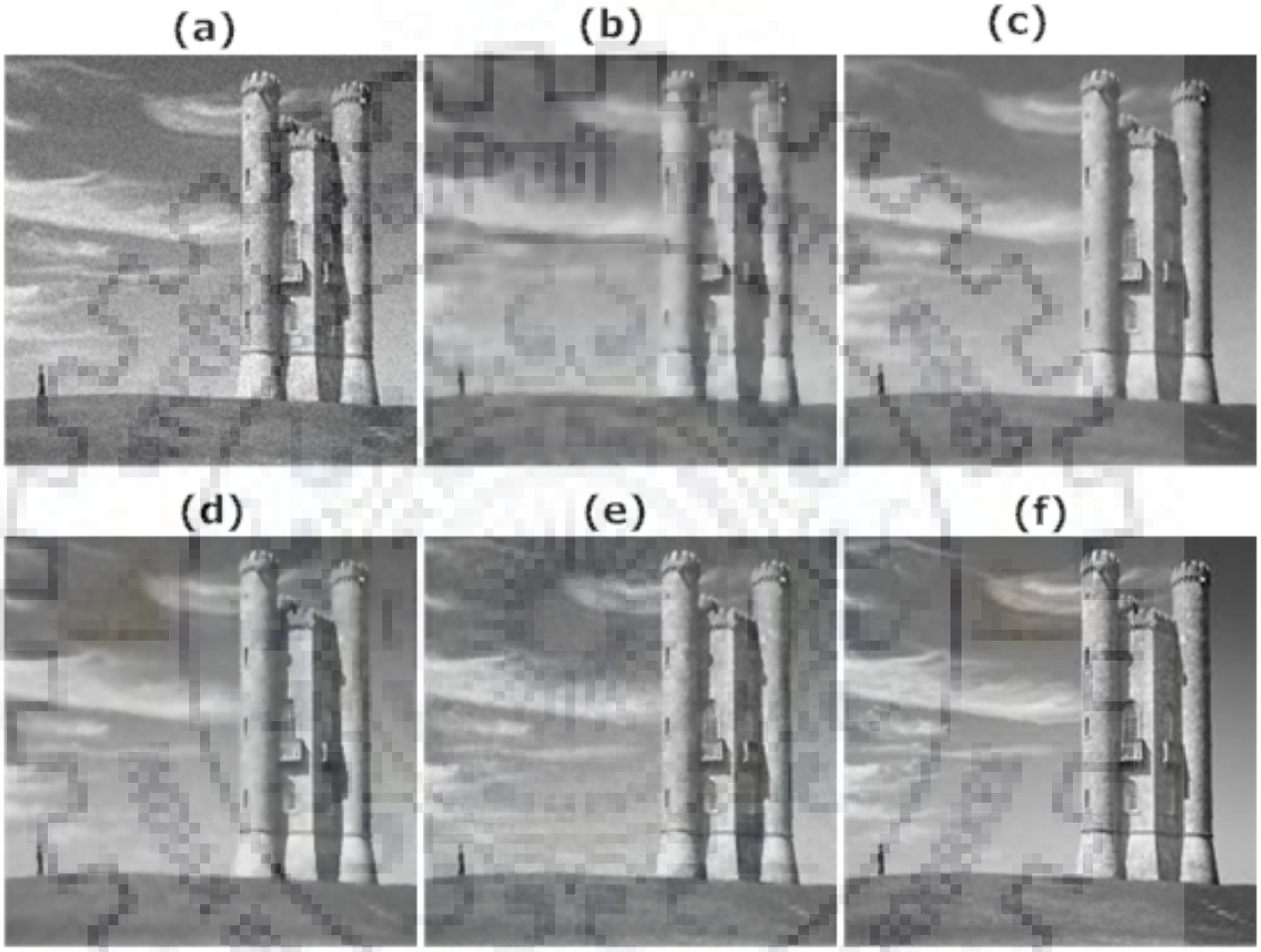

Figure 6.7: Comparison of the filtering method results for the Tower image: (a) Tower noisy image; (b) Perona and Malik based scheme [117]; (c) Guided filtering based scheme [57]; (d) Adaptive anisotropic filtering (AAF) based scheme [142]; (e) the proposed algorithm; (f) ground truth image.

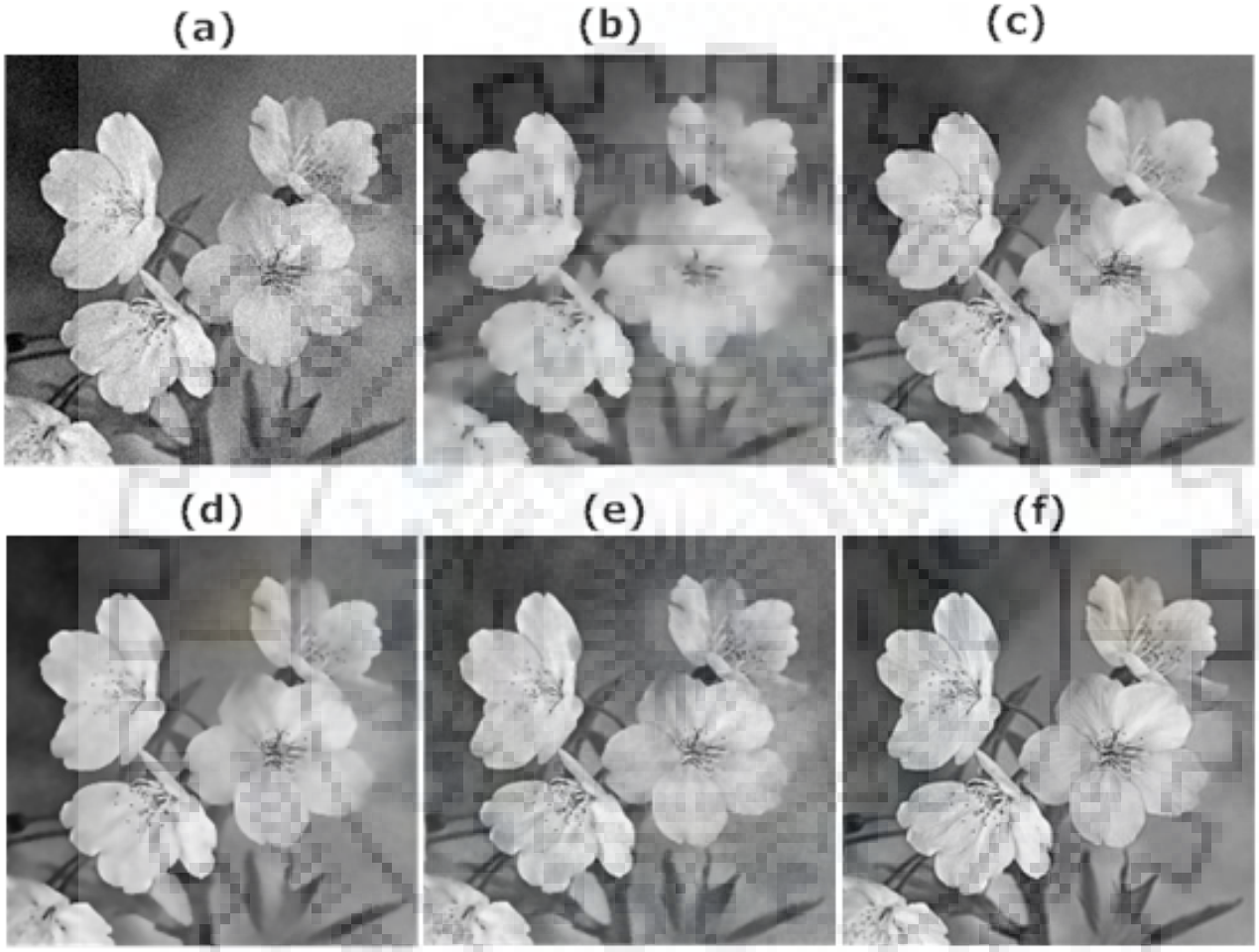

Figure 6.8: Comparison of the filtering method results for the Flower image: (a) Flower noisy image; (b) Perona and Malik based scheme [117]; (c) Guided filtering based scheme [57]; (d) Adaptive anisotropic filtering (AAF) based scheme [142]; (e) the proposed algorithm; (f) ground truth image.

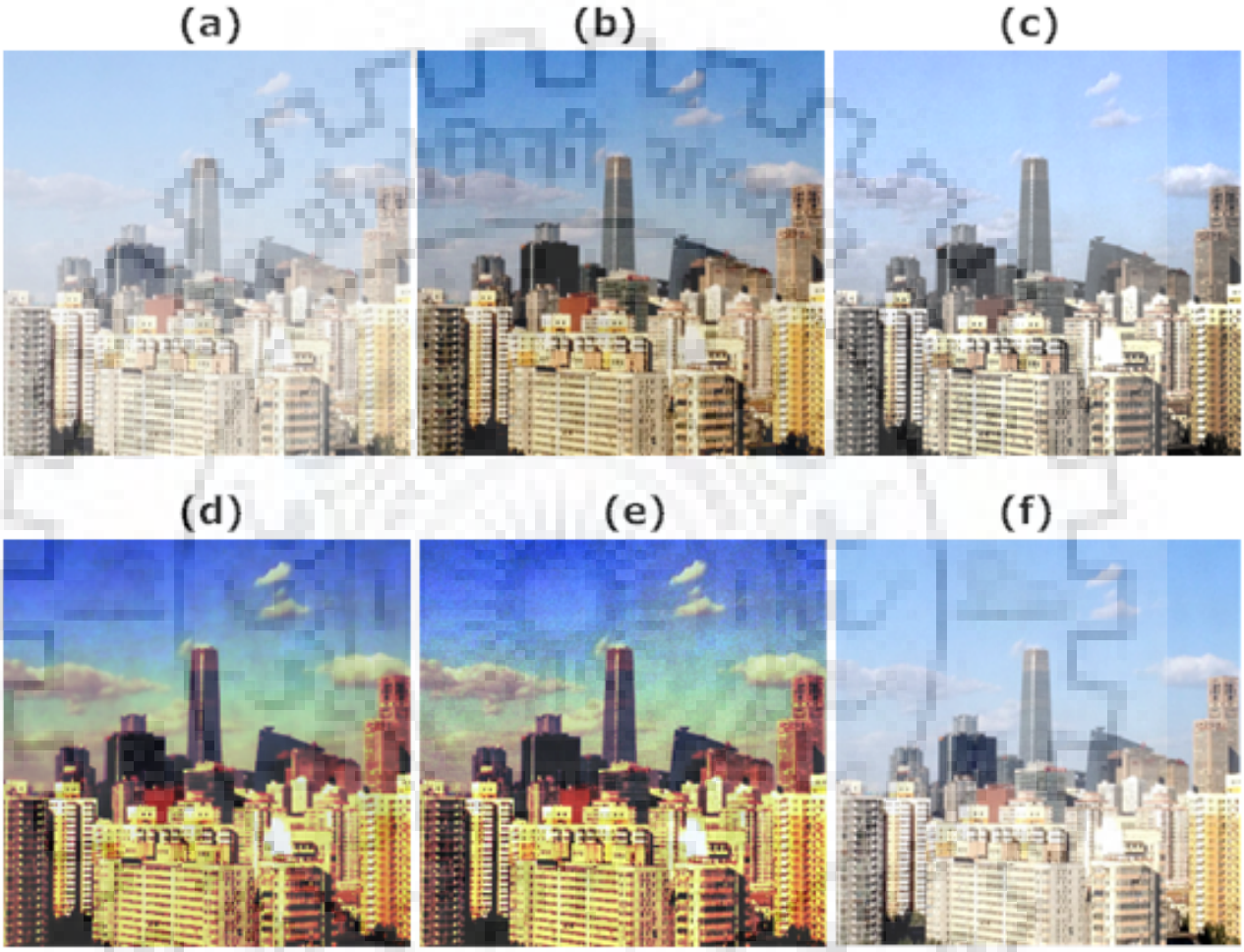

Figure 6.9: Comparison of the filtering method results for the building image: (a) Building hazy image; (b) DCP based scheme [58]; (c) FrADP based scheme; (d) Adaptive and anisotropic filtering (AAF) based scheme [142]; (e) the proposed algorithm; (f) ground truth image.

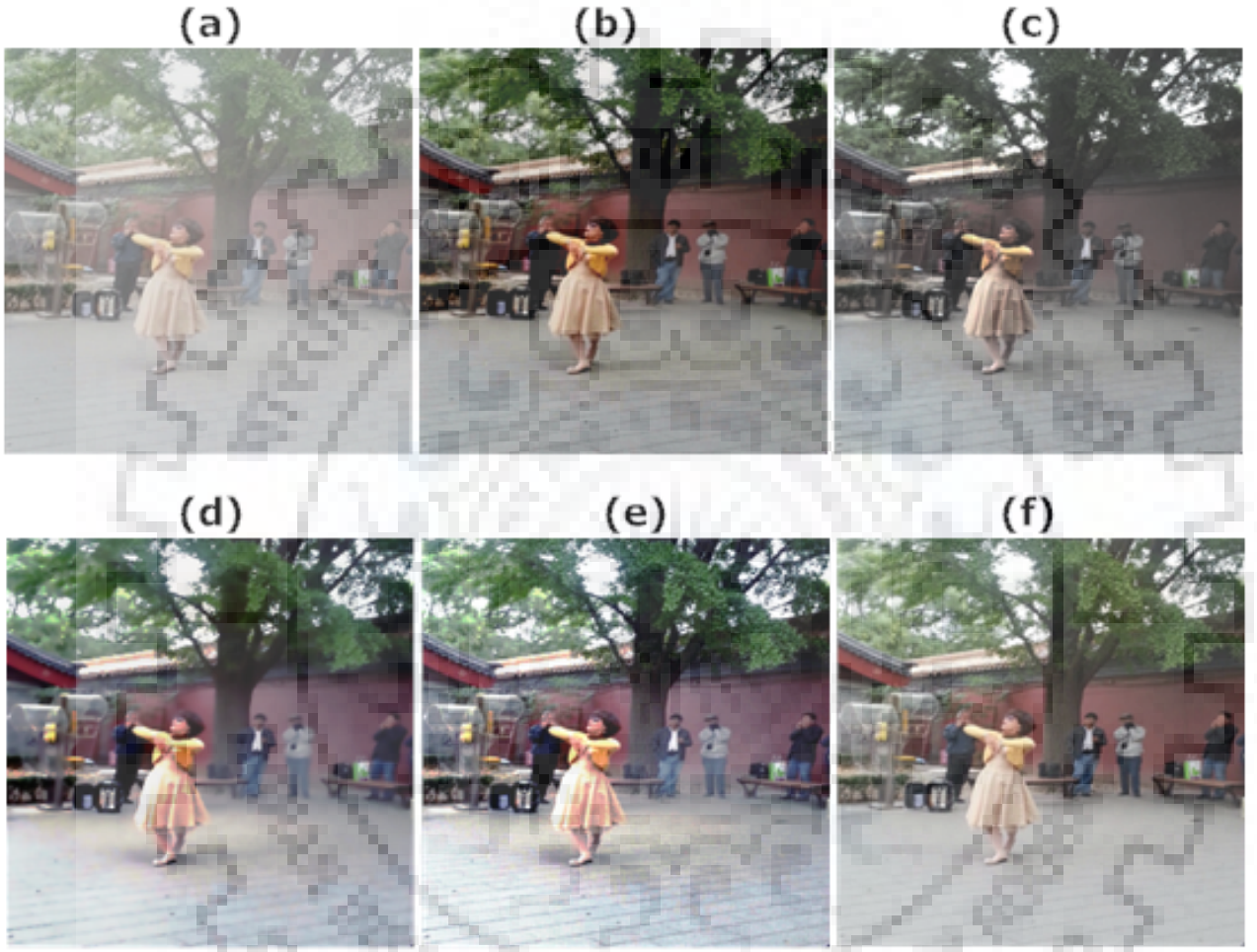

Figure 6.10: Comparison of the filtering method results for the lady image: (a) Lady hazy image; (b) DCP based scheme [58]; (c) FrADP based scheme; (d) Adaptive and anisotropic filtering (AAF) based scheme [142]; (e) the proposed algorithm; (f) ground truth image.

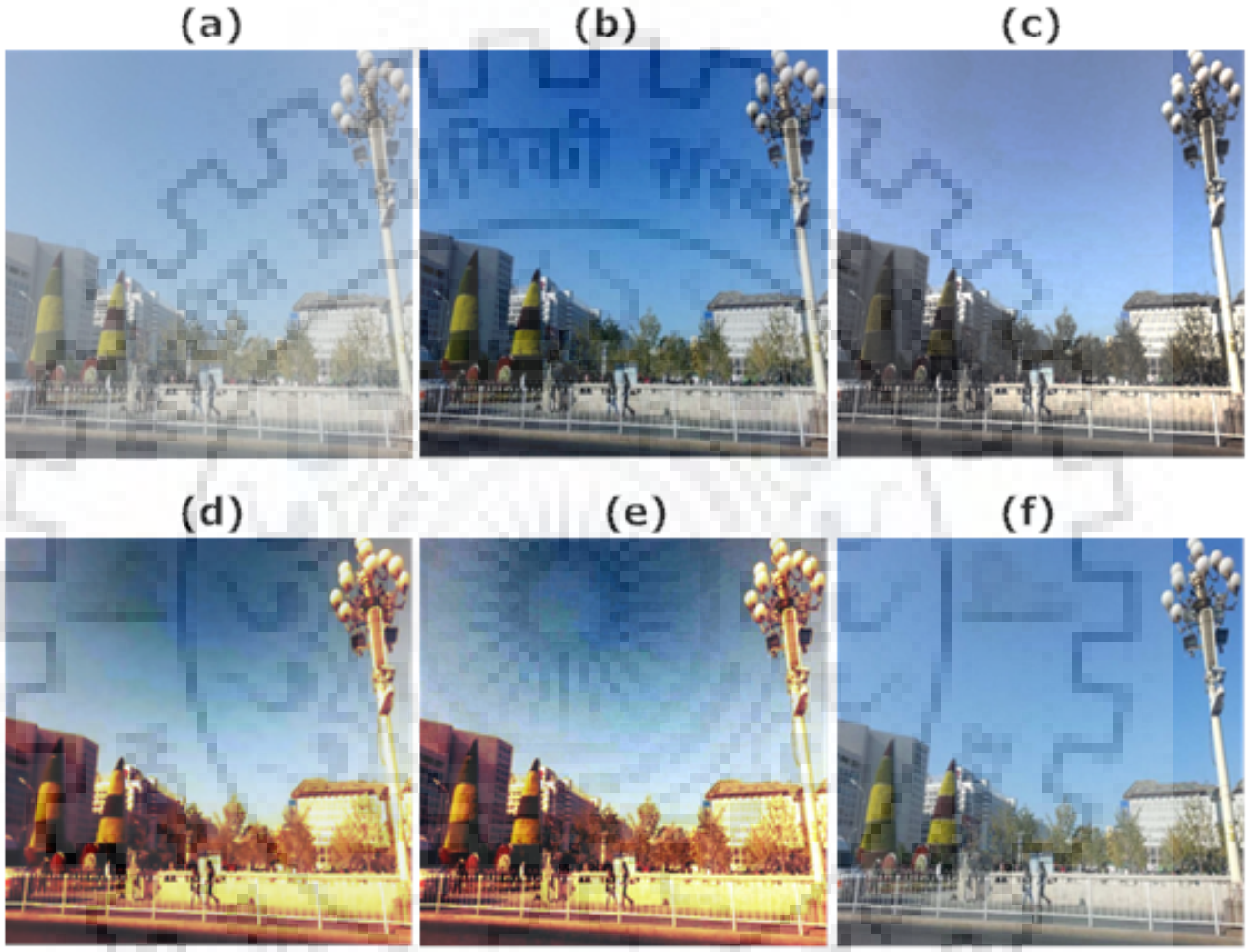

Figure 6.11: Comparison of the filtering method results for the light image: (a) Light hazy image; (b) DCP based scheme [58]; (c) FrADP based scheme; (d) Adaptive and anisotropic filtering (AAF) based scheme [142]; (e) the proposed algorithm; (f) ground truth image.

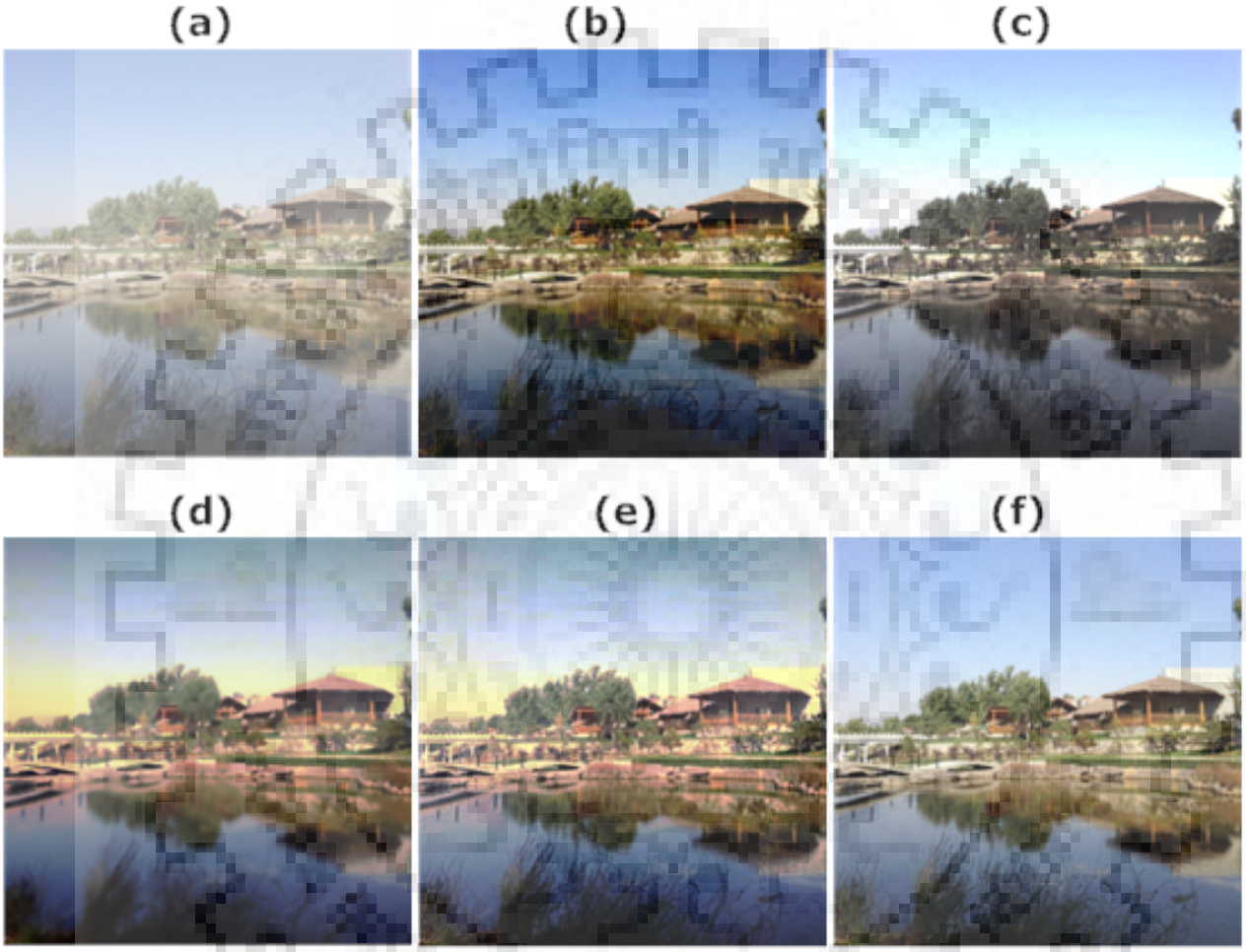

Figure 6.12: Comparison of the filtering method results for the pond image: (a) Pond hazy image; (b) DCP based scheme [58]; (c) FrADP based scheme; (d) Adaptive and anisotropic filtering (AAF) based scheme [142]; (e) the proposed algorithm; (f) ground truth image.

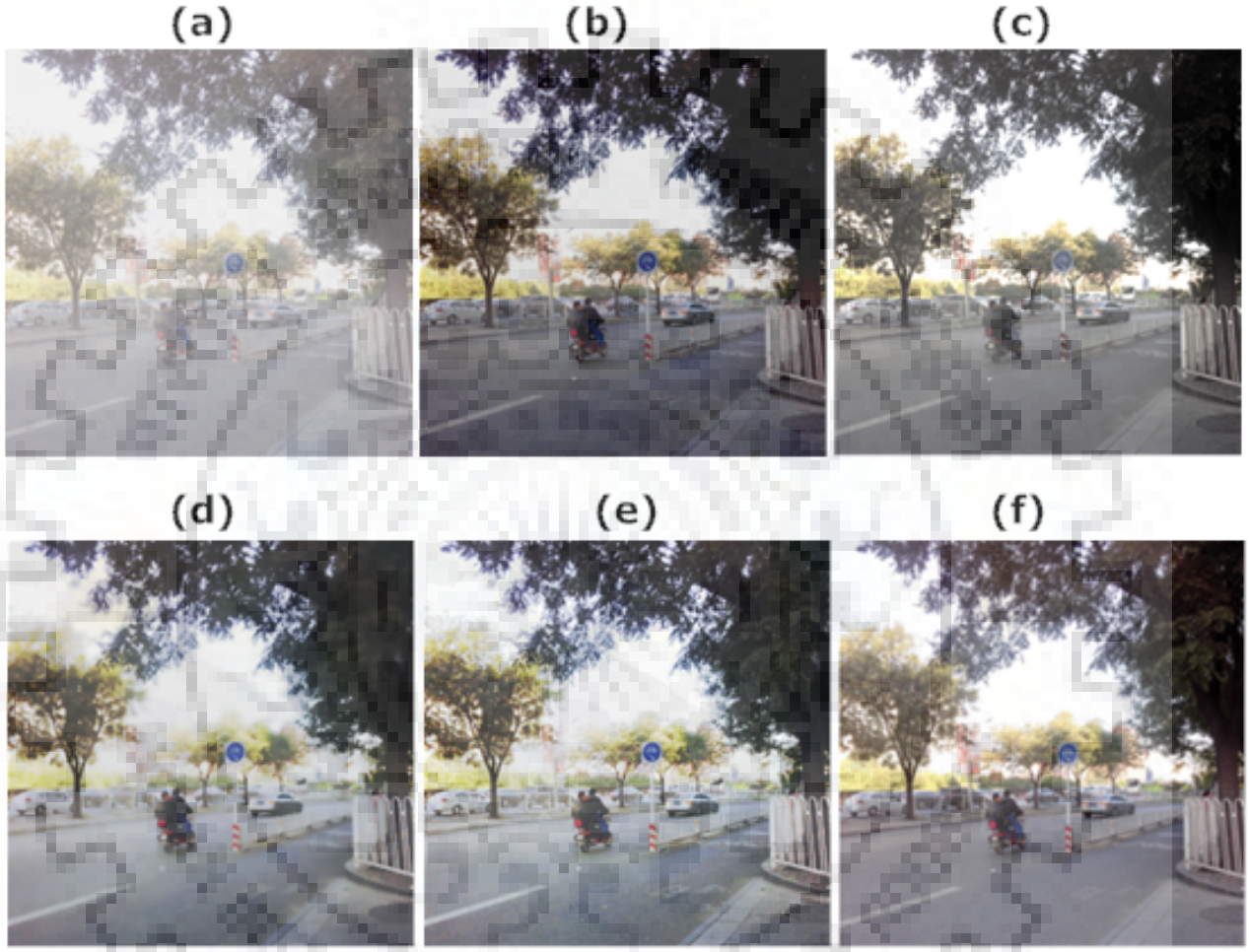

Figure 6.13: Comparison of the filtering method results for the street image: (a) Street hazy image; (b) DCP based scheme [58]; (c) FrADP based scheme; (d) Adaptive and anisotropic filtering (AAF) based scheme [142]; (e) the proposed algorithm; (f) ground truth image.

Chapter 7

Conclusions and future scope

7.1 Conclusions

This thesis introduced certain algorithms for image restoration using fractional-order anisotropic diffusion to solve the image defogging/dehazing and image denoising problems. A total of five different algorithms have been introduced based on the diffusion PDEs and the wavelet transform.

- The first algorithm addressed the issue of defogging of the digital images by using a fractional-order generalization of the anisotropic diffusion PDE in the Cartesian space of the image. The quality of restored images in the proposed algorithm depends on the diffused airlight map. The proposed algorithm diffused the airlight map visually better when compared to classical anisotropic diffusion. The computation of the fractional-order derivatives in the proposed algorithm utilizes lower computational resources when compared to a Fourier domain-based implementation and restores images better.

- The second algorithm is an extension of first algorithm where a cross channel regularization term is included in the 'p-Laplace' based anisotropic diffusion PDE. Again this PDE is having fractional-order derivatives in image space. The efficiency of the proposed algorithm was tested on the benchmark data set 'SOTS' containing synthetic hazy images and naturally hazed outdoor

images. Convergence analysis has been given for both first and second algorithms.

- The third algorithm is based on removal of noise from the images in the fractional quaternion wavelet transform domain (FrQWT). The choice of hard or semi-soft thresholding depends on the image. In a few of the images, the semi-soft threshold performs marginally better than the hard threshold. However, in a few cases, it was found that the choice of hard threshold is better.

- The next algorithm is directions adaptive fractional-order anisotropic diffusion method developed using the wavelet transform, preserves the edges of the restored images in a better way. Moreover, fractional derivatives based convolution filter implemented in the wavelet subspaces of the image are easy to implement and also numerically efficient.

- The last algorithm proposes a 'tansig' function based diffusion scheme which provides impressive restored images with faster convergence. This method is found quite effective in dehazing as well as in denoising. Also, no blurring artifact is noticed in the recovered images.

7.2 Future directions

The work presented in this thesis can be extended in some more directions. In this section, these potential directions are listed briefly.

- The proposed algorithms considers the fixed values of the fractional order in range $[1, 2)$. This fractional order can be chosen in an adaptive way depending on the local image statistics.

- Data-driven or learnable PDEs can be developed to circumvent the manually designing issue of fractional order and give the new life for PDEs based methods in restoration (including denoising, deblurring and dehazing).

- In second and third chapters of this thesis, the widely-used atmospheric scattering model is used to show the fog-effect. In addition to this, there are other degradation models such as the dual-color atmospheric scattering model and the ATF (atmospheric transfer function) model.

Therefore, a fast and optimized method can be explored that uses multi scale information fusion technology and machine learning technology.

- In the fourth chapter of the thesis, the value of hard and soft thresholding parameter is based on a hit and trial way. In this thesis, the fixed values of thresholding values are taken for different images. This parameter value can be made adaptive to have a more accurate image filtering and to preserve the image details. A control parameter sensitivity of hard threshold can be included for better qualitative and quantitative improvement in recovered images.

Bibliography

[1] Agarwal, H., Atrey, P.K. and Raman, B., 2015. Image watermarking in real oriented wavelet transform domain. Multimedia Tools and Applications, 74(23), pp.10883–10921.

[2] Ahn, B. and Cho, N.I., 2017. Block-matching convolutional neural network for image denoising. arXiv preprint arXiv:1704.00524.

[3] Amoako-Yirenkyi, P., Appati, J.K. and Dontwi, I.K., 2016. A new construction of a fractional derivative mask for image edge analysis based on Riemann-Liouville fractional derivative. Advances in Difference Equations, 2016(1), p.238.

[4] Androutsos, D., Plataniotis, K.N. and Venetsanopoulos, A.N., 1999. A novel vector-based approach to color image retrieval using a vector angular-based distance measure. Computer Vision and Image Understanding, 75(1–2), pp.46–58.

[5] Anwar, M.I. and Khosla, A., 2017. Vision enhancement through single image fog removal. Engineering science and technology, an international journal, 20(3), pp.1075–1083.

[6] Arora, S., Bhaskara, A., Ge, R. and Ma, T., 2014, January. Provable bounds for learning some deep representations. In International Conference on Machine Learning (pp. 584–592).

[7] Asari, K.V., Kumar, S. and Radhakrishnan, D., 1999. A new approach for nonlinear distortion correction in endoscopic images based on least squares estimation. IEEE Transactions on Medical Imaging, 18(4), pp.345–354.

[8] Aziz, I. and arler, B., 2013. Wavelets collocation methods for the numerical solution of elliptic BV problems. Applied Mathematical Modelling, 37(3), pp.676–694.

[9] Bai, J. and Feng, X.C., 2007. Fractional-order anisotropic diffusion for image denoising. IEEE transactions on image processing, 16(10), pp.2492–2502.

[10] Bako, S., Vogels, T., McWilliams, B., Meyer, M., Novk, J., Harvill, A., Sen, P., Derose, T. and Rousselle, F., 2017. Kernel-predicting convolutional networks for denoising Monte Carlo renderings. ACM Transactions on Graphics (TOG), 36(4), p.97.

[11] Balakumar, V. and Murugesan, K., 2012, March. A Numerical Method for a Class of Linear Fractional Differential Equations. In International Conference on Mathematical Modelling and Scientific Computation (pp. 360–366). Springer, Berlin, Heidelberg.

[12] Baraniuk, R.G., Kingsbury, N. and Selesnick, I.W., 2005. The dual-tree complex wavelet transform-a coherent framework for multiscale signal and image processing. IEEE Signal Processing Magazine, 22(6), pp.123–151.

[13] Baraniuk, R.G., 1999, October. Optimal tree approximation with wavelets. In Wavelet Applications in Signal and Image Processing VII (Vol. 3813, pp. 196–207). International Society for Optics and Photonics.

[14] Bengio, Y., Simard, P. and Frasconi, P., 1994. Learning long-term dependencies with gradient descent is difficult. IEEE transactions on neural networks, 5(2), pp.157–166.

[15] Bhateja, V., Singh, G., Srivastava, A. and Singh, J., 2014, March. Speckle reduction in ultrasound images using an improved conductance function based on anisotropic diffusion. In 2014 International Conference on Computing for Sustainable Global Development (INDIACom) (pp. 619–624). IEEE.

[16] Bhugra, S., Mishra, D., Anupama, A., Chaudhury, S., Lall, B., Chugh, A. and Chinnusamy, V., 2018. Deep Convolutional Neural Networks Based Framework for Estimation of Stomata Density

and Structure from Microscopic Images. In Proceedings of the European Conference on Computer Vision (ECCV) (pp. 0–0).

[17] Bigun, J., 1987. Optimal orientation detection of linear symmetry.

[18] Black, M.J., Sapiro, G., Marimont, D.H. and Heeger, D., 1998. Robust anisotropic diffusion. IEEE Transactions on image processing, 7(3), pp.421–432.

[19] Brox, T., Weickert, J., Burgeth, B. and Mrzek, P., 2006. Nonlinear structure tensors. Image and Vision Computing, 24(1), pp.41–55.

[20] Bulow, T., 1999. Hypercomplex spectral signal representations for the processing and analysis of images. Ph. D thesis, Christian-Albrechts-Universitat zu Kiel.

[21] Burns, T.J., Rogers, S.K., Oxley, M.E. and Ruck, D.W., 1996. A wavelet multiresolution analysis for spatio-temporal signals. IEEE Transactions on Aerospace and Electronic Systems, 32(2), pp.628–649.

[22] Catte, F., Lions, P.L., Morel, J.M. and Coll, T., 1992. Image selective smoothing and edge detection by nonlinear diffusion. SIAM Journal on Numerical analysis, 29(1), pp.182–193.

[23] Chakraborty, M., Maiti, D., Konar, A. and Janarthanan, R., 2008, December. A study of the grunwald-letnikov definition for minimizing the effects of random noise on fractional order differential equations. In 2008 4th International Conference on Information and Automation for Sustainability (pp. 449–456). IEEE.

[24] Chan, W.L., Choi, H. and Baraniuk, R.G., 2006. Coherent multiscale image processing using quaternion wavelets. IEEE Transactions on Image Processing.

[25] Chan, W.L., Choi, H. and Baraniuk, R.G., 2004, October. Quaternion wavelets for image analysis and processing. In IEEE International Conference on Image Processing (Vol. 5, pp. 3057–3060).

[26] Chan, W.L., Choi, H. and Baraniuk, R.G., 2008. Coherent multiscale image processing using dual-tree quaternion wavelets. IEEE Transactions on Image Processing, 17(7), pp.1069-1082.

[27] Chan, R.H., Lanza, A., Morigi, S. and Sgallari, F., 2013. An adaptive strategy for the restoration of textured images using fractional order regularization. Numerical Mathematics: Theory, Methods and Applications, 6(1), pp.276–296.

[28] Chang, S.G., Yu, B. and Vetterli, M., 2000. Spatially adaptive wavelet thresholding with context modeling for image denoising. IEEE Transactions on image Processing, 9(9), pp.1522–1531.

[29] Chen, J. and Guo, J., 2010, October. Image restoration based on adaptive P-Laplace diffusion. In 2010 3rd International Congress on Image and Signal Processing (Vol. 1, pp. 143–146). IEEE.

[30] Chen, Y. and Pock, T., 2016. Trainable nonlinear reaction diffusion: A flexible framework for fast and effective image restoration. IEEE transactions on pattern analysis and machine intelligence, 39(6), pp.1256–1272.

[31] Cheng, G., Han, J., Guo, L., Qian, X., Zhou, P., Yao, X. and Hu, X., 2013. Object detection in remote sensing imagery using a discriminatively trained mixture model. ISPRS Journal of Photogrammetry and Remote Sensing, 85, pp.32–43.

[32] Chipman, H.A., Kolaczyk, E.D. and McCulloch, R.E., 1997. Adaptive Bayesian wavelet shrinkage. Journal of the American Statistical Association, 92(440), pp.1413–1421.

[33] Coifman, R.R. and Donoho, D.L., 1995. Translation-invariant de-noising. In Wavelets and statistics (pp. 125–150). Springer, New York, NY.

[34] Cuesta, E., Kirane, M. and Malik, S.A., 2012. Image structure preserving denoising using generalized fractional time integrals. Signal Processing, 92(2), pp.553–563.

[35] Daubechies, I., 1992. Ten lectures on wavelets (Vol. 61). Siam.

[36] Dobrosotskaya, J.A. and Bertozzi, A.L., 2008. A wavelet-Laplace variational technique for image deconvolution and inpainting. IEEE Transactions on Image Processing, 17(5), pp.657–663.

[37] De, S., Bhattacharyya, S., Dutta, P., Intelligent Multidimensional Data and Image Processing, IGI Global, ISBN10: 1522552464, 2018.

[38] Donoho, D.L., 1997. CART and best-ortho-basis: a connection. The Annals of Statistics, 25(5), pp.1870–1911.

[39] Donoho, D.L., 1995. De-noising by soft-thresholding. IEEE transactions on information theory, 41(3), pp.613–627.

[40] Donoho, D.L. and Johnstone, I.M., 1995. Adapting to unknown smoothness via wavelet shrinkage. Journal of the american statistical association, 90(432), pp.1200–1224.

[41] Donoho, D.L. and Johnstone, J.M., 1994. Ideal spatial adaptation by wavelet shrinkage. biometrika, 81(3), pp.425–455.

[42] Elango, P. and Murugesan, K., 2009. Digital image inpainting using cellular neural network. Int. J. Open Problems Compt. Math, 2(3), pp.439–450.

[43] Esser, P., Sutter, E. and Ommer, B., 2018. A variational u-net for conditional appearance and shape generation. In Proceedings of the IEEE Conference on Computer Vision and Pattern Recognition (pp. 8857–8866).

[44] Fan, X., Wang, Y., Tang, X., Gao, R. and Luo, Z., 2016. Two-layer Gaussian process regression with example selection for image dehazing. IEEE Transactions on Circuits and Systems for Video Technology, 27(12), pp.2505–2517.

[45] Fattal, R., 2008. Single image dehazing. ACM transactions on graphics (TOG), 27(3), p.72.

[46] Fodor, I.K. and Kamath, C., 2003. Denoising through wavelet shrinkage: an empirical study. Journal of Electronic Imaging, 12(1), pp.151–161.

[47] Foresti, G.L., Micheloni, C., Snidaro, L., Remagnino, P. and Ellis, T., 2005. Active video-based surveillance system: the low-level image and video processing techniques needed for implementation. IEEE Signal Processing Magazine, 22(2), pp.25–37.

[48] Forstner, W. and Gulch, E., 1987, June. A fast operator for detection and precise location of distinct points, corners and centres of circular features. In Proc. ISPRS intercommission conference on fast processing of photogrammetric data (pp. 281–305).

[49] Gangapure, V.N., Banerjee, S. and Chowdhury, A.S., 2015. Steerable local frequency based multispectral multifocus image fusion. Information fusion, 23, pp.99–115.

[50] Gibson, K.B., Vo, D.T. and Nguyen, T.Q., 2011. An investigation of dehazing effects on image and video coding. IEEE transactions on image processing, 21(2), pp.662–673.

[51] Gonzalez, R.C. and Wintz, P., 1977. Digital image processing(Book). Reading, Mass., Addison-Wesley Publishing Co., Inc.(Applied Mathematics and Computation, (13), p.451.

[52] Gosta H.. Granlund and Knutsson, H., 1995. Signal processing for computer vision. Dordrecht: Kluwer Academic Publishers.

[53] Graps, A., 1995. An introduction to wavelets. IEEE computational science and engineering, 2(2), pp.50–61.

[54] Hamza, A.B., Luque-Escamilla, P.L., Martnez-Aroza, J. and Romn-Roldn, R., 1999. Removing noise and preserving details with relaxed median filters. Journal of Mathematical Imaging and Vision, 11(2), pp.161–177.

[55] Han, J., Zhang, D., Cheng, G., Guo, L. and Ren, J., 2014. Object detection in optical remote sensing images based on weakly supervised learning and high-level feature learning. IEEE Transactions on Geoscience and Remote Sensing, 53(6), pp.3325–3337.

[56] Hardie, R.C. and Barner, K.E., 1994. Rank conditioned rank selection filters for signal restoration. IEEE Transactions on Image Processing, 3(2), pp.192–206.

[57] He, K., Sun, J. and Tang, X., 2012. Guided image filtering. IEEE transactions on pattern analysis and machine intelligence, 35(6), pp.1397–1409.

[58] He, K., Sun, J. and Tang, X., 2010. Single image haze removal using dark channel prior. IEEE transactions on pattern analysis and machine intelligence, 33(12), pp.2341–2353.

[59] He, K., Zhang, X., Ren, S. and Sun, J., 2016. Deep residual learning for image recognition. In Proceedings of the IEEE conference on computer vision and pattern recognition (pp. 770–778).

[60] Heydari, M.H., Hooshmandasl, M.R. and Mohammadi, F., 2014. Legendre wavelets method for solving fractional partial differential equations with Dirichlet boundary conditions. Applied Mathematics and Computation, 234, pp.267–276.

[61] Hosotani, F., Inuzuka, Y., Hasegawa, M., Hirobayashi, S. and Misawa, T., 2015. Image denoising with edge-preserving and segmentation based on mask NHA. IEEE transactions on image processing, 24(12), pp.6025–6033.

[62] Hou, Q., Cheng, M.M., Hu, X., Borji, A., Tu, Z. and Torr, P.H., 2017. Deeply supervised salient object detection with short connections. In Proceedings of the IEEE Conference on Computer Vision and Pattern Recognition (pp. 3203–3212).

[63] Huang, Y. and Guan, Y., 2016. Laplacian hashing for fast large-scale image retrieval and its applications for midway processing in a cascaded face detection structure. Multimedia Tools and Applications, 75(23), pp.16315–16332.

[64] Hyvarinen, A., Oja, E., Hoyer, P. and Hurri, J., 1998, August. Image feature extraction by sparse coding and independent component analysis. In Proceedings. Fourteenth International Conference on Pattern Recognition (Cat. No. 98EX170) (Vol. 2, pp. 1268–1273). IEEE.

[65] Jafari, H., Yousefi, S.A., Firoozjaee, M.A., Momani, S. and Khalique, C.M., 2011. Application of Legendre wavelets for solving fractional differential equations. Computers & Mathematics with Applications, 62(3), pp.1038–1045.

[66] Jain, A.K., 1989. Fundamentals of digital image processing. Englewood Cliffs, NJ: Prentice Hall,.

[67] Jain, S.K. and Ray, R.K., 2015. A Non-linear Diffusion Based Partial Differential Equation Model for Noise Reduction in Images. In Information Systems Design and Intelligent Applications (pp. 429–438). Springer, New Delhi.

[68] Jain, S.K. and Ray, R.K., 2016, March. An alternative framework of anisotropic diffusion for image denoising. In Proceedings of the Second International Conference on Information and Communication Technology for Competitive Strategies (p. 46). ACM.

[69] Jain, S.K., Ray, R.K. and Bhavsar, A., 2015. Iterative solvers for image denoising with diffusion models: A comparative study. Computers & Mathematics with Applications, 70(3), pp.191–211.

[70] Janev, M., Pilipovic, S., Atanackovic, T., Obradovic, R. and Ralevic, N., 2011. Fully fractional anisotropic diffusion for image denoising. Mathematical and Computer Modelling, 54(1–2), pp.729–741.

[71] Jansen, M., 2001. Noise reduction by wavelet thresholding.-Lecture notes in statistics ser.

[72] Jiang, H., Lu, N. and Yao, L., 2016. A high-fidelity haze removal method based on hot for visible remote sensing images. Remote Sensing, 8(10), p.844.

[73] Jun, Z. and Zhihui, W., 2011. A class of fractional-order multi-scale variational models and alternating projection algorithm for image denoising. Applied Mathematical Modelling, 35(5), pp.2516–2528.

[74] Jung, A., 2001, October. An introduction to a new data analysis tool: Independent component analysis. In Proceedings of Workshop GK" Nonlinearity"-Regensburg.

[75] Kadiri, M., Djebbouri, M. and Carr, P., 2014. Magnitude-phase of the dual-tree quaternionic wavelet transform for multispectral satellite image denoising. EURASIP Journal on image and video processing, 2014(1), p.41.

[76] Kamalaveni, V., Veni, S. and Narayanankutty, K.A., 2017. Improved self-snake based anisotropic diffusion model for edge preserving image denoising using structure tensor. Multimedia Tools and Applications, 76(18), pp.18815–18846.

[77] Kandi, H., Mishra, D. and Gorthi, S.R.S., 2017. Exploring the learning capabilities of convolutional neural networks for robust image watermarking. Computers & Security, 65, pp.247–268.

[78] Kansal, K., Mohanty, M. and Atrey, P.K., 2015, January. Scaling and cropping of wavelet-based compressed images in hidden domain. In International Conference on Multimedia Modeling (pp. 430–441). Springer, Cham.

[79] Karasulu, B. and Korukoglu, S., 2011. A software for performance evaluation and comparison of people detection and tracking methods in video processing. Multimedia Tools and Applications, 55(3), pp.677–723.

[80] Kermani, E. and Asemani, D., 2014. A robust adaptive algorithm of moving object detection for video surveillance. Eurasip Journal on Image and video processing, 2014(1), p.27.

[81] Kim, T.K., Paik, J.K. and Kang, B.S., 1998. Contrast enhancement system using spatially adaptive histogram equalization with temporal filtering. IEEE Transactions on Consumer Electronics, 44(1), pp.82–87.

[82] Kingsbury, N., 2000, September. A dual-tree complex wavelet transform with improved orthogonality and symmetry properties. In Proceedings 2000 International Conference on Image Processing (Cat. No. 00CH37101) (Vol. 2, pp. 375–378). IEEE.

[83] Kingsbury, N., 1999. Image processing with complex wavelets. Philosophical Transactions of the Royal Society of London. Series A: Mathematical, Physical and Engineering Sciences, 357(1760), pp.2543–2560.

[84] Kingsbury, N., 1998, September. The dual-tree complex wavelet transform: a new efficient tool for image restoration and enhancement. In 9th European Signal Processing Conference (EUSIPCO 1998) (pp. 1–4). IEEE.

[85] Kristaly, A., Lisei, H. and Varga, C., 2008. Multiple solutions for p-Laplacian type equations. Nonlinear Analysis: Theory, Methods & Applications, 68(5), pp.1375–1381.

[86] Krizhevsky, A., Sutskever, I. and Hinton, G.E., 2012. Imagenet classification with deep convolutional neural networks. In Advances in neural information processing systems (pp. 1097–1105).

[87] Kumar, S., Kumar, S., Sukavanam, N. and Raman, B., 2014. Dual tree fractional quaternion wavelet transform for disparity estimation. ISA transactions, 53(2), pp.547–559.

[88] Kumar, S., Micheloni, C., Piciarelli, C. and Foresti, G.L., 2010. Stereo rectification of uncalibrated and heterogeneous images. Pattern Recognition Letters, 31(11), pp.1445–1452.

[89] Langari, B., Vaseghi, S., Prochazka, A., Vaziri, B. and Aria, F.T., 2016. Edge-guided image gap interpolation using multi-scale transformation. IEEE Transactions on Image Processing, 25(9), pp.4394-4405.

[90] Lathey, A. and Atrey, P.K., 2015. Image enhancement in encrypted domain over cloud. ACM Transactions on Multimedia Computing, Communications, and Applications (TOMM), 11(3), p.38.

[91] Lawrence, S., Giles, C.L., Tsoi, A.C. and Back, A.D., 1997. Face recognition: A convolutional neural-network approach. IEEE transactions on neural networks, 8(1), pp.98–113.

[92] Levin, A., Lischinski, D. and Weiss, Y., 2007. A closed-form solution to natural image matting. IEEE transactions on pattern analysis and machine intelligence, 30(2), pp.228–242.

[93] Li, B., Ren, W., Fu, D., Tao, D., Feng, D., Zeng, W. and Wang, Z., 2018. Benchmarking single-image dehazing and beyond. IEEE Transactions on Image Processing, 28(1), pp.492–505.

[94] Li, C., Qian, D. and Chen, Y., 2011. On riemann-liouville and caputo derivatives. Discrete Dynamics in Nature and Society, 2011.

[95] Li, S., Li, W., Cook, C., Zhu, C. and Gao, Y., 2018. Independently recurrent neural network (indrnn): Building a longer and deeper rnn. In Proceedings of the IEEE Conference on Computer Vision and Pattern Recognition (pp. 5457–5466).

[96] Li, X. and Chen, T., 1994. Nonlinear diffusion with multiple edginess thresholds. Pattern Recognition, 27(8), pp.1029–1037.

[97] Lina, J.M., 1998. Complex daubechies wavelets: Filters design and applications. In Inverse Problems, Tomography, and Image Processing (pp. 95–112). Springer, Boston, MA.

[98] Lindqvist, P., 2006. Notes on the p-Laplace equation, Report. University of Jyvskyl Department of Mathematics and Statistics, 102.

[99] Liu, R., Zhong, G., Cao, J., Lin, Z., Shan, S. and Luo, Z., 2016. Learning to diffuse: A new perspective to design pdes for visual analysis. IEEE transactions on pattern analysis and machine intelligence, 38(12), pp.2457–2471.

[100] Liu, R., Fan, X., Hou, M., Jiang, Z., Luo, Z. and Zhang, L., 2018. Learning aggregated transmission propagation networks for haze removal and beyond. IEEE transactions on neural networks and learning systems.

[101] Lu, J., Weaver, J.B., Healy, D.M. and Xu, Y., 1992, October. Noise reduction with a multiscale

edge representation and perceptual criteria. In [1992] Proceedings of the IEEE-SP International Symposium on Time-Frequency and Time-Scale Analysis (pp. 555–558). IEEE.

[102] Ma, Z., Wen, J., Zhang, C., Liu, Q. and Yan, D., 2016. An effective fusion defogging approach for single sea fog image. Neurocomputing, 173, pp.1257–1267.

[103] Malfait, M. and Roose, D., 1997. Wavelet-based image denoising using a Markov random field a priori model. IEEE Transactions on image processing, 6(4), pp.549–565.

[104] Mallat, S.G., 1989. A theory for multiresolution signal decomposition: the wavelet representation. IEEE Transactions on Pattern Analysis & Machine Intelligence, (7), pp.674–693.

[105] Mathew, A. and Asari, V.K., 2012, August. Local histogram based descriptor for tracking in wide area imagery. In International Conference on Information Processing (pp. 119–128). Springer, Berlin, Heidelberg.

[106] Micheloni, C. and Foresti, G.L., 2006. Real-time image processing for active monitoring of wide areas. Journal of Visual Communication and Image Representation, 17(3), pp.589–604.

[107] Miller, K.S. and Ross, B., 1993. An introduction to the fractional calculus and fractional differential equations. Wiley.

[108] Mojzis, F., Svihlik, J., Fliegel, K., Knazovicka, L. and Jerhotova, E., 2012. Measurement and Analysis of Real Imaging Systems. Radioengineering, 21(1).

[109] Mukherjee, A., Chakraborty, S., Sil, J. and Chowdhury, A.S., 2017. A novel visual word assignment model for Content-Based Image Retrieval. In Proceedings of International Conference on Computer Vision and Image Processing (pp. 79-87). Springer, Singapore.

[110] Mukherjee, A., Sil, J. and Chowdhury, A.S., 2018. Image Retrieval Using Random Forest-Based Semantic Similarity Measures and SURF-Based Visual Words. In Proceedings of 2nd International Conference on Computer Vision & Image Processing (pp. 79–90). Springer, Singapore.

[111] Nandal, S. and Kumar, S., 2019. Single image fog removal algorithm in spatial domain using fractional order anisotropic diffusion. Multimedia Tools and Applications, 78(8), pp.10717–10732.

[112] Narasimhan, S.G. and Nayar, S.K., 2000, June. Chromatic framework for vision in bad weather. In Proceedings IEEE Conference on Computer Vision and Pattern Recognition. CVPR 2000 (Cat. No. PR00662) (Vol. 1, pp. 598–605). IEEE.

[113] Neretti, N., Huynh, Q., Intrator, N. and Dobeck, G., 1998, April. Image Enhancement and Feature Extraction for Pattern Recognition. In Proceedings of SPIE'9 (Vol. 3392, pp. 306–315).

[114] Nnolim, U.A., 2018. Partial differential equation-based hazy image contrast enhancement. Computers & Electrical Engineering, 72, pp.670–681.

[115] Ozaki, M., Kakimuma, K., Hashimoto, M. and Takahashi, K., 2012. Laser-based pedestrian tracking in outdoor environments by multiple mobile robots. Sensors, 12(11), pp.14489–14507.

[116] Pandey, S. and Khanna, P., 2016. Content-based image retrieval embedded with agglomerative clustering built on information loss. Computers & Electrical Engineering, 54, pp.506–521.

[117] Perona, P. and Malik, J., 1990. Scale-space and edge detection using anisotropic diffusion. IEEE Transactions on pattern analysis and machine intelligence, 12(7), pp.629–639.

[118] Pu, Y., Wang, W., Zhou, J., Wang, Y. and Jia, H., 2008. Fractional differential approach to detecting textural features of digital image and its fractional differential filter implementation. Science in China Series F: Information Sciences, 51(9), pp.1319–1339.

[119] Pu, Y.F., Zhou, J.L. and Yuan, X., 2009. Fractional differential mask: a fractional differential-based approach for multiscale texture enhancement. IEEE transactions on image processing, 19(2), pp.491–511.

[120] Rahimkhani, P. and Ordokhani, Y., 2019. A numerical scheme based on Bernoulli wavelets and

collocation method for solving fractional partial differential equations with Dirichlet boundary conditions. Numerical Methods for Partial Differential Equations, 35(1), pp.34–59.

[121] Rahimkhani, P., Ordokhani, Y. and Babolian, E., 2017. A new operational matrix based on Bernoulli wavelets for solving fractional delay differential equations. Numerical Algorithms, 74(1), pp.223–245.

[122] Romberg, J., Choi, H. and Baraniuk, R.G., 2001. Bayesian wavelet domain image modeling using hidden Markov models. IEEE Transactions on Image Processing, 10(7), pp.1056–1068.

[123] Rudin, L.I., Osher, S. and Fatemi, E., 1992. Nonlinear total variation based noise removal algorithms. Physica D: nonlinear phenomena, 60(1–4), pp.259–268.

[124] Saxena, S., Pandey, S. and Khanna, P., 2018. A semi-supervised domain adaptation assembling approach for image classification. Pattern Analysis and Applications, 21(3), pp.813–827.

[125] Schechner, Y.Y., Narasimhan, S.G. and Nayar, S.K., 2001, December. Instant dehazing of images using polarization. In CVPR (1) (pp. 325–332).

[126] Schechner, Y.Y., Narasimhan, S.G. and Nayar, S.K., 2003. Polarization-based vision through haze. Applied optics, 42(3), pp.511–525.

[127] Serikawa, S. and Lu, H., 2014. Underwater image dehazing using joint trilateral filter. Computers & Electrical Engineering, 40(1), pp.41–50.

[128] Sermanet, P., Eigen, D., Zhang, X., Mathieu, M., Fergus, R. and LeCun, Y., 2013. Overfeat: Integrated recognition, localization and detection using convolutional networks. arXiv preprint arXiv:1312.6229.

[129] Shen, J. and Castan, S., 1992. An optimal linear operator for step edge detection. CVGIP: Graphical models and image processing, 54(2), pp.112–133.

[130] Simoncelli, E.P. and Adelson, E.H., 1996, September. Noise removal via Bayesian wavelet coring. In Proceedings of 3rd IEEE International Conference on Image Processing (Vol. 1, pp. 379–382). IEEE.

[131] Simonyan, K. and Zisserman, A., 2014. Very deep convolutional networks for large-scale image recognition. arXiv preprint arXiv:1409.1556.

[132] Singh, D. and Kumar, V., 2018. A novel dehazing model for remote sensing images. Computers & Electrical Engineering, 69, pp.14–27.

[133] Singh, D. and Kumar, V., 2018. Comprehensive survey on haze removal techniques. Multimedia Tools and Applications, 77(8), pp.9595–9620.

[134] Singh, D. and Kumar, V., 2018. Comprehensive survey on haze removal techniques. Multimedia Tools and Applications, 77(8), pp.9595–9620.

[135] Surya Prasath, V.B. and Singh, A., 2010. Multispectral image denoising by well-posed anisotropic diffusion scheme with channel coupling. International Journal of Remote Sensing, 31(8), pp.2091–2099.

[136] Szegedy, C., Liu, W., Jia, Y., Sermanet, P., Reed, S., Anguelov, D., Erhan, D., Vanhoucke, V. and Rabinovich, A., 2015. Going deeper with convolutions. In Proceedings of the IEEE conference on computer vision and pattern recognition (pp. 1–9).

[137] Tan, R.T., 2008, June. Visibility in bad weather from a single image. In 2008 IEEE Conference on Computer Vision and Pattern Recognition (pp. 1–8). IEEE.

[138] Tao, L. and Asari, V.K., 2005, July. A robust image enhancement technique for improving image visual quality in shadowed scenes. In International Conference on Image and Video Retrieval (pp. 395–404). Springer, Berlin, Heidelberg.

[139] Tao, D., Tang, X., Li, X. and Wu, X., 2006. Asymmetric bagging and random subspace for support vector machines-based relevance feedback in image retrieval. IEEE Transactions on Pattern Analysis & Machine Intelligence, (7), pp.1088–1099.

[140] Tarel, J.P. and Hautiere, N., 2009, September. Fast visibility restoration from a single color or gray level image. In 2009 IEEE 12th International Conference on Computer Vision (pp. 2201–2208). IEEE.

[141] Tarel, J.P., Hautiere, N., Caraffa, L., Cord, A., Halmaoui, H. and Gruyer, D., 2012. Vision enhancement in homogeneous and heterogeneous fog.

[142] Tebini, S., Seddik, H. and Braiek, E.B., 2016. An advanced and adaptive mathematical function for an efficient anisotropic image filtering. Computers & Mathematics with Applications, 72(5), pp.1369–1385.

[143] Thakur, A. and Mishra, D., 2017, January. Hyper spectral image classification using multilayer perceptron neural network & functional link ANN. In 2017 7th International Conference on Cloud Computing, Data Science & Engineering-Confluence (pp. 639–642). IEEE.

[144] Tomasi, C. and Manduchi, R., 1998, January. Bilateral filtering for gray and color images. In Iccv (Vol. 98, No. 1, p. 2).

[145] Torkamani-Azar, F. and Tait, K.E., 1996. Image recovery using the anisotropic diffusion equation. IEEE Transactions on Image Processing, 5(11), pp.1573–1578.

[146] Tripathi, A.K. and Mukhopadhyay, S., 2012. Single image fog removal using anisotropic diffusion. IET image processing, 6(7), pp.966–975.

[147] Tripathi, S., Lipton, Z.C. and Nguyen, T.Q., 2018. Correction by projection: Denoising images with generative adversarial networks. arXiv preprint arXiv:1803.04477.

[148] Unser, M., 1999. Splines: A perfect fit for signal and image processing. IEEE Signal processing magazine, 16(ARTICLE), pp.22–38.

[149] Unser, M. and Blu, T., 2000. Fractional splines and wavelets. SIAM review, 42(1), pp.43–67.

[150] Weickert, J., 1998. Anisotropic diffusion in image processing (Vol. 1, pp. 59–60). Stuttgart: Teubner.

[151] Weickert, J., 1996. Theoretical foundations of anisotropic diffusion in image processing. In Theoretical foundations of computer vision (pp. 221–236). Springer, Vienna.

[152] Weickert, J., Feddern, C., Welk, M., Burgeth, B. and Brox, T., 2006. PDEs for tensor image processing. In Visualization and Processing of Tensor Fields (pp. 399–414). Springer, Berlin, Heidelberg.

[153] Weickert, J. and Scharr, H., 2002. A scheme for coherence-enhancing diffusion filtering with optimized rotation invariance. Journal of Visual Communication and Image Representation, 13(1-2), pp.103–118.

[154] Whitaker, R.T. and Pizer, S.M., 1993. A multi-scale approach to nonuniform diffusion. CVGIP: Image Understanding, 57(1), pp.99–110.

[155] Williams, B.M., Zhang, J. and Chen, K., 2016. A new image deconvolution method with fractional regularisation. Journal of Algorithms & Computational Technology, 10(4), pp.265–276.

[156] Witkin, A.P., 1987. Scale-space filtering. In Readings in Computer Vision (pp. 329–332). Morgan Kaufmann.

[157] Wu, Y. and He, K., 2018. Group normalization. In Proceedings of the European Conference on Computer Vision (ECCV) (pp. 3–19).

[158] Xie, C.H., Qiao, W.W., Liu, Z. and Ying, W.H., 2017. Single image dehazing using kernel regression model and dark channel prior. Signal, image and video processing, 11(4), pp.705–712.

[159] Xie, S., Girshick, R., Dollar, P., Tu, Z. and He, K., 2017. Aggregated residual transformations for deep neural networks. In Proceedings of the IEEE conference on computer vision and pattern recognition (pp. 1492–1500).

[160] Yadollahi, M., Prochzka, A., Kaparov, M. and Vyata, O., 2015. The use of combined illumination in segmentation of orthodontic bodies. Signal, Image and Video Processing, 9(1), pp.243–250.

[161] Yang, F., Chen, K., Yu, B. and Yan, Z., 2014. Image denoising using LLT model and iterated total variation refinement. Int J Numer Anal Model, 5, pp.255–268.

[162] Yang, R., Yin, L., Gabbouj, M., Astola, J. and Neuvo, Y., 1995. Optimal weighted median filtering under structural constraints. IEEE transactions on signal processing, 43(3), pp.591–604.

[163] Yang, Q., Chen, D., Zhao, T. and Chen, Y., 2016. Fractional calculus in image processing: a review. Fractional Calculus and Applied Analysis, 19(5), pp.1222–1249.

[164] Yin, M., Liu, W., Shui, J. and Wu, J., 2012. Quaternion wavelet analysis and application in image denoising. Mathematical problems in Engineering, 2012.

[165] Yin, X., Zhou, S. and Siddique, M.A., 2016. Fractional nonlinear anisotropic diffusion with p-Laplace variation method for image restoration. Multimedia Tools and Applications, 75(8), pp.4505–4526.

[166] You, Y.L. and Kaveh, M., 2000. Fourth-order partial differential equations for noise removal. IEEE Transactions on Image Processing, 9(10), pp.1723–1730.

[167] You, Y.L., Kaveh, M., Xu, W.Y. and Tannenbaum, A., 1994, November. Analysis and design of anisotropic diffusion for image processing. In Proceedings of 1st International Conference on Image Processing (Vol. 2, pp. 497–501). IEEE.

[168] Yu, J., Xiao, C. and Li, D., 2010, October. Physics-based fast single image fog removal. In IEEE 10th International Conference on Signal Processing Proceedings (pp. 1048–1052). IEEE.

[169] Zagoruyko, S. and Komodakis, N., 2017. Diracnets: Training very deep neural networks without skip-connections. arXiv preprint arXiv:1706.00388.

[170] Zhang, J. and Chen, K., 2015. A total fractional-order variation model for image restoration with nonhomogeneous boundary conditions and its numerical solution. SIAM Journal on Imaging Sciences, 8(4), pp.2487–2518.

[171] ZHANG, H.Y., Qi-Cong, P.E.N.G. and Yang-Dong, W.U., 2007. Wavelet inpainting based on p-Laplace operator. Acta automatica sinica, 33(5), pp.546–549.

[172] Zhang, Y., Pu, Y.F., Hu, J.R. and Zhou, J.L., 2012. A class of fractional-order variational image inpainting models. Appl. Math. Inf. Sci, 6(2), pp.299–306.

[173] Zhang, Y., Tian, Y., Kong, Y., Zhong, B. and Fu, Y., 2018. Residual dense network for image super-resolution. In Proceedings of the IEEE Conference on Computer Vision and Pattern Recognition (pp. 2472–2481).

[174] Zhu, Z., Wu, W., Zou, W. and Yan, J., 2018. End-to-end flow correlation tracking with spatial-temporal attention. In Proceedings of the IEEE Conference on Computer Vision and Pattern Recognition (pp. 548–557).

[175] Zhuang, P., Fu, X., Huang, Y. and Ding, X., 2017. Image enhancement using divide-and-conquer strategy. Journal of Visual Communication and Image Representation, 45, pp.137–146.